UNIVERSIDAD CATÓLICA DEL NORTE

FACULTAD DE CIENCIAS

Departamento de física

TSALLIS STATISTICS IN THE EARLY UNIVERSE: PRIMORDIAL PLASMA, WIMP FREEZE-OUT, AND DYNAMICAL NONEXTENSIVITY

Thesis submitted in fulfillment of the requirements for the degree of Master of Science with a specialization in Physics (Magíster en Ciencias con mención en Física).

MATIAS GONZALEZ MERCADO

Thesis Advisor: Dr. Roberto Lineros

Antofagasta, Chile.
June, 2026

To my beloved ones. And La Tumba.

Contents

List of Figures

List of Tables

Acknowledgements

I acknowledge the Nucleo de Investigacion en Simetrias y la Estructura del Universo of Universidad Católica del Norte, NISEU-UCN, for the academic and institutional support provided during the development of this thesis. In particular, I acknowledge the support granted under Resolución VRIDT N°200/2025, which contributed to strengthening this research and its connection with the scientific work developed within the group.

I am especially grateful to my thesis advisor, Dr. Roberto Lineros, for his guidance, availability, and support throughout this process. His comments, suggestions, and physical insight were essential for structuring this research, improving its theoretical formulation, and advancing the interpretation of the results obtained.

Finally, I thank my beloved ones for their constant support throughout this process.

Abstract

This thesis studies a nonextensive generalization of the primordial plasma in the early Universe using Tsallis statistics. The basic idea is that, before Big Bang Nucleosynthesis, the plasma could have contained long range interactions, correlations, memory effects, or residual nonextensive behavior encoded in a parameter $q \neq 1$. Starting from the maximum entropy principle, q-generalized distribution functions are obtained and used to modify the thermodynamic quantities of the plasma, such as the number density, energy density, entropy density, effective relativistic degrees of freedom, and the Hubble rate.

Two freeze-out descriptions are developed. The First Order Model corresponds to expanding the q-generalized distributions around the extensive limit, keeping only corrections linear in $(q-1)$. This model is useful as a controlled approximation, but it is not precise enough when the deformation is not extremely small. The Exact Model, instead, uses the full q-exponential without expanding the distribution functions. For this reason, the main phenomenological analysis is based on the Exact Model, where the WIMP abundance $Y_{\chi,q}(x)$, the relic density $\Omega_{\chi,q}h^2$, and the freeze-out point $x_f = m_\chi/T_f$ are obtained by solving an effective q-generalized Boltzmann equation.

The relic abundance by itself does not give a robust bound on q, because different combinations of q, the annihilation parameters, and the WIMP mass can reproduce the observed dark matter abundance. In practice, the annihilation cross section remains the dominant quantity controlling $\Omega_{\chi,q}h^2$, while the mass dependence is weaker and mainly enters through the logarithmic behavior of the freeze-out point.

To constrain the nonextensive parameter more directly, the neutrino radiation sector is deformed while photons are kept standard. This maps the correction into $N_{\rm eff}$ through the fermionic radiation factor $R_\nu^{\rm FD}(q)$. The comparison with CMB+BAO gives bounds close to the extensive limit. The BBN Gaussian prior is used only as an illustrative input, because a robust BBN constraint would require following the full BBN physics, including light element abundances, weak interaction rates, the neutron to proton ratio, and the nuclear reaction network. For a more robust constraint we suggest to solve the full kinetic neutrino decoupling scenario which involves neutrino oscillations, finite temperature QED corrections and spectral distortions.

Finally, the strong preference for $q \simeq 1$ before BBN motivates a dynamical parameter $q(T)$ that relaxes toward the extensive limit as the Universe cools. Two phenomenological profiles were proposed for this purpose: a log-linear profile in the plasma temperature and a sigmoid profile, the latter being useful for describing localized transitions. This allows possible nonextensive effects at earlier critical stages, such as EWSB or the QCD crossover, while recovering an almost standard radiation era by $T \sim 1$ MeV. By assuming a separation of timescales, the nonextensive parameter is treated within a quasi-static approximation, which provides a controlled way to discuss the thermodynamic consistency of this scenario. A nonextensive primordial plasma, $q \neq 1$, could motivate future studies of BSM-type interactions and provide a phenomenological window to explore exotic effects not included in the standard thermal framework.

Chapter 1

Introduction

This chapter introduces the physical motivation and the theoretical framework developed in this thesis. We begin by presenting the dark matter problem and the main observational evidence supporting its existence. Then, we discuss why the Cold Dark Matter (CDM) scenario is the standard cosmological framework in which WIMP candidates are usually studied. After that, we introduce the WIMP Freeze-out mechanism and explain why its prediction depends on the thermal history of the Universe before Big Bang Nucleosynthesis (BBN).

The standard computation of thermal Relic Abundance assumes Boltzmann-Gibbs statistics and an extensive primordial plasma. This assumption is well motivated and has been extremely successful. However, it also fixes the statistical structure of the plasma in an epoch where there is no direct experimental access. For this reason, the purpose of this thesis is not to replace the standard framework, but to test how robust the WIMP Freeze-out prediction is under a controlled nonextensive deformation of the thermal background through Tsallis statistics.

In this work, the nonextensive parameter q is treated as a phenomenological quantity that encodes deviations from Boltzmann-Gibbs statistics. The extensive limit is recovered when $q \to 1$. We study how this deformation modifies the thermodynamic quantities of the primordial plasma, the WIMP Freeze-out process, the Relic Abundance, and radiation era observables such as N_{eff}. Finally, since low-energy cosmological observables strongly prefer an almost extensive plasma near the MeV scale, we motivate a dynamical interpretation $q(T)$, where the nonextensive parameter relaxes toward $q \simeq 1$ before BBN.

1.1 The Dark Matter Problem

Dark matter is a hypothetical form of matter that does not interact with the electromagnetic spectrum. This means that, although it is invisible because it does not interact with light, it is estimated to constitute approximately 27% of the energy density and mass of the Universe, exceeding the baryonic matter by roughly five to one. Its origin and nature remain among the greatest mysteries of modern science, since no particle in the current Standard Model of particle physics satisfies all the requirements to be a viable dark matter candidate.

Its existence is not postulated arbitrarily, but is instead motivated by a large body of observational evidence:

- **Galactic Rotation Curves:** Stars in the outer regions of galaxies rotate at higher speeds than predicted by visible matter alone. According to Newtonian mechanics, they should move more slowly the farther they are from the galactic center [2]. The observed high velocities imply the existence of an extended halo of invisible matter that provides additional gravitational attraction, keeping stellar velocities approximately constant or even increasing along the galactic radius.

- **Gravitational Lensing:** Light emitted by distant objects is deflected when passing near massive structures such as galaxy clusters. The magnitude of this effect, known as gravitational lensing, allows one to infer the total mass of the cluster. Observations consistently reveal a total mass much larger than the amount of visible matter, strongly suggesting the presence of a substantial dark matter component [3].

- **Cosmic Microwave Background (CMB):** The study of anisotropies, namely the small temperature fluctuations in the CMB, provides one of the strongest pieces of evidence for dark matter. The cosmological models that best reproduce these observations require the presence of cold dark matter in order to explain the formation of large scale structures such as galaxies and galaxy clusters [4].

These observations strongly motivate the study of theoretical frameworks capable of explaining the origin, stability, and abundance of dark matter.

1.2 Cold Dark Matter and the WIMP Paradigm

In the standard cosmological picture, dark matter is usually described as Cold Dark Matter. The word "cold" means that the dark matter component was non-relativistic during the epoch of structure formation. This is relevant because relativistic, or hot, dark matter would erase small-scale structures through free streaming, while CDM allows the growth of structures in agreement with observations. In this thesis, we focus on the CDM scenario because WIMPs are massive thermal relics that naturally become non-relativistic well before the epoch of structure formation.

Precision measurements of the cosmic microwave background, carried out by the Planck satellite together with complementary cosmological observations, have determined the cold dark matter abundance with high accuracy. The current value of the cold dark matter density parameter is

$$\Omega_c h^2 = 0.120 \pm 0.001, \tag{1.1}$$

within the ΛCDM framework [4]. Here, Ω_c is the present cold dark matter density parameter and h is the dimensionless Hubble parameter, defined through $H_0 = 100h$ km s^{-1} Mpc^{-1}. Therefore, any viable theoretical model of dark matter should be able to reproduce this measurement.

A general and well motivated class of cold dark matter candidates is that of weakly interacting massive particles (WIMPs). In particle physics, a dark matter candidate must be electrically neutral, sufficiently stable on cosmological timescales, and weakly coupled enough to evade current experimental bounds. WIMPs satisfy these basic requirements in many Beyond the Standard Model scenarios.

A viable WIMP candidate must be stable. In beyond the Standard Model scenarios, this stability is often ensured by means of a discrete symmetry. A typical implementation is a Z_2 symmetry, under which Standard Model fields are even and the dark matter candidate is odd [5]. Stability arises because physical processes must conserve parity between initial and final states; therefore, a decay such as $\chi \to f\bar{f}$ is forbidden if χ carries odd parity while Standard Model particles are even. This strategy of extending the Standard Model symmetry content with discrete symmetries is commonly used in particle-physics model building. Since WIMPs are electrically neutral, they may also be their own antiparticles, as in the case of Majorana candidates.

1.3 WIMP Freeze-out and the Pre-BBN Thermal History

In the Early Universe, WIMPs may have been in chemical equilibrium with the primordial plasma. As the Universe expanded and cooled, their equilibrium number density became exponentially suppressed by the Boltzmann factor. Eventually, annihilation reactions became inefficient compared with the cosmic expansion rate. At that point, the abundance freezes out and remains approximately constant in a comoving volume [6]. If no entropy production occurs after decoupling, the Relic Abundance is approximately given by

$$\Omega h^2 \propto \frac{1}{\langle \sigma v \rangle}. \tag{1.2}$$

where $\langle \sigma v \rangle$ is the thermally averaged annihilation cross section. To match the observations in Eq. (1.1), the value of the annihilation thermal cross section has to be approximately

$$\langle \sigma v \rangle \approx 3 \times 10^{-26} \mathrm{cm}^3 \mathrm{s}^{-1} = 2.6 \times 10^{-9} \mathrm{GeV}^{-2}. \tag{1.3}$$

This approximate expression yields the correct observed abundance when the decoupling temperature is of order $T_f \sim m_\chi/20$, where m_χ is the WIMP mass [7]. This remarkable coincidence is commonly known as the *WIMP Miracle*.

Although Eq. (1.2) captures the inverse relation between the Relic Abundance and the annihilation strength, the full prediction is not determined only by $\langle \sigma v \rangle$. It also depends on the thermal history of the Universe, the entropy density, the expansion rate, and the effective number of relativistic degrees of freedom. Therefore, a modification of the primordial plasma before decoupling may propagate into the final WIMP abundance.

This point is especially relevant before Big Bang Nucleosynthesis (BBN). BBN occurs at temperatures of order $T \sim 1$ MeV and provides one of the earliest observational probes of the radiation dominated Universe. Any modification of the expansion rate or relativistic energy density near this epoch is strongly constrained. However, at temperatures above the MeV scale there is no direct experimental observation of the thermal plasma. The next cosmological observable comes much later, in the form of the CMB. Therefore, if dark matter is ever directly discovered, it would provide access to one of the earliest and longest-lived relics of the Universe.

This motivates studying whether the standard WIMP Freeze-out scenario is robust under controlled modifications of the statistical properties of the primordial plasma.

1.4 Boltzmann-Gibbs Statistics and Tsallis Nonextensivity

The standard Freeze-out computation assumes Boltzmann-Gibbs statistical mechanics. In this framework, entropy is additive for independent systems and the equilibrium distributions decay exponentially. This is the usual extensive description of a thermal plasma and it represents the baseline scenario used in standard cosmology.

Tsallis statistics extends Boltzmann-Gibbs statistical mechanics to situations involving long range interactions, strong correlations, and memory effects. Its entropy is defined as

$$S_q \;=\; k\,\frac{1-\sum_i p_i^{\,q}}{q-1}\,, \qquad \lim_{q\to 1} S_q = S_{\mathrm{BG}},$$

where q is the nonextensive parameter, also called the Tsallis Parameter.[1] In practice, one

[1] We use the words **Nonextensive Parameter** and **Tsallis Parameter** indistinctly.

may view q as a single phenomenological parameter that quantifies departures from the standard extensive case. For $q > 1$, the corresponding q-generalized distributions develop power law tails, while for $q < 1$ they exhibit compact support. The Boltzmann-Gibbs result is recovered in the limit $q \to 1$.

This framework has been widely used because it often provides a successful description of systems exhibiting heavy tails, nonlocal effects, or nonequilibrium features. Examples include astrophysical plasmas, solar winds, turbulence, and several complex systems such as networks, traffic, finance, and biological processes. Similar tools also appear in kinetic models with memory, helping to explain why power law behavior is so common across otherwise very different physical settings [8].

These examples do not imply that the primordial plasma must be nonextensive. Rather, they motivate the use of q as a phenomenological parameter to test possible departures from Boltzmann-Gibbs statistics in a controlled way. In the cosmological context considered in this thesis, the central question is how a nonextensive primordial plasma would modify the thermal production of WIMP dark matter and the radiation era observables.

1.5 Hypothesis: A Nonextensive Primordial Plasma

This thesis explores the possibility that the primordial plasma may have been nonextensive in the Tsallis sense, characterized by a parameter $q \neq 1$. Such behavior may arise when long range interactions, slowly decaying correlations, memory effects, or nonstandard thermal features become relevant. The hypothesis is not that the standard cosmological framework is wrong, but that its statistical assumptions can be generalized and tested through cosmological observables.

If $q \neq 1$, the stationary distributions are q-deformed[2], and so are the corresponding integrals for number, energy, and entropy densities. We summarize these modifications through a rescaling factor $R_\rho(q)$, which is defined as the ratio between the q-deformed radiation energy density and the standard one. This factor propagates into the effective relativistic degrees of freedom $g_{*,q}(T)$, $g_{*s,q}(T)$, and the expansion rate $H_q(T)$. Likewise, another rescaling factor $R_n(q)$ affects the number density. Both rescalings operate in the ultrarelativistic regime. Their explicit derivation and implementation are presented in the following chapters.

The modification of H does not come from changing the Friedmann equation itself. Instead, it arises because the energy density that sources the expansion is modified. In a spatially flat radiation dominated Universe, $H^2 \propto \rho$. Therefore, if $\rho \to \rho_q = R_\rho(q)\rho_{\rm std}$, then the Hubble rate is modified as $H_q = \sqrt{R_\rho(q)} H_{\rm std}$.

On this background, we revisit WIMP Freeze-out by solving an effective q-generalized Boltzmann equation and computing $\langle \sigma v \rangle_q$ using both the first order expansion in $(q-1)$ and the exact q-distribution functions, within a partial-wave approximation up to p-wave. This provides a connection between the q-deformed radiation bath and the calculation of the Relic Abundance.

The first order model is not introduced as the final phenomenological description, but as a diagnostic approximation. It allows us to identify analytically how corrections proportional to $(q-1)$ enter the thermodynamic quantities and the Freeze-out equation. Its comparison with the exact q-exponential model is useful precisely because it quantifies the regime where the perturbative treatment fails. For the quantitative results, however, the exact model is adopted.

Within the exact model, the thermally averaged annihilation cross section is written through a partial-wave approximation as

$$\langle \sigma v \rangle_q \approx a + b \, \langle v_{\rm rel}^2 \rangle_q,$$

[2]We use the words **Generalized**, **q-Generalized**, **Deformed** and **q-Deformed** indistinctly.

where a and b are the s-wave and p-wave contributions, respectively [9]. In this thesis, these coefficients are treated as nuisance parameters. Therefore, the Relic Abundance alone does not provide a robust one-parameter bound on q, because different combinations of q, m_χ, and the annihilation parameters can reproduce the observed value $\Omega_c h^2 \simeq 0.12$ [4].

For this reason, this thesis also studies the radiation sector. In particular, we deform the neutrino contribution while photons are kept standard. This maps the q-deformation into the effective number of neutrinos observable $N_{\rm eff}$ through the fermionic radiation factor $R_\nu^{\rm FD}(q)$. The comparison with BBN [10] and CMB+BAO [4] provides a more direct probe of q near the MeV scale. The BBN input is used only as an illustrative Gaussian prior, because a robust BBN constraint would require following the full BBN physics, including light element abundances, weak interaction rates, the neutron to proton ratio, and the nuclear reaction network.

Finally, since radiation era observables restrict constant-q models close to the extensive limit, we further hypothesize that the nonextensive parameter q may be interpreted as a dynamical function of the plasma temperature, $q(T)$. In this scenario, possible nonextensive effects may be present at earlier temperatures, while the plasma relaxes toward $q \simeq 1$ before BBN. Assuming a separation of timescales, the plasma may evolve smoothly through quasi-stationary states without breaking the generalized H-theorem [11].

In this thesis, two scenarios for the nonextensive parameter q are considered:

- A constant $q \neq 1$ during the radiation dominated epoch.
- A relaxation law $q(T) \to 1$ as the temperature decreases, reaching $q \simeq 1$ by the onset of BBN at $T \sim 1$ MeV. This framework is developed by directly promoting the nonextensive parameter to a temperature dependent function and by studying its thermodynamic consistency through the H-theorem.

The concrete goals of this thesis are the following:

- **Develop the theoretical framework:** Compute the fundamental thermodynamic observables, such as number density, entropy density and energy density, from Tsallis nonextensive statistics. Two approaches are analyzed and compared: a first order perturbative model $\mathcal{O}(q-1)$ and an exact model based on the q-exponential without any expansion.
- **Model WIMP evolution:** Formulate the q-generalized Boltzmann equation for the comoving abundance $Y_{\chi,q}$, incorporating the q-generalized thermally averaged annihilation cross section $\langle \sigma v \rangle_q$ within a partial-wave expansion.
- **Quantify the impact of nonextensivity:** Solve the Boltzmann equation numerically in order to determine how the parameter q affects the Freeze-out process and the dark matter Relic Abundance $\Omega_{\chi,q} h^2$, and compare the results with Planck measurements within the ΛCDM framework [4]. In this stage, q is taken to be arbitrary but constant.
- **Degrees of freedom and H-Theorem:** Study how the primordial-plasma degrees of freedom are modified in the nonextensive scenario for arbitrary q, and connect this result with the need for a relaxation model through the H-Theorem, the notion of attractors, and the sensitivity of BBN to changes in the relativistic degrees of freedom.
- **Observational bounds on q:** Quantify and constrain the nonextensive parameter q by confronting the model predictions with Early Universe data. In particular, map the radiative deformation $R_\nu^{\rm FD}(q)$ onto the effective number of neutrinos observable $N_{\rm eff}$ and determine the ranges of q compatible with BBN [10] and CMB+BAO [4] at the 1σ level.

- **Multi-component Dark Matter as a motivated extension:** In the constant-q framework, the underproduction found for $q < 1$ under fixed benchmark annihilation parameters motivates interpreting dark matter as a sum of independently freezing-out stable species [12]. This is not proposed as a necessary solution, but as one possible phenomenological extension when a single thermal component does not reproduce the full observed abundance.

- **Motivate and develop a dynamical nonextensive parameter $q(T)$:** Since low-energy observations restrict constant-q models, see Table 6.2, we propose a thermodynamically consistent model where q relaxes with temperature. Assuming a separation of timescales, we argue that the plasma may evolve smoothly through quasi-stationary states without breaking the generalized H-theorem [11]. Using a sigmoid profile for key phase transitions, such as EWSB and QCD, we aim to measure the temporary spike in thermodynamic non-linearity and verify that it vanishes before Big Bang Nucleosynthesis.

1.6 Strategy and Observational Approach

To address the hypothesis introduced above, the strategy of this thesis is divided into three connected levels: the statistical description of the plasma, the cosmological propagation of the q-deformation[3] and the phenomenological comparison with Relic Abundance and radiation era observables.

First, we construct the thermodynamic background using both the first order approximation and the exact q-distribution functions. This allows us to identify the analytical structure of the corrections and, at the same time, determine the regime where the perturbative approximation loses reliability.

Second, we propagate the q-deformation through the rescaling factor $R_\rho(q)$ into the effective degrees of freedom and the expansion rate [1]. In the exact model, this step is particularly relevant because the full q-exponential modifies the thermodynamic integrals nonlinearly. Schematically, this propagation is written as

$$\rho_q = R_\rho(q)\rho_{\rm std}, \qquad g_{*,q}(T) = R_\rho(q)g_*(T), \qquad g_{*s,q}(T) = R_\rho(q)g_{*s}(T),$$

and

$$H_q(T) = \sqrt{R_\rho(q)}H_{\rm std}(T).$$

Finally, we solve the generalized Boltzmann equation for the comoving abundance $Y_{\chi,q}$ and compute the final Relic Abundance $\Omega_{\chi,q}h^2$.

To connect the framework with observations, we map the deformation into an effective change in radiation, expressed through a shift in the effective number of neutrinos $N_{\rm eff}$ [13], and compare the results with BBN [10] and CMB+BAO [4]. Under these assumptions, photons are assumed to rethermalize and behave nearly extensively, while neutrinos, which decouple near the MeV scale, may retain a nonextensive imprint that manifests itself as a contribution to $\Delta N_{\rm eff}$.

Within our framework, the partial-wave coefficients (a, b) [9] are treated as nuisance parameters. For each value of q, they may be retuned within physically reasonable priors so that the Relic Abundance matches observations,

$$\Omega_c h^2 \simeq 0.12.$$

[3]Note: The parameter q is treated as a phenomenological quantity encoding departures from Boltzmann-Gibbs statistics. No specific microscopic derivation of q from a concrete BSM sector is assumed in this thesis.

From this perspective, the Freeze-out scenario acts as a consistency test between the q-deformed cosmological background and a viable Relic Abundance. The strongest direct leverage on q, however, comes from radiation era observables such as BBN and the CMB, because these observables are more directly sensitive to changes in the relativistic energy density near the MeV scale.

1.7 Motivation

The motivation for this work is based on the following points:

- Public programs used for dark matter abundance calculations, such as `micrOMEGAs` [14], usually rely on standard Boltzmann-Gibbs statistics when solving the Boltzmann equation. This is the standard and observationally successful assumption. In this thesis, we take that assumption as the baseline to be tested by asking how the Freeze-out prediction changes when the statistical structure of the plasma is deformed in a controlled way.

- Some particle physics models containing dark matter candidates possess parameter spaces that are already highly constrained, or even partially excluded, by current experiments. Applying nonextensive statistical mechanics in these contexts could modify the cosmological predictions of the models, such as the Relic Abundance or the required annihilation cross sections. The relevant point is not merely to enlarge parameter space, but to identify whether nonextensive effects can mimic, weaken, or strengthen the cosmological constraints imposed on dark matter models, provided that consistency with all relevant experimental constraints is maintained.

- Since radiation era observables strongly prefer an approximately extensive plasma near the MeV scale, any sizeable nonextensive effect at earlier temperatures must relax before BBN. This motivates studying q as a temperature-dependent parameter rather than only as a constant deformation. In the standard picture, the radiation dominated epoch is described by the extensive limit $q = 1$; here, we allow for controlled departures from extensivity, $q \neq 1$, and explore how such departures could disappear before the onset of Big Bang Nucleosynthesis.

These motivations justify studying nonextensivity not as a purely formal extension of statistical mechanics, but as a phenomenological framework capable of modifying the thermal history of the Early Universe in a quantitatively testable way.

Chapter 2

Cosmology Basics and Relic Production

In this chapter we introduce the fundamental concepts behind cosmology and the production of thermal relics through the Freeze-out process, with particular focus on dark matter. We begin by reviewing Einstein's field equations and the cosmological principle, which states that the Universe is homogeneous and isotropic on sufficiently large scales. Then, we introduce the Friedmann-Lemaître-Robertson-Walker (FLRW) metric, which describes an expanding Universe consistent with this principle.

By applying this metric to Einstein's equations, one obtains the Friedmann equations, which describe the dynamics of the cosmic expansion. These equations allow us to connect the expansion of the Universe with its energy content. From this framework, we can also establish the conservation equation and introduce an equation of state for the components of the Early Universe. This provides the basis for the standard ΛCDM model.

With this cosmological background, we then describe the thermodynamics of the Early Universe in the equilibrium regime, where the interaction rates of particles are much larger than the expansion rate of the Universe. In this regime, statistical mechanics allows us to obtain the main macroscopic cosmological quantities, such as the number density, energy density, pressure, entropy density, and the effective relativistic degrees of freedom.

Finally, to study how relic abundances are generated, such as the dark matter abundance, it is necessary to consider processes that depart from thermal equilibrium. In this case, the relevant tool is the Boltzmann equation, which relates the evolution of the particle number density with both the expansion of the Universe and the microscopic interactions of the species under study. In this work, this formalism is applied to the Freeze-out production of dark matter.

2.1 The Expanding Universe: ΛCDM Model

In this section we introduce the standard cosmological framework used to describe the expansion of the Universe. Starting from the cosmological principle and the FLRW metric, we obtain the Friedmann equations, which relate the expansion rate to the energy content of the Universe. This provides the basis for the ΛCDM model.

2.1.1 Einstein Equations and the Cosmological Principle

The starting point of the standard cosmological model is General Relativity, whose dynamics are encoded in Einstein's equations [6]

$$G_{\mu\nu} + \Lambda g_{\mu\nu} = \frac{8\pi}{M_{\rm Pl}^2} T_{\mu\nu}, \tag{2.1}$$

where $G_{\mu\nu}$ is the Einstein tensor, $T_{\mu\nu}$ is the energy-momentum tensor of the cosmic fluid, Λ is the cosmological constant, and $M_{\rm Pl}$ is the Planck mass. In cosmology, one further assumes the *Cosmological Principle*, i.e., that the Universe is homogeneous and isotropic on sufficiently large scales. Since Einstein's equations relate spacetime geometry to the energy-momentum content, this assumption strongly restricts the allowed geometry and leads directly to the FLRW metric.

2.1.2 The Friedmann-Lemaître-Robertson-Walker (FLRW) Metric

The spacetime metric compatible with homogeneity and isotropy is the FLRW metric, whose line element is defined as

$$ds^2 = dt^2 - a^2(t)\left(\frac{dr^2}{1-kr^2} + r^2 d\theta^2 + r^2 \sin^2\theta\, d\phi^2\right), \tag{2.2}$$

where $a(t)$ is the scale factor, which measures how physical distances evolve due to cosmic expansion. The parameter k encodes the spatial curvature: $k = +1$ for a closed geometry, $k = -1$ for an open geometry, and $k = 0$ for flat spatial sections.

2.1.3 Expansion Dynamics: Friedmann Equations

The Friedmann equations provide the basis for describing the dynamics of the standard cosmological model. They are obtained by imposing the Cosmological Principle in Einstein's equations [6], i.e., by applying the FLRW metric (2.2) to these equations.

The temporal component of Einstein's equations gives rise to the first Friedmann equation:

$$H^2 = \frac{8\pi}{3M_{\rm Pl}^2}\rho - \frac{k}{a^2}. \tag{2.3}$$

This equation relates the Universe's expansion rate to its energy content and spatial curvature. Here, $H \equiv \dot{a}/a$ is the Hubble parameter, ρ represents the total energy density, and the term k/a^2 contains the curvature contribution determined by the FLRW geometry.

From the spatial components of Einstein's equations, and in combination with the first equation, one obtains the second Friedmann equation, known as the acceleration equation:

$$\frac{\ddot{a}}{a} = -\frac{4\pi}{3M_{\rm Pl}^2}(\rho + 3P). \tag{2.4}$$

This second equation describes the acceleration of cosmic expansion, $\ddot{a}$. The term P represents the total pressure exerted by the constituents of the Universe. The cosmological constant Λ is not included explicitly in Eq. (2.4), since this thesis focuses on the Early Universe. In the radiation dominated epoch, the contribution associated with Λ is negligible compared with the radiation content.

2.1.4 Energy content, conservation, and equations of state

On the other hand, the covariant conservation of the energy-momentum tensor, $\nabla_\mu T^{\mu\nu} = 0$, allows one to obtain a conservation equation [7]:

$$\dot{\rho} = -3H(\rho + P). \tag{2.5}$$

The Friedmann equations (2.3), (2.4) and the conservation equation (2.5) are not all independent. To close the system and describe the evolution of the cosmic fluid, it is necessary to specify an equation of state. For this we introduce the barotropic equation of state of the form

$P = w\rho$, where the parameter w determines the type of energy content present. In this thesis, the main interest is the radiation dominated Universe, when the plasma was very dense, hot, and the particle velocities were relativistic. In this case, the equation of state takes the form $P = \rho/3$, with $w = 1/3$.

2.1.5 ΛCDM as the Standard framework

The ΛCDM (*Lambda Cold Dark Matter*) model [15] is the current standard theoretical framework of cosmology. It successfully describes the evolution of our Universe and its large scale structures, integrating the Big Bang theory with two fundamental components: cold dark matter and Dark Energy, represented by the cosmological constant Λ. Although the cosmological constant is negligible during the radiation era considered in this thesis, the ΛCDM model provides the observational framework in which quantities such as $\Omega_c h^2$ are inferred.

To compute how each component contributes to the total abundance of the Universe, the dimensionless density parameters Ω_i are defined. In general, each parameter represents the ratio between the density of a specific component ρ_i and the critical density, ρ_c. For present day quantities, this critical density is defined as

$$\rho_c = \frac{3M_{\rm Pl}^2 H_0^2}{8\pi}, \tag{2.6}$$

where H_0 is the present value of the Hubble parameter.

The main contributors to the Universe content are matter, radiation, and Dark Energy:

$$\Omega_M = \frac{\rho_{M,0}}{\rho_c}, \qquad \Omega_{\rm rad} = \frac{\rho_{\rm rad,0}}{\rho_c}, \qquad \Omega_\Lambda = \frac{\rho_{\Lambda,0}}{\rho_c}, \tag{2.7}$$

where the subscript 0 denotes present day values. The geometry of the Universe is described in turn by the curvature parameter,

$$\Omega_k = -\frac{k}{a_0^2 H_0^2}. \tag{2.8}$$

The sum of all these contributions must, by definition, be equal to one:

$$\Omega_M + \Omega_{\rm rad} + \Omega_\Lambda + \Omega_k = 1. \tag{2.9}$$

Observations such as luminosity measurements of distant supernovae, which act as *standard candles* (astrophysical objects whose absolute luminosity is known so that, by estimating their apparent brightness, it is possible to compute their distance) [16], and the analysis of the Cosmic Microwave Background, have determined these parameters with great precision.

Experimental results indicate that the current Universe is spatially flat, or very close to it, implying that the curvature contribution is negligible, $\Omega_k \approx 0$. Moreover, at present, the energy density of radiation, $\Omega_{\rm rad}$, is insignificant compared to matter and Dark Energy. Under these conditions, the cosmic budget is greatly simplified for a present day approximation:

$$\Omega_M + \Omega_\Lambda \approx 1. \tag{2.10}$$

In turn, the total matter density parameter, Ω_M, is decomposed into two main types: baryonic matter, Ω_b, and cold dark matter, Ω_c, sometimes denoted $\Omega_{\rm DM}$. Therefore, the total matter density is the sum of both:

$$\Omega_M = \Omega_b + \Omega_c. \tag{2.11}$$

Currently, matter, baryonic and dark, is estimated to constitute approximately 30% of the Universe's energy density, while Dark Energy accounts for the remaining 70%. These values are measured/fixed by CMB measurements, SNI supernovae, Baryon Acoustic Oscillations (BAO), and abundances of light elements [4, 16, 17, 18].

2.2 Thermodynamics and equilibrium in the Early Universe

To understand the origin of the particles that make up the present Universe, it is necessary to study the physics of the primordial plasma. In its early stages, the Universe was a dense and hot system assumed to be in thermal equilibrium, whose behavior is described by statistical mechanics. This framework allows one to model the evolution of the particle species in the primordial plasma. In this thesis, it is applied specifically to the thermal production and abundance of dark matter.

As the Universe expanded, it cooled; as a consequence, interaction rates between particles decreased. For certain particle species, interactions eventually became insignificant compared to the Hubble expansion rate of the Universe, leading to a phenomenon known as thermal decoupling or Freeze-out. This mechanism gives rise to relics: particles whose abundance "freezes" and remains constant to the present day.

The fundamental mathematical tool to describe this process is the Boltzmann equation, which governs the evolution of the density of a species by describing how the interaction rate competes with the Hubble expansion rate [6]. The following subsections develop this formalism in detail to determine the abundance of a thermal relic, with a specific focus on WIMPs, which together with the contents of the following chapters will contribute to the proposed model.

2.2.1 The Primordial Plasma and Thermal Equilibrium

In the early stages of the Universe, the temperature and density were high enough to keep matter in a primordial plasma state, in which Standard Model particle species interacted continuously and efficiently. The condition for thermal equilibrium is that the particle interaction rate, $\Gamma \sim n\langle\sigma v\rangle$, where n is the number density of particles, is much larger than the expansion rate of the Universe, characterized by the Hubble parameter H. As long as $\Gamma \gg H$ holds, collisions are frequent and the plasma shares a common temperature, with well defined energy distributions.

Under this assumption, the macroscopic properties of the plasma are described through statistical mechanics using the equilibrium distribution function f [6], which sets the mean occupation number of a state with energy E:

$$f(E) \;=\; \frac{1}{\exp\Big[(E-\mu)/T\Big] + \xi}\,, \tag{2.12}$$

where T is the plasma temperature, μ the chemical potential, and ξ determines the statistics: $\xi = +1$ for fermions (Fermi-Dirac), $\xi = -1$ for bosons (Bose-Einstein) and $\xi = 0$ for the classical limit (Maxwell-Boltzmann).

From $f(E)$, macroscopic thermodynamic observables for a species with g internal degrees of freedom are defined:

$$n \;=\; g\int \frac{d^3p}{(2\pi)^3}\, f(E)\,, \tag{2.13}$$

$$\rho \;=\; g\int \frac{d^3p}{(2\pi)^3}\, E(p)\, f(E)\,, \tag{2.14}$$

$$P \;=\; g\int \frac{d^3p}{(2\pi)^3}\, \frac{p^2}{3\,E(p)}\, f(E)\,, \tag{2.15}$$

with $E(p) = \sqrt{p^2+m^2}$. Here, m is the particle mass. The factor g summarizes the sum over internal states, such as spin and polarization, assuming equiprobable population in thermal

equilibrium. A standard caveat is that of neutrinos, for which only left-handed helicity states are significantly populated.

The usual results for n and ρ, which are the most relevant cases for the model, are [19]:

$$n = \begin{cases} \dfrac{\zeta(3)}{\pi^2}\, g\, T^3\,, & \text{bosons, } \xi = -1\,, \\ \dfrac{3}{4}\dfrac{\zeta(3)}{\pi^2}\, g\, T^3\,, & \text{fermions, } \xi = +1\,, \\ g\left(\dfrac{mT}{2\pi}\right)^{3/2} e^{-m/T}\,, & \text{non-relativistic, } \xi = 0\,, \end{cases} \tag{2.16}$$

where ζ is the Riemann zeta function. In the relativistic regime, $T \gg m$, the number density scales as T^3, while in the non-relativistic regime, $T \ll m$, the Boltzmann exponential suppression appears.

Similarly, the energy density is

$$\rho = \begin{cases} \dfrac{\pi^2}{30}\, g\, T^4\,, & \text{bosons, } \xi = -1\,, \\ \dfrac{7}{8}\dfrac{\pi^2}{30}\, g\, T^4\,, & \text{fermions, } \xi = +1\,, \\ m\, n\,, & \text{non-relativistic, } \xi = 0\,, \end{cases} \tag{2.17}$$

so in the relativistic limit $\rho \propto T^4$, and in the non-relativistic limit rest mass energy dominates, $\rho \simeq mn$. In the calculations that follow, the chemical potential is neglected, $\mu \simeq 0$, appropriate for the Early Universe where $\mu \ll T$ and the matter-antimatter asymmetry is small [19]. To describe the total content of a relativistic plasma in equilibrium, it is useful to compact the contribution of all species into

$$\rho = g_* \frac{\pi^2}{30} T^4\,, \tag{2.18}$$

where g_* is the effective number of relativistic degrees of freedom,

$$g_* = \sum_{\text{bosons}} g_i \left(\frac{T_i}{T}\right)^4 + \frac{7}{8} \sum_{\text{fermions}} g_j \left(\frac{T_j}{T}\right)^4 . \tag{2.19}$$

Here g_i and g_j count the internal states of each species, and the ratios T_i/T, T_j/T allow one to include species with temperatures different from that of the plasma.

An equally relevant quantity is the entropy density s, which for $\mu \simeq 0$ satisfies [20]

$$s = \frac{\rho + P}{T}\,. \tag{2.20}$$

For a relativistic gas, $P = \rho/3$, and using (2.18), it follows that

$$s = \frac{4}{3}\frac{\rho}{T} = g_{*s} \frac{2\pi^2}{45} T^3\,, \tag{2.21}$$

where g_{*s} is the effective number of entropic degrees of freedom,

$$g_{*s} = \sum_{\text{bosons}} g_i \left(\frac{T_i}{T}\right)^3 + \frac{7}{8} \sum_{\text{fermions}} g_j \left(\frac{T_j}{T}\right)^3 . \tag{2.22}$$

The difference in exponents in T between g_* and g_{*s} is essential when dealing with decouplings: when a species decouples, its temperature can evolve differently from the plasma's, and g_* and g_{*s} cease to coincide.

Finally, the comoving entropy $S \equiv s\,a^3$ is conserved to a good approximation for an adiabatically expanding Universe. This implies that

$$S \;=\; s\,a^3 \;=\; \text{constant}\,, \tag{2.23}$$

which makes s, and the comoving abundance $Y \equiv n/s$, central tools for tracking the evolution of species in the Early Universe [19].

2.2.2 The Boltzmann equation and species evolution

Once equilibrium observables are defined, the next step is to describe the evolution of the species as they deviate from it. The fundamental tool for this purpose is the Boltzmann equation, which governs the microscopic evolution of the distribution function f in phase space. In its general covariant form, the equation is expressed as [21]:

$$L[f] = C[f], \tag{2.24}$$

where the Liouville operator $L[f]$ describes the variation of f due to free motion of particles and the effect of spacetime expansion. On the other hand, the collision term $C[f]$ represents the variation of f due to interactions of the species of interest, such as annihilations and scatterings.

The Boltzmann equation is greatly simplified by applying the Cosmological Principle. For a detailed derivation, see [9]. The homogeneity and isotropy of the Universe imply that the distribution function does not depend on position or on the direction of momentum, but only on the energy magnitude E and time, i.e. $f = f(E,t)$. Under this condition, the covariant equation reduces to [19]:

$$E\frac{\partial f}{\partial t} - Hp^2\frac{\partial f}{\partial E} = C[f]. \tag{2.25}$$

The term proportional to H explicitly describes how the expansion of the Universe, through the redshift of momentum, competes with the collisional term $C[f]$ that seeks to restore thermal equilibrium.

2.2.3 The Freeze-out mechanism for thermal relics

The thermal decoupling, or Freeze-out, mechanism explains the current abundance of relics generated in the primordial plasma, as in the case of WIMPs.

Decoupling occurs when the interaction rate of a particle Γ becomes inefficient compared to the expansion rate of the Universe described by the Hubble parameter H. As the temperature drops below the mass of the particle, the equilibrium number density becomes Boltzmann suppressed through the factor $e^{-m/T}$. When $\Gamma \lesssim H$, interactions effectively cease and the number density of the particle deviates from equilibrium, becoming "frozen." From then on, its abundance is simply diluted by the expansion of the Universe.

To model this phenomenon, one starts from the Boltzmann equation for a distribution function f, Eq. (2.25). A macroscopic description is needed; to this end, the Boltzmann equation is integrated in phase space as follows:

$$g\int \frac{d^3p}{(2\pi)^3}\left(E\frac{\partial f}{\partial t} - Hp^2\frac{\partial f}{\partial E}\right) = g\int \frac{d^3p}{(2\pi)^3}C[f], \tag{2.26}$$

where the left hand side represents the effect of expansion on the population of particles. Its integration is a standard result in cosmology [19] and breaks down into two terms: the total

time variation of the number density and how the number density of the particle of interest is diluted due to the expansion of the Universe:

$$g \int \frac{d^3p}{(2\pi)^3} \left(E\frac{\partial f}{\partial t} - Hp^2 \frac{\partial f}{\partial E} \right) = \frac{dn}{dt} + 3Hn, \tag{2.27}$$

where t denotes cosmic time. The right hand side, when integrated, represents the net rate of change in the number of particles per unit volume due to interactions. For the WIMP annihilation process into Standard Model particles, and vice versa, $\chi + \bar{\chi} \leftrightarrow \text{SM} + \text{SM}$, this term is defined through the thermally averaged cross section $\langle \sigma v \rangle$ [19].[1]

$$g_\chi \int \frac{d^3p}{(2\pi)^3} C[f_\chi] = -\langle \sigma v \rangle \left(n_\chi^2 - n_{\chi,\text{eq}}^2 \right), \tag{2.28}$$

where n_χ is the physical, out-of-equilibrium number density in the Universe's volume at a given time, $n_{\chi,\text{eq}}$ is the number density the WIMP candidate would have if it were in perfect equilibrium with the primordial plasma, and $\langle \sigma v \rangle$ is the thermally averaged annihilation cross section that accounts for all pair annihilation processes between the candidate χ and Standard Model particles [9]:

$$\begin{aligned} \langle \sigma v \rangle &= \frac{\int d^3p_1 d^3p_2 \, \sigma v f_{\chi,\text{eq}}(p_1,T) f_{\chi,\text{eq}}(p_2,T)}{\int d^3p_1 d^3p_2 \, f_{\chi,\text{eq}}(p_1,T) f_{\chi,\text{eq}}(p_2,T)} \\ &= \frac{1}{8m_\chi^4 T K_2^2\left(\frac{m_\chi}{T}\right)} \int_{4m_\chi^2}^{\infty} ds \, \sigma(s) \sqrt{s} (s - 4m_\chi^2) K_1\left(\frac{\sqrt{s}}{T}\right), \end{aligned} \tag{2.29}$$

where s is the energy of the center of mass, K_1 and K_2 are modified Bessel functions of the second kind, and $\sigma(s)$ is the traditional annihilation cross section obtained via quantum field theory [22].

Finally, by equating the results of the previous steps, one obtains the Boltzmann equation for the number density. This is the fundamental equation that describes the evolution of the abundance of a thermal relic and the Freeze-out mechanism:

$$\frac{dn_\chi}{dt} + 3Hn_\chi = -\langle \sigma v \rangle \left(n_\chi^2 - n_{\chi,\text{eq}}^2 \right). \tag{2.30}$$

Note that, for a vanishing collisional term, the time variation of the number density depends only on the expansion of the Universe governed by the Hubble parameter H. To simplify the Boltzmann equation and isolate the effect of interactions from dilution by expansion, a change of variables is made. A new quantity, the Yield Y, or comoving abundance, for the dark matter is introduced, defined as the ratio between number density and entropy density:

$$Y_\chi \equiv \frac{n_\chi}{s}.$$

Since the entropy in a comoving volume, $S = sa^3$, is a conserved quantity, the Yield represents the particle abundance per unit of entropy. This definition is particularly useful because, for a decoupled particle species, its Yield Y remains constant.

Additionally, the time variable t is replaced by a dimensionless variable x that relates the mass of the particle m_χ to the plasma temperature T. It is convenient to describe the thermal evolution in terms of the dimensionless variable $x = m_\chi/T$, where T denotes the temperature of the cosmological plasma.[2]

$$x \equiv \frac{m_\chi}{T}.$$

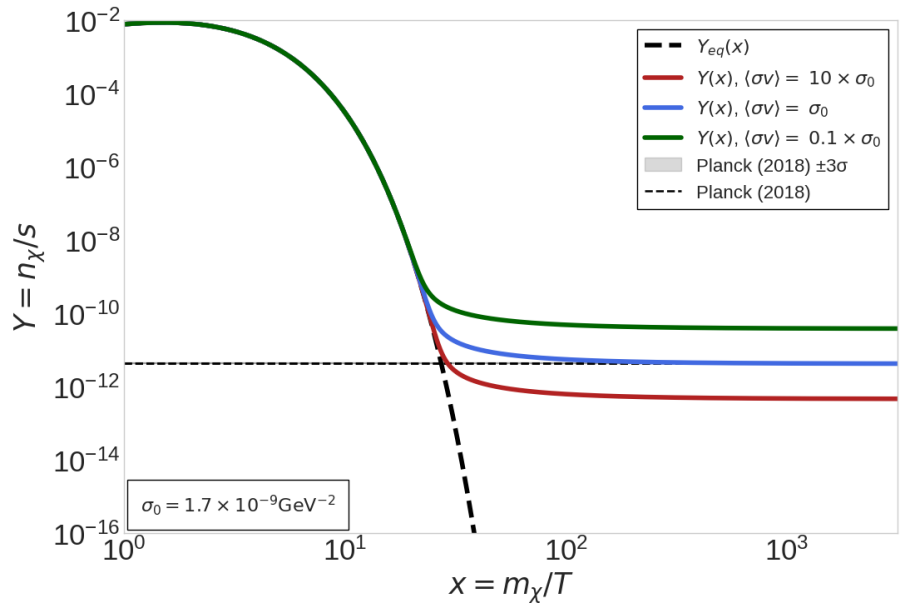

Figure 2.1: **Standard WIMP Freeze-out.** Evolution of the yield $Y(x) = n_\chi/s$ as a function of $x = m_\chi/T$ for different values of $\langle\sigma v\rangle$. The dashed line shows $Y_{\rm eq}(x)$. The horizontal shaded band indicates the $\pm 3\sigma$ band of the asymptotic value Y_∞ compatible with the Relic Abundance measured by Planck (2018).

By applying these two transformations to the Boltzmann equation, it adopts its canonical form for Freeze-out studies. This is the differential equation that must be solved numerically to simulate the evolution of the WIMP abundance and determine its final value:

$$\frac{dY_\chi}{dx} = -\sqrt{\frac{\pi}{45}}\frac{g_{*s}}{g_*^{1/2}} m_\chi M_{\rm Pl} \frac{\langle\sigma v\rangle}{x^2}\left(Y_\chi^2 - Y_{\chi,\rm eq}^2\right). \tag{2.31}$$

Equation (2.31) is, therefore, the fundamental tool for analyzing thermal decoupling. Its numerical solution makes it possible to determine the evolution of the comoving abundance of the particle, $Y(x)$, as the Universe cools. The asymptotic value of this solution is reached when $x \to \infty$ and corresponds to the final comoving abundance denoted by Y_∞ [7]. This theoretical result, Y_∞, is directly connected to one of the best measured cosmological quantities: the dark matter density parameter, $\Omega_\chi h^2$ [4], which corresponds to the cold dark matter contribution of the ΛCDM model, $\Omega_c h^2$. The expression that links the numerical solution of the Boltzmann equation (2.31) with the measured cold dark matter is given by

$$\Omega_\chi h^2 = \frac{\rho_\chi^0 h^2}{\rho_c^0} = \frac{m_\chi s_0 Y_\infty h^2}{\rho_c^0}, \tag{2.32}$$

where $s_0 = 2.9\times10^3$ cm^{-3} is the present day entropy density, and $\rho_c = 1.0537\times10^{-5}\, h^2$ GeV cm^{-3} is the critical energy density for the Universe to have flat space-time geometry [4]. Equation (2.32) is the connection between the theoretical model of the Early Universe and observations of

[1] To refer to WIMP-type dark matter from now on, the notation χ will be used.

[2] In this work, the temperature is used as the macroscopic thermal scale controlling the plasma distribution and the cosmological evolution, not as a direct identification with the energy of each particle. For relativistic species, T sets the typical energy scale up to numerical factors of order unity. For non-relativistic dark matter, instead, T controls the kinetic energy and the velocity dispersion, while the rest mass m_χ sets the dominant contribution to the particle energy. In the q-deformed case, T should be understood as the effective thermal parameter entering the distribution, whereas physical quantities such as number density, energy density, entropy density and thermally averaged rates are obtained from the full q-dependent phase-space integrals.

the present Universe. It allows one to contrast the predictions of a WIMP model, defined by its mass m_χ and cross section $\langle \sigma v \rangle$, with the value measured by experiments such as Planck [4]. In the following chapters, this standard formalism will be generalized using Tsallis' nonextensive statistics. The standard Freeze-out case is shown in Fig. 2.1, obtained by numerically solving the Boltzmann equation (2.31) as the Universe cools.

Chapter 3

Nonextensive Generalization of the Early Universe

The theoretical framework for the generalization of the Early Universe proposed in this study is based on nonextensive statistical mechanics. The core of this formalism is Tsallis entropy, S_q, which is non-additive [8]. In the following sections, it is shown how, via the maximum entropy principle and the constraints of the system, one can derive the q-generalized distribution functions, or mean occupation numbers. These functions are the fundamental tool that will allow the recalculation of cosmological observables, thus incorporating the effects of nonextensivity in the model.

3.1 Foundations of Tsallis Statistics

The theoretical foundation of Tsallis statistics lies in the concept of nonextensivity. In Boltzmann-Gibbs statistical mechanics, entropy is additive for statistically independent systems and the standard equilibrium distributions decay exponentially. Tsallis statistics generalizes this structure through a nonextensive parameter q, recovering the Boltzmann-Gibbs case in the limit $q \to 1$. Typically, this framework is used to describe systems whose behavior deviates from the standard Boltzmann-Gibbs statistics, for example systems with long range interactions, strong correlations, memory effects, or quasi-equilibrium states.

In physical terms, examples where nonextensive statistics has been used phenomenologically include self-gravitating systems, astrophysical plasmas, solar wind distributions and systems with long range correlations. These examples do not imply that the primordial plasma must be nonextensive, but they motivate the use of q as a controlled phenomenological parameter to test deviations from the standard extensive case.

3.1.1 The Tsallis entropy

The pillar of Tsallis statistics is the generalization of Boltzmann-Gibbs entropy S_{BG} through a new functional, Tsallis entropy S_q [8]. This quantity is the starting point for constructing the entire nonextensive framework. Its mathematical definition is given by:

$$S_q \equiv k \frac{1 - \sum_i p_i^q}{q - 1}, \tag{3.1}$$

where $\{p_i\}$ is the set of probabilities for the system's microstates, k is a constant analogous to the Boltzmann constant k_B, and q is a real number known as the nonextensivity parameter. It is essential to note that in the limit $q \to 1$, this expression formally recovers Boltzmann-Gibbs entropy, establishing Tsallis' formalism as a generalization of standard statistical mechanics.

Tsallis entropy, S_q, shares several fundamental properties with Boltzmann-Gibbs entropy S_{BG}, such as non-negativity and the fact that it reaches its maximum value for a uniform probability distribution, i.e. equiprobability. However, the crucial distinction between them lies in the property of additivity.

While S_{BG} is strictly additive, Tsallis entropy is non-additive, or more precisely pseudo-additive. For a system composed of two statistically independent subsystems, A and B, the total entropy of the combined system is not the sum of the individual entropies but obeys the following composition rule:

$$S_q(A+B) = S_q(A) + S_q(B) + \frac{1-q}{k} S_q(A) S_q(B). \tag{3.2}$$

The last term in Eq. (3.2) quantifies the deviation from additivity and is a direct manifestation of the correlations or long range interactions that the nonextensive formalism seeks to describe. In the limit $q \to 1$, standard Boltzmann-Gibbs additivity is recovered, $S_{\mathrm{BG}}(A+B) = S_{\mathrm{BG}}(A) + S_{\mathrm{BG}}(B)$. In the distribution functions used below, the case $q > 1$ is associated with power law tails, while $q < 1$ leads to compact support at high energies [23].

3.1.2 Generalized distribution functions

To derive the generalized distribution function in Tsallis formalism, the maximum entropy principle is applied. This procedure consists of maximizing the entropy functional S_q using the method of Lagrange multipliers subject to a set of constraints representing the macroscopic properties of the system.

The first and most fundamental of these constraints is the normalization of probability, which ensures that the sum of the probabilities of all microstates is unity:

$$\sum_i p_i = 1. \tag{3.3}$$

The constraints for the average internal energy $\bar{E}$ and the average number of particles $\bar{N}$ are defined via q-averages, a specific choice within the nonextensive formalism, the Curado-Tsallis prescription [24]:

$$\bar{E} = \sum_i p_i^q E_i, \qquad \bar{N} = \sum_i p_i^q N_i, \tag{3.4}$$

where E_i and N_i are the energy and the number of particles of the i-th microstate, respectively.[1]

To find the probability distribution $\{p_i\}$ that maximizes Tsallis entropy S_q subject to the system constraints, the method of Lagrange multipliers is used. The constants α, β and γ are Lagrange multipliers associated with the normalization, energy and particle-number constraints, respectively. First, the functional Q is constructed, which incorporates Tsallis entropy and the constraints (3.3) and (3.4):

$$Q = \frac{1}{q-1}\left(1 - \sum_i p_i^q\right) - \alpha \sum_i p_i - \beta \sum_i p_i^q E_i - \gamma \sum_i p_i^q N_i. \tag{3.5}$$

The maximization condition requires that the partial derivative of Q with respect to each probability p_i be zero:

$$\frac{\partial Q}{\partial p_i} = 0. \tag{3.6}$$

[1] This work adopts the Curado-Tsallis prescription for the q-averages. Other choices of constraints, such as normalized escort averages, may modify the analytical prefactors and the numerical values of the inferred bounds. See appendix A.4.1.

Taking the derivative with respect to p_i, one obtains:

$$-\frac{q}{q-1}p_i^{q-1} - \alpha - \beta q p_i^{q-1} E_i - \gamma q p_i^{q-1} N_i = 0. \tag{3.7}$$

Rearranging the terms to isolate p_i^{q-1}:

$$p_i^{q-1}\left(-\frac{q}{q-1} - \beta q E_i - \gamma q N_i\right) = \alpha. \tag{3.8}$$

From this expression, p_i can be isolated. The standard identification of the Lagrange multipliers in statistical physics is $\beta = 1/T$, which corresponds to the inverse temperature, and $\gamma = -\mu/T$, introducing the chemical potential μ. The multiplier α is subsequently determined by the normalization condition $\sum_i p_i = 1$. By solving for p_i and imposing normalization, it is found that the sum in the denominator ensures $\sum_i p_i = 1$. The final result for the probability of the i-th microstate is:

$$p_i = \frac{[1 + \beta(q-1)E_i - \mu\beta(q-1)N_i]^{1/(1-q)}}{\sum_i [1 + \beta(q-1)E_i - \mu\beta(q-1)N_i]^{1/(1-q)}}, \tag{3.9}$$

which gives the probabilities that extremize S_q under the imposed constraints. The denominator is, by definition, the q-generalized partition function, Z_q.

From the probability distribution for the system's microstates, given by Eq. (3.9), it is possible to deduce the mean occupation number for an individual particle state. This quantity, denoted $\langle n_i \rangle_q$, corresponds to the q-generalized distribution function and represents the generalization of quantum and classical statistics to the nonextensive formalism [25]. For notational reasons, it will be denoted by $f_{i,q}$. Its explicit form is:

$$f_{i,q} = \frac{1}{[1 + (q-1)\beta(E_i - \mu_i)]^{1/(q-1)} + \xi}, \tag{3.10}$$

where the parameter ξ distinguishes between different statistics: $\xi = +1$ for fermions, Fermi-Dirac statistics, $\xi = -1$ for bosons, Bose-Einstein statistics, and $\xi = 0$ for the classical case, Maxwell-Boltzmann statistics. In the limit $q \to 1$, Eq. (3.10) reduces to the usual Boltzmann-Gibbs distribution,

$$f_i = \frac{1}{e^{\beta(E_i - \mu_i)} + \xi}. \tag{3.11}$$

The generalized distribution functions given by (3.10) will be useful when generalizing some cosmological observables.

3.1.3 Physical interpretation of nonextensivity

The physical interpretation of the nonextensivity parameter q lies in the deviation from the additivity of fundamental thermodynamic properties such as entropy. This behavior is characteristic of complex systems that do not satisfy Boltzmann-Gibbs statistical theory. Typically, these systems are distinguished by the presence of long range interactions such as gravity, strong correlations among their constituents, quasi-equilibrium states, or a possible fractal structure of spacetime at fundamental scales [23].

As a physical example, in a self gravitating system the interaction is long range and the energy of a subsystem cannot always be treated as independent from the rest of the system. In this type of situation, the usual additive structure of Boltzmann-Gibbs entropy may not be the most adequate phenomenological description. This does not prove that the primordial plasma is nonextensive, but it motivates the use of Tsallis statistics as a controlled way to parametrize departures from the standard equilibrium framework.

This takes on particular relevance in the cosmological context. The earliest epoch of the Universe accessible to direct observational validation is Big Bang Nucleosynthesis (BBN), followed later by the Cosmic Microwave Background (CMB). The physics of earlier eras, such as dark matter decoupling, must be inferred through theoretical models.

3.2 Nonextensive H-Theorem

In the Tsallis framework, the q-generalized logarithm and exponential are introduced,

$$\ln_q f \equiv \frac{f^{\,1-q}-1}{1-q}, \qquad e_q(x) \equiv \Big[1+(1-q)\,x\Big]^{\frac{1}{1-q}}, \tag{3.12}$$

which recover the Boltzmann-Gibbs case in the limit $q \to 1$. The Boltzmann-like functional compatible with (3.12) is

$$H^{(q)} \equiv \int f^{\,q}\, \ln_q f \, d^3p, \tag{3.13}$$

and satisfies the balance equation:

$$\frac{\partial H^{(q)}}{\partial t} + \nabla\cdot \vec{S}_q = -\,\mathcal{G}_q \;\leq\; 0, \qquad \mathcal{G}_q \geq 0, \tag{3.14}$$

where $\vec{S}_q$ is the entropic flux and $\mathcal{G}_q$ measures the entropy production due to collisions. In the homogeneous case, where there is no flux, one has $dH^{(q)}/dt = -\mathcal{G}_q \leq 0$. Relation (3.14) constitutes the statement of the nonextensive H-Theorem [11]. The q-generalized functions constitute the attractor to quasi-equilibrium. In the limit $q \to 1$, the attractor becomes the traditional Boltzmann-Gibbs distribution function. This generalization of the H-Theorem will be useful to connect the formalism with the discussion of the results.

3.3 Cosmological observables in the nonextensive formalism at first order

To carry out the q-generalization of cosmology in the Early Universe, it is essential to use the distribution function obtained in the previous section, Eq. (3.10), via the method of Lagrange multipliers. With this, we begin the path toward the two models used in this thesis: one at first order in $(q-1)$ and another using Eq. (3.10) exactly. In this section we use the first order approximation.

3.3.1 Perturbative approximation of the distribution function

To evaluate the impact of nonextensivity on cosmological observables, it is convenient to work with an analytically manageable form of the q-generalized distribution function (3.10). We proceed to expand the distribution function $f_{i,q}$ in a Taylor series with respect to the parameter $(q-1)$. Truncating the series at first order, one obtains an expression that captures the leading correction due to nonextensivity:

$$f_{i,q} \approx f_{i,q}\Big|_{q=1} + (q-1)\frac{\partial f_{i,q}}{\partial q}\Big|_{q=1}. \tag{3.15}$$

The first term, $f_{i,q}\big|_{q=1}$, corresponds to the standard equilibrium distribution, $f_{i,\mathrm{eq}}$. The second term involves the derivative of the q-generalized function. After performing the calculation and

neglecting the chemical potential, $\mu \ll T$, for the reasons stated in the previous chapter, one arrives at the following expression:

$$f_{i,q} \approx \frac{1}{e^{\beta E_i} + \xi} + \frac{(q-1)}{2} \frac{(\beta E_i)^2 e^{\beta E_i}}{(e^{\beta E_i} + \xi)^2}. \tag{3.16}$$

This approximation is valid only in the regime where $|q-1| \ll 1$. Therefore, it should not be interpreted as a reliable description for arbitrary values of q, but as a perturbative diagnostic around the extensive limit. Equation (3.16) will be the fundamental tool for deriving the modified forms of the number density, energy density, and other observables in the following sections for the first order model.

Cosmological observables are computed from the q-generalized distribution functions, truncated at first order in $(q-1)$.

3.3.2 Generalized Number and Energy Densities

To maintain uniform notation with the standard case, unless otherwise indicated, the chemical potential is neglected, $\mu = 0$. Using (2.13) and (2.14) together with (3.16), one obtains the following expressions. Here, g denotes the number of internal degrees of freedom of the species, m is the particle mass, and ζ is the Riemann zeta function.

Number density

$$n_q(T) = \begin{cases} \dfrac{\zeta(3)}{\pi^2} g\, T^3 + \dfrac{g\,(q-1)}{2\pi^2}\, 12.98\, T^3, & \text{bosons (Bose-Einstein)}, \ \xi = -1, \\ \dfrac{3}{4}\dfrac{\zeta(3)}{\pi^2} g\, T^3 + \dfrac{g\,(q-1)}{2\pi^2}\, 11.36\, T^3, & \text{fermions (Fermi-Dirac)}, \ \xi = +1, \\ g\left(\dfrac{mT}{2\pi}\right)^{3/2} e^{-m/T} \times C, & \text{Maxwell-Boltzmann}, \ \xi = 0, \end{cases} \tag{3.17}$$

where the asymptotic approximation has already been used to reach the Boltzmann suppression factor corresponding to MB statistics. C is defined as follows:

$$C = \left[1 + \frac{q-1}{2}\left(\frac{15}{4} + \frac{3m}{T} + \frac{m^2}{T^2}\right)\right]. \tag{3.18}$$

Energy density

$$\rho_q(T) = \begin{cases} \dfrac{\pi^2}{30} g\, T^4 + \dfrac{30}{\pi^2}\,(1.04)\, g\,(q-1)\, T^4, & \text{bosons (Bose-Einstein)}, \ \xi = -1, \\ \dfrac{7}{8}\dfrac{\pi^2}{30} g\, T^4 + \dfrac{30}{\pi^2}\,(0.97)\, g\,(q-1)\, T^4, & \text{fermions (Fermi-Dirac)}, \ \xi = +1, \\ m\, n_q(T), & \text{Maxwell-Boltzmann}, \ \xi = 0, \end{cases} \tag{3.19}$$

where in the last line the result for n_q in (3.17) is used. For the total relativistic content at common temperature one can introduce the compact notation of q-generalized effective degrees of freedom,

$$g_{*,q}(T) = \sum_{\text{bosons}} g_i \left(\frac{T_i}{T}\right)^4 + \frac{7}{8} \sum_{\text{fermions}} g_j \left(\frac{T_j}{T}\right)^4 + (q-1)\left[9.58 \sum_{\text{bosons}} g_i \left(\frac{T_i}{T}\right)^4 + 8.98 \sum_{\text{fermions}} g_j \left(\frac{T_j}{T}\right)^4\right], \tag{3.20}$$

with which the total relativistic energy density is written as [26]

$$\rho_q(T) = \frac{\pi^2}{30} g_{*,q}\, T^4. \tag{3.21}$$

3.3.3 Entropy Density and Hubble Parameter

From the first law of thermodynamics and the standard definition, the entropy density is written as

$$s_q(T) \;=\; \frac{\rho_q + P_q}{T}\,, \tag{3.22}$$

and in the relativistic regime, $P_q \simeq \rho_q/3$, it adopts the form

$$s_q(T) \;=\; \frac{\rho_q + \rho_q/3}{T} \;=\; \frac{2\pi^2}{45}\, g_{*s,q}\, T^3\,, \tag{3.23}$$

where $g_{*s,q}$ denotes the effective degrees of freedom associated with entropy at first order in $(q-1)$. For species with temperatures T_i (bosons) and T_j (fermions), the result is [26]

$$g_{*s,q}(T) \;=\; \sum_{\text{bosons}} g_i \frac{T_i^3}{T^3} + \frac{7}{8} \sum_{\text{fermions}} g_j \frac{T_j^3}{T^3} + 7.18\,(q-1)\left[\sum_{\text{bosons}} g_i \frac{T_i^3}{T^3} + \frac{15}{16} \sum_{\text{fermions}} g_j \frac{T_j^3}{T^3}\right]. \tag{3.24}$$

In an adiabatically expanding Universe, the comoving entropy $S_q \equiv s_q a^3$ remains approximately constant, which justifies the use of dimensionless abundances $Y_q \equiv n_q/s_q$.

Using the first Friedmann equation for a flat Universe (2.3) and the q-generalized relativistic energy density (3.21), the expansion rate is obtained as

$$H_q(T) \;=\; \sqrt{\frac{8\pi^3}{90}}\, \frac{T^2}{M_{\rm Pl}}\, g_{*,q}^{1/2}\,, \tag{3.25}$$

which generalizes the standard Hubble parameter. This modification does not come from changing the Friedmann equation or the background cosmology itself. Instead, it arises because the radiation energy density that sources the expansion is modified by the q-generalized distribution functions. Thus, in a flat radiation dominated Universe, the relation $H^2 \propto \rho$ implies that the replacement $\rho \to \rho_q$ induces the corresponding replacement $H \to H_q$. In this expression, nonextensivity is encapsulated in $g_{*,q}$, while $g_{*s,q}$ controls the evolution of s_q and Y_q. These first order corrections in $(q-1)$ clarify how nonextensivity systematically modifies the cosmological ingredients involved in the Freeze-out calculation; see Appendix A.5 for more details.

3.4 Cosmological observables using the exact generalized distribution functions

In this section we carry out the generalization of the cosmological observables by using the exact definition of generalized distribution functions within Tsallis statistics. We use the exact q-exponential

$$e_q(-z) = \begin{cases} [1-(1-q)\,z]^{\frac{1}{1-q}}\,, & 1-(1-q)\,z > 0, \\ 0, & \text{otherwise}, \end{cases} \qquad z \equiv \frac{E}{T}, \tag{3.26}$$

from which it follows that for $q < 1$ the support is compact, while for $q > 1$ power law tails appear. Convergence of integrals in 3D requires $q < 4/3$ for number density and $q < 5/4$ for energy density [23].

For q-generalized quantum statistics, FD and BE denote Fermi-Dirac and Bose-Einstein statistics, respectively, while MB denotes Maxwell-Boltzmann statistics. We start from (3.10) with $\mu \simeq 0$ and use dimensionless variables

$$x \equiv \frac{m}{T}, \qquad y \equiv \frac{p}{T}, \qquad \frac{E}{T} = \sqrt{y^2 + x^2}, \tag{3.27}$$

so that $p = y\,T$ and the measures acquire explicit factors of T. The limits in y are

$$y_{\max}(x,q) = \begin{cases} \sqrt{\left(\frac{1}{1-q}\right)^2 - x^2}, & q < 1, \\ \infty, & q \geq 1. \end{cases} \tag{3.28}$$

Thus, if $q > 1$, power law tails appear in the distribution, while if $q < 1$, it presents compact support, i.e., the variable cannot take values beyond a certain finite limit.

With these conventions, the exact thermodynamic observables are

$$n_q(T) = \frac{g}{2\pi^2}\,T^3 \int_0^{y_{\max}} y^2\, f_q\Big(\sqrt{y^2+x^2}\Big)\,dy, \tag{3.29}$$

$$\rho_q(T) = \frac{g}{2\pi^2}\,T^4 \int_0^{y_{\max}} y^2\,\sqrt{y^2+x^2}\, f_q\Big(\sqrt{y^2+x^2}\Big)\,dy, \tag{3.30}$$

$$P_q(T) = \frac{g}{6\pi^2}\,T^4 \int_0^{y_{\max}} \frac{y^4}{\sqrt{y^2+x^2}}\, f_q\Big(\sqrt{y^2+x^2}\Big)\,dy. \tag{3.31}$$

In the relativistic regime relevant for a radiation dominated Universe, the equation of state is preserved as $P_q \simeq \rho_q/3$. Hence the entropy density is written as

$$s_q(T) = \frac{\rho_q(T) + P_q(T)}{T} = \frac{2\pi^2}{45}\, g_{*s,q}(T)\, T^3, \tag{3.32}$$

while the total energy density can be written as

$$\rho_q(T) = \frac{\pi^2}{30}\, g_{*,q}(T)\, T^4. \tag{3.33}$$

In the limit $q \to 1$, expressions (3.29)-(3.33) reduce to the standard Boltzmann-Gibbs formulas [19, 20]. While the exact formulation provides the complete physical picture, it is often useful to analyze the system through a perturbative approach to isolate the leading-order effects of nonextensivity.

3.5 Generalized Distribution Functions: First Order Approximation vs. Exact Formula

Before comparing the numerical behavior of the exact and perturbative distributions, we recall that in the extensive limit $q \to 1$ the q-generalized distribution reduces to the Boltzmann-Gibbs expression

$$f(z) = \frac{1}{e^z + \xi}, \qquad z \equiv \beta E, \tag{3.34}$$

with $\xi = -1$ for BE, $\xi = +1$ for FD, and $\xi = 0$ for MB statistics.

It is necessary to compare (3.16) and (3.10) to ascertain the limitations of a first order model with respect to the relative percentage error compared to the exact q-generalized distribution function. This can be seen in Figs. 3.1 and 3.2, respectively.

The relative error between the exact distribution function and the first order approximation in $(q-1)$ can become large over part of the range $z \equiv \beta E$, especially away from the strict perturbative regime. This shows that the first order approximation is not appropriate for the main numerical constraints when q deviates appreciably from unity. Consequently, the first order model is kept as a diagnostic approximation, while the exact q-generalized distribution will be used for the quantitative phenomenological analysis.

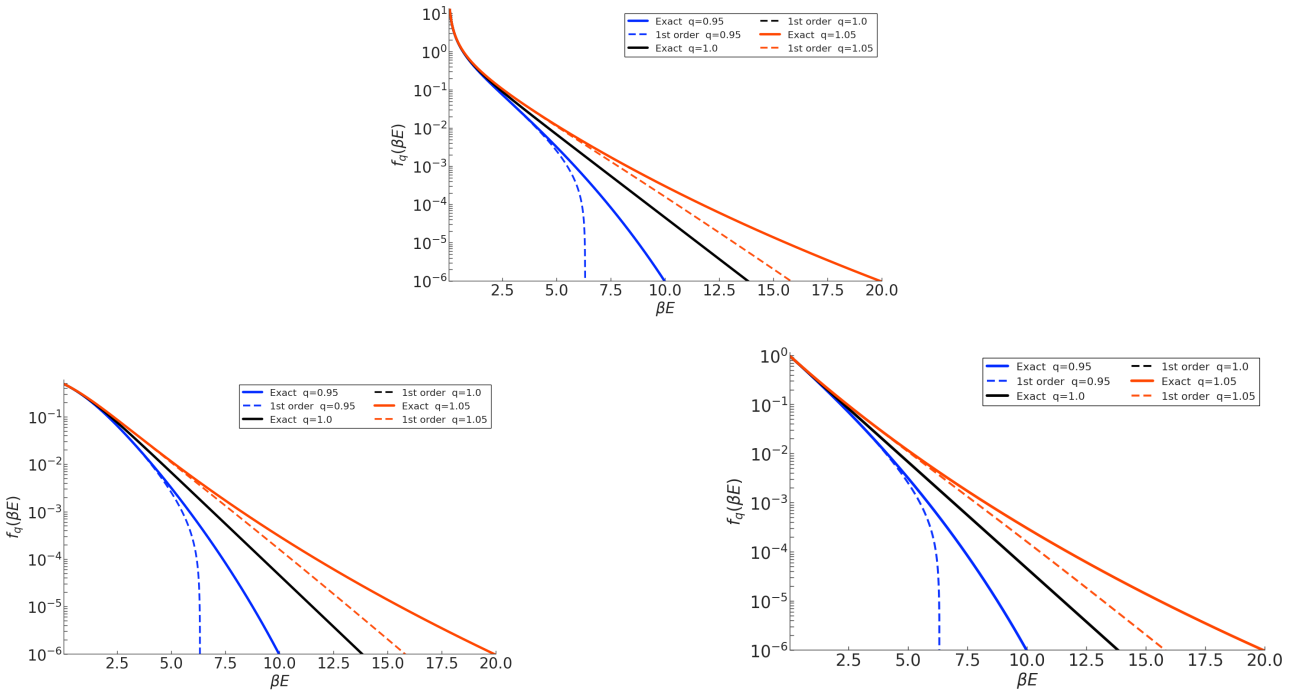

Figure 3.1: q-generalized distributions with vanishing chemical potential, $\mu = 0$, for the three statistics of interest: Bose-Einstein (BE), Fermi-Dirac (FD), and Maxwell-Boltzmann (MB), as functions of $z \equiv \beta E$. For each case, exact curves (solid lines) and the first order approximation in $(q-1)$ (dotted lines) with $q = \{0.95,\ 1.0,\ 1.05\}$ are shown. In the extensive limit $q \to 1$ one recovers $f(z) = 1/(e^z + \xi)$, with $\xi = -1$ (BE), $\xi = +1$ (FD), and $\xi = 0$ (MB).

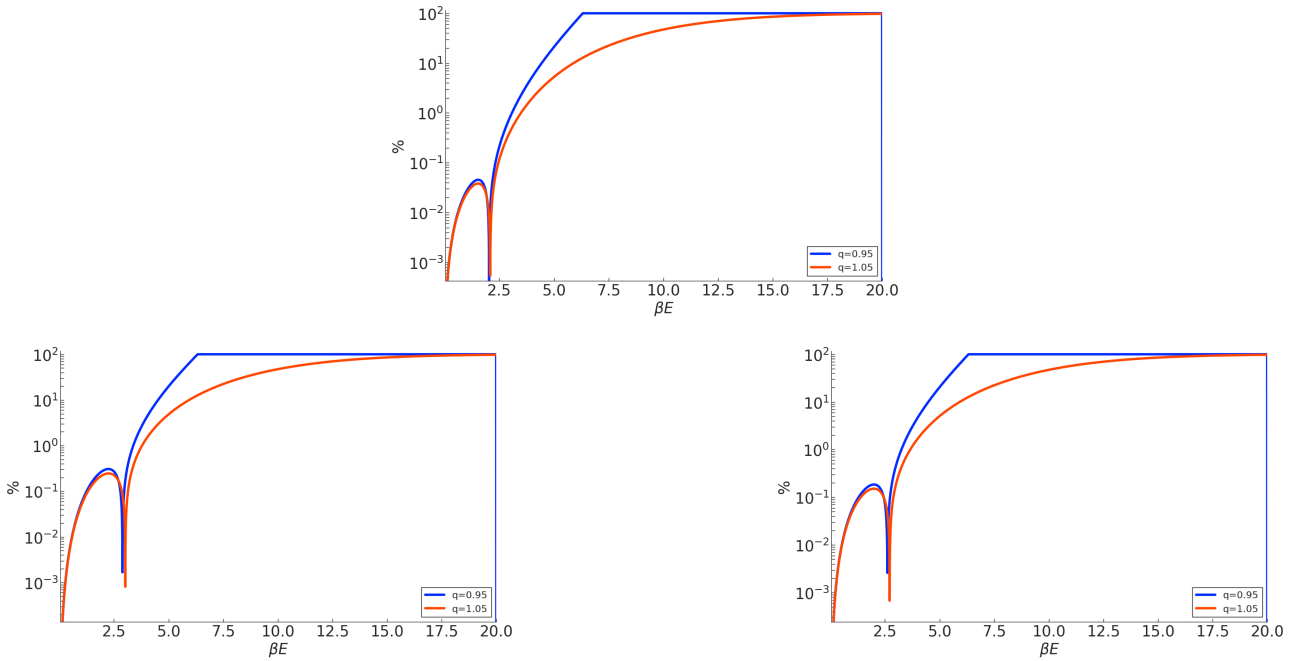

Figure 3.2: Percent relative error of the first order approximation in $(q-1)$ with respect to the exact q-generalized distribution, with $\mu = 0$, for $q = 0.95$ and $q = 1.05$, in the BE, FD, and MB statistics, as a function of $z \equiv \beta E$. The vertical axis is in logarithmic scale to simultaneously highlight the small-error regime and the regions where the approximation loses validity.

Chapter 4

Freeze-out Models for WIMPs in a nonextensive Universe

In this chapter a theoretical model is developed to study the decoupling, or Freeze-out, of WIMP-type dark matter under the hypothesis of a nonextensive primordial Universe. The goal is to build a formalism, based on Tsallis statistics, that generalizes the standard calculation both at first order in $(q-1)$ and through the exact q-generalized distribution functions of Eq. (3.10). The first order model is introduced as a diagnostic approximation, useful to identify analytically how the leading corrections enter the Freeze-out calculation. The exact model, instead, is used as the main quantitative framework for the numerical observables and the thermal decoupling of dark matter. The q-generalized Boltzmann equation and the q-generalized thermally averaged cross section are presented[1], establishing the framework for numerical simulation and comparative analysis with the Relic Abundance measured by Planck (2018) [4], namely $\Omega_c h^2 = 0.120 \pm 0.001$. With this foundation, the numerical algorithms are built for the thermal decoupling process in order to continue exploring the parameter space (a, b, m_χ, q).

4.1 First Order Model

The starting point for the generalization is the Boltzmann equation in its standard form, promoted to a nonextensive context. As a consequence, thermodynamic quantities such as number density are transformed into their q-generalized analogues, $n_\chi \to n_{\chi,q}$. The evolution equation for the dark matter candidate χ is therefore:

$$\dot{n}_{\chi,q} + 3H_q n_{\chi,q} = -\langle \sigma v \rangle_q (n^2_{\chi,q} - n^2_{\chi,q,\mathrm{eq}}). \tag{4.1}$$

To isolate the effect of interactions from cosmic dilution, the change of variables to the Yield, $Y_{\chi,q} = n_{\chi,q}/s_q$, and to the inverse temperature variable, $x = m_\chi/T$, is performed. Here, comoving entropy conservation is assumed as an effective way to formulate the generalized Yield $Y_{\chi,q}$ for WIMP dark matter. The procedure, analogous to the standard case, leads to:

$$\frac{dY_{\chi,q}}{dx} = -\langle \sigma v \rangle_q \frac{s_q}{H_q x} \left(Y^2_{\chi,q} - Y^2_{\chi,q,\mathrm{eq}} \right). \tag{4.2}$$

Substituting the expressions for the entropy density, $s_q = (2\pi^2/45) g_{*s,q} T^3$, and for the Hubble parameter, $H_q = (\sqrt{8\pi^3/90}) g^{1/2}_{*,q} T^2/M_{\mathrm{Pl}}$, the Boltzmann equation acquires its most explicit

[1] The term q-generalized Boltzmann equation is used in an effective sense. A full nonextensive collision operator is not derived here; instead, the macroscopic quantities entering the standard freeze-out equation are promoted to their q-generalized counterparts, $A \to A_q$.

form:

$$\frac{dY_{\chi,q}}{dx} = -\sqrt{\frac{\pi}{45}}\frac{g_{*s,q}}{\sqrt{g_{*,q}}} m_\chi M_{\rm Pl} \frac{\langle\sigma v\rangle_q}{x^2}\left(Y^2_{\chi,q} - Y^2_{\chi,q,\rm eq}\right). \tag{4.3}$$

Given that the energy degrees of freedom $g_{*,q}$ and the entropic ones $g_{*s,q}$ are numerically very similar in the epochs of interest, the approximation $g_{*s,q} \approx g_{*,q}$ can be used [27] to simplify the expression. The final equation to be solved numerically is thus obtained:

$$\frac{dY_{\chi,q}}{dx} = -\sqrt{\frac{\pi}{45}} g^{1/2}_{*s,q} m_\chi M_{\rm Pl} \frac{\langle\sigma v\rangle_q}{x^2}\left(Y^2_{\chi,q} - Y^2_{\chi,q,\rm eq}\right). \tag{4.4}$$

To solve the Boltzmann equation, it is necessary to model the thermally averaged cross section, $\langle\sigma v\rangle_q$. In this work, the partial-wave expansion is used to approximate Eq. (2.29) up to the p-wave term[2] [22]:

$$\langle\sigma v\rangle_q \approx a + b\langle v^2_{\rm rel}\rangle_q, \tag{4.5}$$

where the parameters a and b quantify the intrinsic strength of s-wave and p-wave annihilations, respectively. Nonextensivity manifests itself in the q-average of the relative squared velocity, $\langle v^2_{\rm rel}\rangle_q = 2\langle v^2\rangle_q$. This relation follows from

$$\langle v^2_{\rm rel}\rangle = \left\langle |\mathbf{v}_1 - \mathbf{v}_2|^2 \right\rangle = \langle v_1^2\rangle + \langle v_2^2\rangle - 2\langle \mathbf{v}_1 \cdot \mathbf{v}_2\rangle. \tag{4.6}$$

Assuming no initial directional correlation between the two incoming particles, $\langle \mathbf{v}_1 \cdot \mathbf{v}_2\rangle = 0$, and assuming that both particles belong to the same species and the same thermal distribution, one obtains

$$\langle v^2_{\rm rel}\rangle = 2\langle v^2\rangle. \tag{4.7}$$

This relation is then promoted to the q-generalized prescription. The velocity average is computed by integrating over the first order distribution:

$$\langle v^2\rangle_q \approx \frac{\int_0^\infty v^2 e^{-E/T}\left(1 + \frac{q-1}{2}\frac{E^2}{T^2}\right) d^3v}{\int_0^\infty e^{-E/T}\left(1 + \frac{q-1}{2}\frac{E^2}{T^2}\right) d^3v}. \tag{4.8}$$

Solving this integral leads to the analytical result at first order in $(q-1)$:

$$\langle v^2\rangle_q \approx \frac{3T}{m_\chi}\left(1 + \frac{5}{2}(q-1)\right). \tag{4.9}$$

Finally, the q-generalized thermally averaged cross section to be used in the approximate model is:

$$\langle\sigma v\rangle_q \approx a + b\frac{6T}{m_\chi}\left(1 + \frac{5}{2}(q-1)\right). \tag{4.10}$$

The effective and entropic degrees of freedom $g_{*,q}$ and $g_{*s,q}$ for the calculation take values according to the transition epochs [1] as interpolated tables.

The asymptotic solution of this equation, $Y_{\infty,q}$, is the comoving abundance of *frozen* dark matter. Assuming that in the q-generalized formalism the asymptotic Yield $Y_{\infty,q}$ can be calculated numerically in the same way as in the standard case, it is connected to the current dark matter abundance through the q-generalized analogue of Eq. (2.32):

$$\Omega_{\chi,q}h^2 = \frac{\rho^0_{\chi,q}h^2}{\rho^0_c} = \frac{m_\chi s_0 Y_{\infty,q}h^2}{\rho^0_c}. \tag{4.11}$$

This formalism is applied in the *Python* simulations for arbitrary values of q that remain constant throughout the cooling of the Universe. This allows us to compare the first order model with the exact model introduced next, where Eq. (3.10) is used exactly with $\mu = 0$.

[2]This partial-wave form is a model-independent approximation to the thermal average. A complete particle-physics implementation would require specifying the microscopic annihilation channel and computing the exact thermally averaged cross section from the corresponding exact integral (2.29).

4.2 Exact Model

In this section, a more complete model is developed for WIMP decoupling, based on the use of the exact q-generalized distribution function (3.10), instead of its perturbative approximation. This approach allows one to obtain exact expressions for the q-generalized cosmological observables (3.29)-(3.33). The structure of the resulting Boltzmann equation is analogous to that of the previous model, preserving the same functional form of Eq. (4.4):

$$\frac{dY_{\chi,q}}{dx} = -\sqrt{\frac{\pi}{45}} g_{*s,q}^{1/2} m_\chi M_{\rm Pl} \frac{\langle \sigma v \rangle_q}{x^2} \left(Y_{\chi,q}^2 - Y_{\chi,q,\rm eq}^2 \right), \tag{4.12}$$

where now $g_{*s,q}$, $Y_{\chi,q,\rm eq}$, and $\langle \sigma v \rangle_q$ must be evaluated using their exact non-perturbative integrations. For the thermally averaged cross section, $\langle \sigma v \rangle_q$, the partial-wave expansion of Eq. (4.5) is maintained. However, the observable $\langle v^2 \rangle_q$ is computed numerically using the exact distribution in the form

$$\langle v^2 \rangle_q = \frac{\displaystyle\int_0^{y_{\max}} y^2 \left(\frac{y}{\sqrt{y^2+x^2}} \right)^2 e_q\!\left(-\sqrt{y^2+x^2} \right) dy}{\displaystyle\int_0^{y_{\max}} y^2 \, e_q\!\left(-\sqrt{y^2+x^2} \right) dy}, \tag{4.13}$$

where $y_{\max}$ is the maximum dimensionless momentum $y = p/T$ allowed by the support of the q-exponential e_q.

We now describe the deformations of the cosmological background. We introduce the mapping

$$\rho_q(T) = R_\rho(q)\, \rho(T), \qquad s_q(T) = R_\rho(q)\, s(T), \tag{4.14}$$

so that $g_{*,q}$ and $g_{*s,q}$ reabsorb the variation of ρ and s induced by the q-generalized distribution, in complete consistency with the first order analytical factorization; see Appendix A.6.1.

For an ultra-relativistic gas, with $z \equiv \beta E = E/T$ and the exact q-exponential $e_q(-z)$, the moment ratio reads

$$R_\rho(q) \;\equiv\; \frac{\displaystyle\int_0^{z_{\max}} z^3 \, e_q(-z)\, dz}{\displaystyle\int_0^{\infty} z^3 \, e^{-z}\, dz} \;=\; \frac{1}{6} \int_0^{z_{\max}} z^3 \, e_q(-z)\, dz,$$

$$\text{where} \quad z_{\max} = \begin{cases} \dfrac{1}{1-q}, & q < 1, \\ \infty, & q \geq 1, \end{cases} \tag{4.15}$$

which converges for $q < 5/4$ when $q \geq 1$, since $e_q(-z) \sim z^{-1/(q-1)}$ and the integrand scales as z^3.[3] A fully analogous deformation follows from the number density,

$$n_q(T) = R_n(q)\, n(T), \tag{4.16}$$

with the exact ultra-relativistic expression

$$R_n(q) \;\equiv\; \frac{\displaystyle\int_0^{z_{\max}} z^2 \, e_q(-z)\, dz}{\displaystyle\int_0^{\infty} z^2 \, e^{-z}\, dz} \;=\; \frac{1}{2} \int_0^{z_{\max}} z^2 \, e_q(-z)\, dz, \tag{4.17}$$

using the same $z_{\max}$ as above. For $q \geq 1$ this integral converges for $q < 4/3$, since the integrand scales as z^2.[4]

[3] The factor $R_\rho(q)$ is derived in the ultrarelativistic regime and is used to deform the radiation background. It is not applied as a multiplicative correction to the nonrelativistic WIMP equilibrium abundance.

[4] For $q > 1$, convergence is restricted by the power law tails of the exact q-exponential. For $q < 1$, the compact support restricts the available phase space. Numerical results close to these boundaries must therefore be interpreted with additional caution.

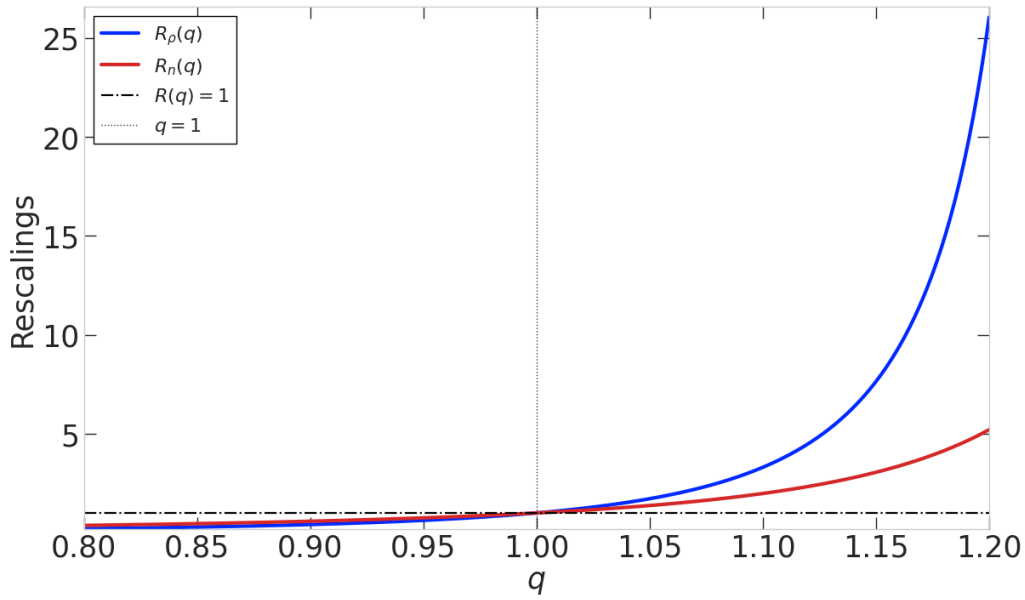

Figure 4.1: **Nonextensive rescalings of the thermal background and number density**. The solid blue curve shows the radiation deformation $R_\rho(q)$ defined in Eq. (4.15), the solid red curve shows the number-density deformation $R_n(q)$ defined in Eq. (4.17). Both R_ρ and R_n are computed with the exact q-exponential, $R_\rho = (1/6)\int_0^{z_{\max}} z^3 e_q(-z)\,dz$ and $R_n = (1/2)\int_0^{z_{\max}} z^2 e_q(-z)\,dz$, with $z_{\max} = 1/(1-q)$ for $q < 1$ and $z_{\max} \to \infty$ for $q \geq 1$; convergence holds for $q < 5/4$ (energy) and $q < 4/3$ (number). At $q = 1$ all rescalings equal unity (dash-dotted line), and the dotted vertical line marks the extensive limit.

These mappings are species-blind. To construct mappings that distinguish the statistics of each species, namely fermions with $\xi = +1$ or bosons with $\xi = -1$, we define:

$$R_n^{(\xi)}(q) \equiv \frac{\displaystyle\int_0^{z_{\max}} \frac{z^2\,dz}{e_q(z)+\xi}}{\displaystyle\int_0^{\infty} \frac{z^2\,dz}{e^z+\xi}}, \qquad R_\rho^{(\xi)}(q) \equiv \frac{\displaystyle\int_0^{z_{\max}} \frac{z^3\,dz}{e_q(z)+\xi}}{\displaystyle\int_0^{\infty} \frac{z^3\,dz}{e^z+\xi}}. \tag{4.18}$$

For simplification purposes, the entire background is rescaled with no species distinction. However, in the bounds for q, an important distinction will be made. Both integrals converge for $q < 4/3$ and $q < 5/4$, respectively. See Appendix A.6.1 for related mappings.

Figure 4.1 shows how $R_n(q)$ and $R_\rho(q)$ behave as functions of q, while Fig. 4.2 shows how the rescalings using quantum distributions behave as functions of q. Both rescalings are constructed in the ultra-relativistic regime, where $E/T \equiv z \equiv p/T$.[5]

In the relativistic regime, Eqs. (2.20) and (2.21) imply $s_q/s = R_\rho(q)$ and therefore

$$g_{*,q}(T) \;=\; R_\rho(q)\, g_*(T), \qquad g_{*s,q}(T) \;=\; R_\rho(q)\, g_{*s}(T), \tag{4.19}$$

which corresponds to a vertical rescaling of the curves $g_*(T)$ and $g_{*s}(T)$. Their shapes, including threshold positions from Standard Model masses and thermal transitions such as QCD, are

[5]Note on rescalings: A single convention for the q-exponentials with heavy tails for $q > 1$, $e_q(z) = [1 + (q-1)z]^{1/(q-1)}$ is used consistently; switching convention can invert the trends and must be avoided. The construction is ultrarelativistic (UR) and near-equilibrium (massless kinematics, well-defined temperature, negligible chemical potentials), so q enters through dimensionless prefactors $R_n(q)$ and $R_\rho(q)$ multiplying the standard integrals for analytic simplicity. When a universal background scaling suffices and quantum ± 1 corrections are subleading, use indistinguishable/MB rescalings ($\xi = 0$). When the observable depends on statistical character or relative weighting between species, use species-aware rescalings that distinguish BE and FD.

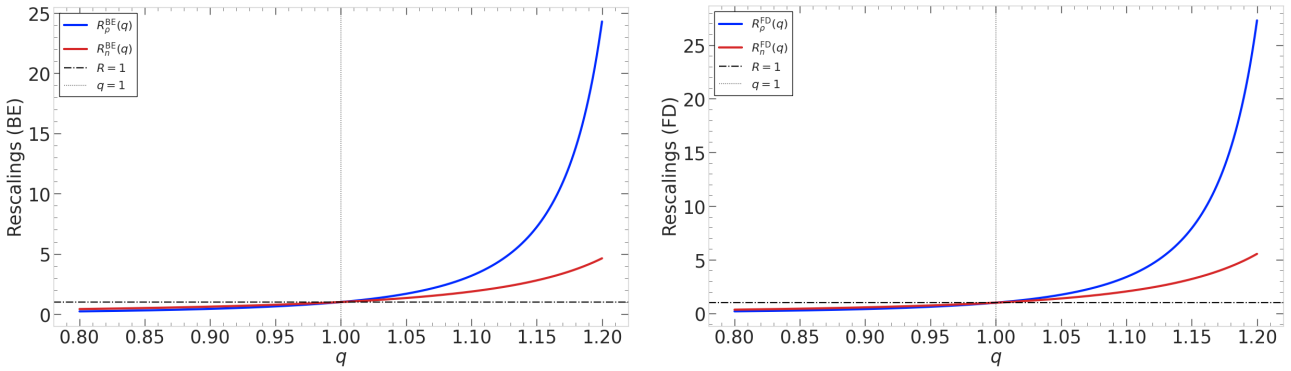

(a) Bosons (BE): $R_\rho^{\rm BE}(q)$, $R_n^{\rm BE}(q)$. (b) Fermions (FD): $R_\rho^{\rm FD}(q)$, $R_n^{\rm FD}(q)$.

Figure 4.2: **Species-aware rescalings as a function of q.** Blue: R_ρ; red: R_n. The dash-dot horizontal line marks $R = 1$ and the dotted vertical line marks $q = 1$, considering $\mu \simeq 0$. The number density species-aware integrals converge for $q < 4/3$ and the energy density species-aware integrals converge for $q < 5/4$.

unchanged, since the particle spectrum is unmodified and only the normalization of energy and entropy at fixed temperature is deformed. The rescaling factors are derived in the ultra-relativistic regime and are used in this work only to describe how the radiation bath is deformed. When WIMPs are non-relativistic, each deformed macroscopic quantity must be calculated by using the corresponding exact integral.

The Hubble rate in a flat Universe reads

$$H \;=\; \sqrt{\frac{8\pi}{3}}\,\frac{\sqrt{\rho}}{M_{\rm Pl}}, \tag{4.20}$$

hence in the nonextensive background

$$H_q(T) \;=\; \sqrt{\frac{8\pi}{3}}\,\frac{\sqrt{\rho_q(T)}}{M_{\rm Pl}} \;=\; \sqrt{R_\rho(q)}\,H(T). \tag{4.21}$$

This is not a modification of the Friedmann equation itself. It is the standard Friedmann relation evaluated with the q-deformed radiation energy density, $\rho_q(T) = R_\rho(q)\rho(T)$. Thus, the gravitational dynamics are not modified; only the thermodynamic source term is rescaled.

The yield is kept as $Y_q \equiv n_q/s_q$ without additional rescalings. The only background modification relevant here is $H_q = \sqrt{R_\rho(q)}\,H$. The equilibrium density $n_{\chi,{\rm eq},q}$ is obtained from the exact nonrelativistic phase-space integral, not from the ultra-relativistic rescaling R_n. The collision term uses the q-generalized thermal average $\langle\sigma v\rangle_q \approx a + b\,\langle v_{\rm rel}^2\rangle_q$, with $\langle v^2\rangle_q$ explicitly defined in Eq. (4.13).

Unlike the first order model in $(q-1)$, the use of exact functions makes a purely analytical treatment unfeasible. Therefore, it is more appropriate to use numerical methods for the analysis, from the computation of observables to the final solution of the Boltzmann equation.

Starting from the condition equating the q-deformed annihilation rate to the q-deformed expansion rate at T_f,

$$\Gamma_{{\rm ann},q}(T_f) \;\simeq\; H_q(T_f), \qquad \Gamma_{{\rm ann},q} \;\equiv\; n_{\chi,{\rm eq},q}(T_f)\,\langle\sigma v\rangle_q(T_f), \tag{4.22}$$

and adopting the partial-wave ansatz (4.5), together with the q-rescaled Hubble rate

$$H_q(T) \;=\; \sqrt{R_\rho(q)}\,H(T), \tag{4.23}$$

one obtains the q-logarithmic transcendental equation for $x_f \equiv m_\chi/T_f$:

$$x_f(q) \;\simeq\; \ln_q\!\left[\frac{g_\chi\, M_{\rm Pl}\, m_\chi}{1.66\,(2\pi)^{3/2}\sqrt{g_*(T_f)\,R_\rho(q)}}\left(a + b\,\langle v_{\rm rel}^2\rangle_q\right)\sqrt{x_f(q)}\right], \tag{4.24}$$

where g_χ is the internal multiplicity of the WIMP, m_χ its mass, $g_*(T_f)$ the effective relativistic degrees of freedom evaluated at T_f, $R_\rho(q)$ the nonextensive deformation of the radiation background defined in Eq. (4.15), and a and b are the s- and p-wave coefficients entering the q-generalized thermally averaged annihilation cross section $\langle\sigma v\rangle_q$. The factor $\langle v_{\rm rel}^2\rangle_q$ is the q-generalized thermal average of the squared relative velocity, evaluated self consistently at Freeze-out.

Freeze-out takes place in the nonrelativistic regime, $x \equiv m_\chi/T \gtrsim \mathcal{O}(20)$, so we do not apply any ultrarelativistic number density map in this computation. The equilibrium density that enters $\Gamma_{{\rm ann},q}$ is obtained from the exact q-generalized phase-space integral of Eq. (3.29), evaluated in the NR limit relevant for decoupling, while the only background rescaling that survives in the Hubble rate is the energy-density factor $H_q = \sqrt{R_\rho(q)}\,H$ with $R_\rho(q)$ defined in Eq. (4.15). In other words, the q-logarithmic structure in Eq. (4.24) comes solely from using the q-exponential equilibrium distribution in the annihilation rate and from inverting the Freeze-out condition with the q-logarithm, not from any UR number-density rescaling. The detailed derivation is provided in Appendix A.6.2.

Chapter 5

Deforming the Neutrino Sector

Once the q-generalized framework for WIMP Freeze-out based on nonextensive statistical mechanics has been constructed, it is natural to look for a phenomenological way to restrict the nonextensive parameter q using Early Universe observables. The purpose of this chapter is to construct an independent radiation era probe of q. While the Relic Abundance is degenerate with the WIMP annihilation parameters, the neutrino contribution to N_{eff} provides a more direct way to test deformations of the relativistic plasma near the MeV scale.

In this chapter, a minimal and phenomenological hypothesis is adopted: to deform only the neutrino sector through the fermionic rescaling $R_\rho^{\text{FD}}(q)$ in the energy density, see Eq. (4.18), while keeping the photon sector without an explicit deformation. This is done in the epoch in which the radiation content is essentially dominated by photons and neutrinos, namely after the reheating associated with electron-positron annihilation [19]. The physical reason is that neutrinos decouple at energies of order MeV and may retain a residual nonextensive imprint that can be parametrized effectively from the primordial plasma, while photons continue to rethermalize and their standard description is preserved. In addition, this choice allows the nonextensive deformation to be mapped directly onto the observable N_{eff}, avoiding modifications of the standard parametrization through which BBN and CMB describe the radiation content, and reducing unnecessary degeneracies that would appear if the whole radiation background were deformed at the same time.

5.1 Standard parametrization of the radiation

The radiation content in this epoch is parameterized as a sum of the neutrino and photon energy density contributions:

$$\rho_r = \rho_\gamma + \rho_\nu = \rho_\gamma\Big(1 + k\, N_{\text{eff}}\Big), \tag{5.1}$$

where ρ_γ is the photon energy density,

$$k = \frac{7}{8}\left(\frac{4}{11}\right)^{4/3}, \tag{5.2}$$

is the factor that contains the Fermi-Dirac contribution (7/8) and the photon reheating factor $(4/11)^{4/3}$ originated from electron-positron annihilation, and N_{eff} is the effective number of neutrino species. As a reference value, we take the Standard Model prediction

$$N_{\text{eff}}^{\text{std}} = 3.0440 \pm 0.0002, \tag{5.3}$$

which includes the standard corrections from non-instantaneous neutrino decoupling and finite-temperature effects [13]. Equation (5.1) provides the baseline radiation parametrization that we deform within the nonextensive framework.

In this work, $N_{\rm eff}^{\rm std}$ is not recomputed. It is used as the standard theoretical reference value around which the nonextensive shift is defined. Therefore, the role of the Tsallis parameter q is to encode an additional effective departure[1] from the Boltzmann-Gibbs baseline, not to replace the standard neutrino decoupling calculation.

5.2 How the Neutrino Sector is Deformed

The deformation introduced here is deliberately minimal. Instead of modifying the full electromagnetic plasma and the neutrino decoupling history simultaneously, we keep the photon sector fixed and assign the nonextensive correction only to the effective neutrino contribution. This choice isolates the impact of the deformation on $N_{\rm eff}$, which is directly constrained by CMB+BAO and can also be compared phenomenologically with inferred BBN values.

Using the fermionic radiation rescaling induced by nonextensivity, $R_\rho^{\rm FD}(q)$, which is defined in Eq. (4.18), and considering fixed photons plus a rescaling of neutrinos only, we define[2]

$$\Delta N_{\rm eff}(q) \equiv \widehat{N}_{\rm eff}(q) - N_{\rm eff}^{\rm std} = \left[R_\nu^{\rm FD}(q) - 1\right] N_{\rm eff}^{\rm std}. \tag{5.4}$$

Here, the hat in $\widehat{N}_{\rm eff}(q)$ denotes the model prediction obtained after applying the nonextensive deformation, in contrast with the standard theoretical reference value $N_{\rm eff}^{\rm std}$ and the observationally inferred values. The corresponding energy densities are written as

$$\rho_{\gamma,q} = \rho_\gamma, \qquad \rho_{\nu,q} = R_\nu^{\rm FD}(q)\rho_\nu^{\rm std}. \tag{5.5}$$

This prescription has a clear analytical advantage: it gives a one-to-one mapping between the nonextensive parameter q and the shift $\Delta N_{\rm eff}$. It affects only the effective neutrino radiation contribution and preserves the standard observational parametrization of the radiation density [28]. Moreover, the photon thermodynamics is not modified, which avoids changing the photon temperature, the definition of the CMB temperature, and the electromagnetic thermal history relevant for recombination.

The extensive limit is recovered exactly. Since

$$\lim_{q\to 1} R_\nu^{\rm FD}(q) = 1, \tag{5.6}$$

one obtains

$$\lim_{q\to 1} \widehat{N}_{\rm eff}(q) = N_{\rm eff}^{\rm std}, \qquad \lim_{q\to 1} \Delta N_{\rm eff}(q) = 0. \tag{5.7}$$

Therefore, the deformation does not introduce a new radiation component. It only rescales the standard neutrino contribution by a factor fixed by the nonextensive distribution.

The validity of this mapping relies on the following assumptions: (i) the deformation is flavor universal, (ii) neutrinos are treated as ultrarelativistic during the relevant epoch, (iii) the photon bath is kept standard after electromagnetic rethermalization in order to avoid tensions with CMB physics, (iv) the standard temperature ratio $T_\nu/T_\gamma = (4/11)^{1/3}$ is used as the baseline, and (v) the deformation is sufficiently small near the MeV scale so that the standard thermal history remains the appropriate reference background. A full treatment beyond this effective

[1] Note: Flavor-dependent nonextensivity is not assumed here, since we adopt a minimal and phenomenological deformation of the neutrino sector. Equivalently, q is not interpreted as originating from a specific microscopic flavor model, but as an effective parameter controlling possible residual departures from extensivity in the decoupled relativistic sector.

[2] This mapping is an effective one parameter deformation of the neutrino radiation density. It does not include a full calculation of neutrino decoupling, finite-temperature QED corrections, or spectral distortions.

Table 5.1: Summary of the data used in the analysis. The cold dark matter abundance is included because it is used in the WIMP relic-abundance sector of this thesis.

Observable	Symbol	Value (1σ)	Experiment/Dataset
Effective radiation (CMB+BAO)	$N_{\rm eff}^{\rm CMB}$	2.99 ± 0.17	Planck 2018 + BAO [4]
Effective radiation (BBN)	$N_{\rm eff}^{\rm BBN}$	2.88 ± 0.16	BBN primordial abundances [10]
Cold Dark Matter density (CMB)	$\Omega_c h^2$	0.120 ± 0.001	Planck 2018, base ΛCDM [4]
Theoretical reference (SM)	$N_{\rm eff}^{\rm std}$	3.0440 ± 0.0002	Neutrino decoupling [13]

mapping would require solving the neutrino decoupling kinetic equations with a nonextensive collision operator, which is beyond the scope of this thesis.[3]

The observational inputs used in this analysis are summarized in Table 5.1. The BBN Gaussian prior is used only as an illustrative phenomenological input. A robust BBN constraint would require computing light element abundances, weak interaction rates, the neutron to proton ratio, and the nuclear reaction network.

We model $\Delta N_{\rm eff}(q)$ as a function of q and visualize the allowed regions under the 1σ intervals of $N_{\rm eff}^{\rm CMB}$ and $N_{\rm eff}^{\rm BBN}$. With this in hand, we perform a combined χ^2 analysis using the BBN and CMB+BAO measurements listed in Table 5.1; for more details, see Appendix B.2.

It is important to stress that $N_{\rm eff}^{\rm std}$ is not treated as an additional observational value, in the χ^2 analysis. It is used only as the theoretical reference value around which the nonextensive shift is defined. The experimental constraints are those associated with BBN and CMB+BAO. The cold dark matter abundance in Table 5.1 is used in the relic-abundance analysis of the WIMP sector. The phenomenological restrictions on q from the deformed neutrino sector are obtained from $N_{\rm eff}^{\rm CMB}$, with $N_{\rm eff}^{\rm BBN}$ used as an illustrative comparison.

[3]Neutrino kinetic decoupling and BBN abundance evolution are related Early Universe problems, but they are not the same calculation. The former concerns the evolution of the neutrino distribution functions, entropy transfer, and spectral distortions, while the latter concerns weak rates and nuclear abundances.

Chapter 6

Results and discussion for constant q

This chapter presents the main results for the constant-q scenario, comparing the first order and exact nonextensive frameworks in WIMP Freeze-out and Relic Abundance. The first order treatment is shown only as a diagnostic approximation, since it is not sufficiently accurate for the quantitative analysis. The exact model provides the main basis for the phenomenological results. Within the exact description, the Relic Abundance remains strongly degenerate with the annihilation parameters, because the setup is model independent. Therefore, $\Omega_{\chi,q}h^2$ should be interpreted mainly as a consistency test of the nonextensive Freeze-out framework, while the most direct constraint on q comes from the radiation era observable ΔN_{eff} through a deformed neutrino sector.

The chapter is organized as follows:

- We solve the Boltzmann equation for $Y_q(x)$ and show its behavior as a function of the dimensionless parameter x for different values of q, considering a WIMP with mass 100 GeV in the first order and exact models; see Fig. 6.1.
- We show the Relic Abundance $\Omega_{\chi,q}h^2$ as a function of the WIMP mass m_χ for different values of q in the first order and exact models; see Fig. 6.2. We also show the Freeze-out point $x_f = m_\chi/T_f$ as a function of m_χ for different values of q; see Fig. 6.3.
- We study the decoupling point from the q-generalized transcendental equation. Using the q-logarithmic equation implied by $\Gamma_{\text{ann},q} \simeq H_q$ with an $s{+}p$ partial-wave ansatz, we solve for $x_f(q)$ on a grid of q at fixed masses $m_\chi = \{100, 500, 1000\}$ GeV; see Fig. 6.4. We also study the sensitivity of the parameter space using a χ^2 fit from the observed Relic Abundance; see Figs. 6.6–6.11.
- We quantify the effects of nonextensivity in the primordial plasma through $R_\rho(q)$ by studying the relativistic degrees of freedom using interpolated tables for $g_{*,q}$ and $g_{*s,q}$ at different values of q; see Fig. 6.5.
- We compare the theory with the observational data of BBN and CMB+BAO given in Table 5.1 by parameterizing radiation through the effective number of neutrinos. We plot the variation $\Delta N_{\text{eff}}(q)$ induced by the factor $R_\nu^{\text{FD}}(q)$ in the deformed neutrino sector, construct $\chi^2_{N_{\text{eff}}}$ with observational data, and obtain phenomenological constraints on q through confidence levels; see Figs. 6.12, 6.13, 6.14a, 6.14b, and Table 6.1.
- We interpret the results and discuss two motivated extensions: a Multi-component dark matter interpretation of under-abundant regions and a dynamical relaxation model in which q is promoted to $q(T)$, recovering extensivity or near-extensivity before BBN. The parameter-space regions are shown in Figs. 6.15, 6.16, and 6.17 for the s-wave dominated scenario, and in Figs. 6.18, 6.19, and 6.20 for the p-wave dominated scenario.

6.1 Freeze-out with Arbitrary q: First Order and Exact

In this section we present the results of the effective generalized Freeze-out calculation in the first order and exact prescriptions. The purpose is not to claim evidence for $q \neq 1$ from the Relic Abundance alone, but to identify how the nonextensive parameter modifies the Freeze-out dynamics and where the first order approximation loses reliability.

6.1.1 Comoving Abundance and decoupling

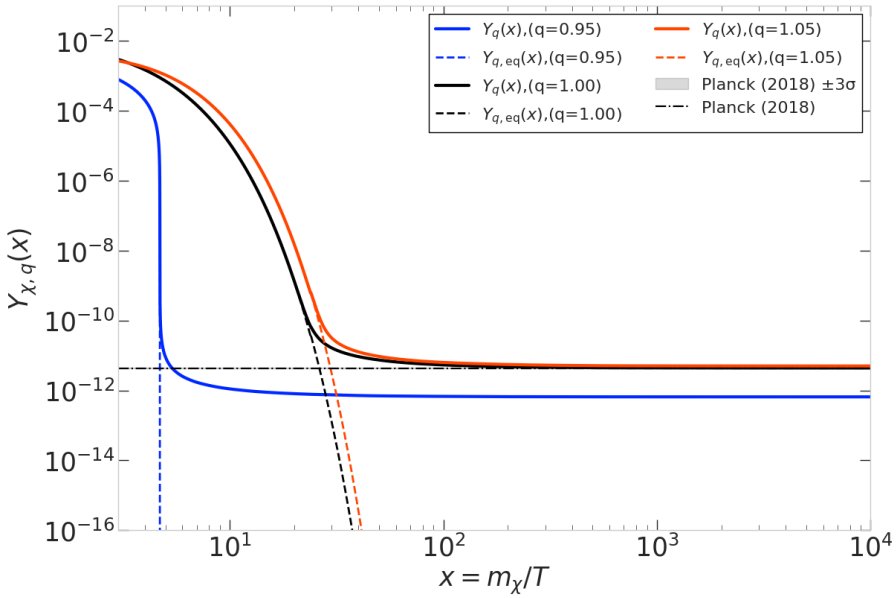

(a) First order approximation.

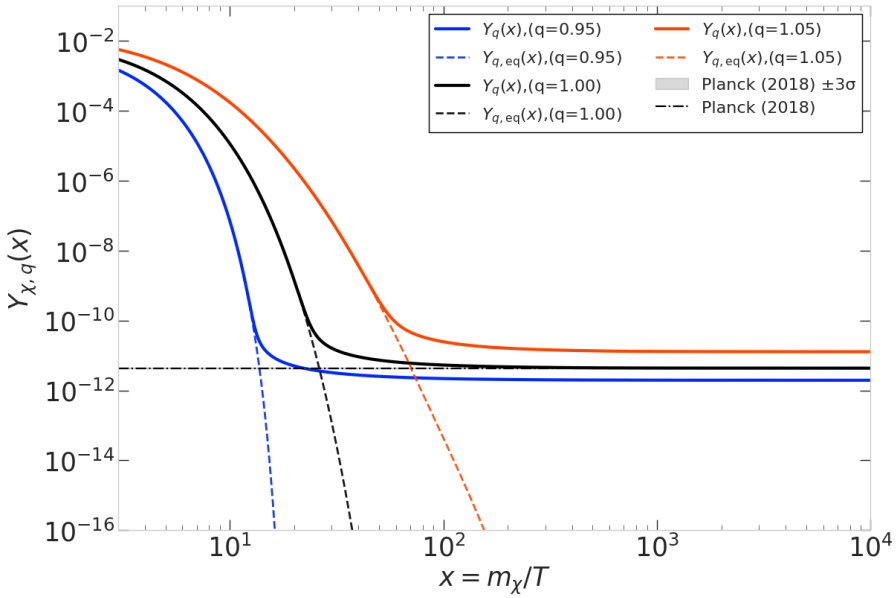

(b) Exact model.

Figure 6.1: **Freeze-out for** $m_\chi = 100$ GeV: comparison between the first order approximation and the exact model. In both, $g_\chi = 4$, $a = 1.825 \times 10^{-9}$ GeV^{-2} and $b = 1.05 \times 10^{-9}$ GeV^{-2} are considered. The black dashed line is the value measured by the Planck satellite, $\Omega_c h^2 = 0.120 \pm 0.001$.

As shown in Fig. 6.1, WIMP decoupling occurs later when $q > 1$, corresponding to larger x_f and therefore smaller T_f for fixed mass, and earlier when $q < 1$, corresponding to smaller x_f and therefore larger T_f. This behavior appears in both models. However, the first order scheme does not accurately reproduce the exact behavior: the approximate distribution function used in (3.16) induces biases in the estimation of x_f and in the trajectory of $Y_q(x)$, as seen in Fig. 3.1. Consequently, first order predictions about the shift of Freeze-out with q should be interpreted with caution. The exact model is the one used for the quantitative interpretation because it consistently captures the power law tails for $q > 1$ and the compact support for $q < 1$.

6.1.2 Relic Abundance versus WIMP mass

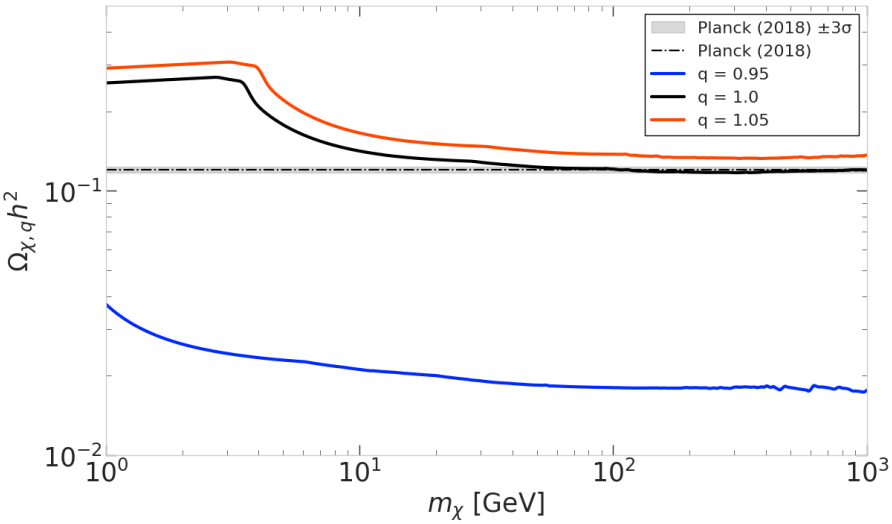

(a) First order approximation.

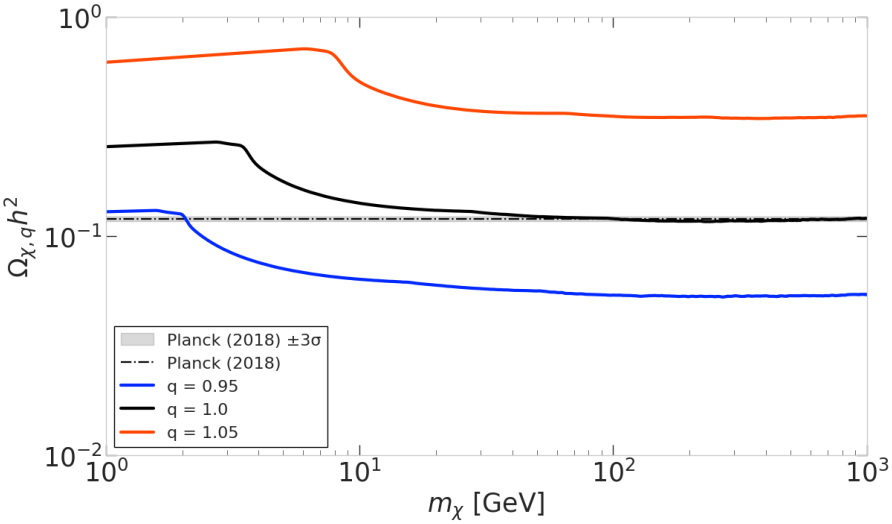

(b) Exact model.

Figure 6.2: **Relic Abundance $\Omega_{\chi,q}h^2$ vs. mass m_χ for different q ($g_\chi = 4$).** The first order approximation and the exact model are shown, respectively. The shaded band and dashed line indicate, respectively, the $\pm 3\sigma$ region and the central Planck value with the same annihilation parameters as in Fig. 6.1.

Figure 6.2 shows that, for fixed annihilation parameters, the Relic Abundance $\Omega_{\chi,q}h^2$ changes with both q and m_χ. The standard case $q = 1$ remains the natural reference point, while

deviations from $q = 1$ modify the thermal history and can move the prediction away from the observed value. This does not by itself exclude $q \neq 1$, because the annihilation parameters are model dependent and can shift the allowed region.

The figure also shows a marked drop when the mass m_χ is such that the decoupling temperature $T_f \simeq m_\chi/x_f$ enters the QCD crossover region, $T \sim$ 150-170 MeV. In that interval the plasma equation of state changes rapidly and the effective degrees of freedom $g_{*,q}(T)$ and $g_{*s,q}(T)$, see Fig. 6.5, decrease notably, altering both $H_q \propto \sqrt{g_{*,q}}\,T^2$ and $s_q \propto g_{*s,q}\,T^3$ in the Boltzmann equation. Since around Freeze-out one approximately has $Y_{\infty,q} \sim H_q/(s_q \langle\sigma v\rangle_q)$, a reduction of $g_{*,q}$ and $g_{*s,q}$ translates into a visible decrease of $\Omega_{\chi,q}h^2$. This effect is purely thermodynamic, intrinsic to the QCD plasma, and should not be confused with the opening or closing of annihilation channels [29, 30].

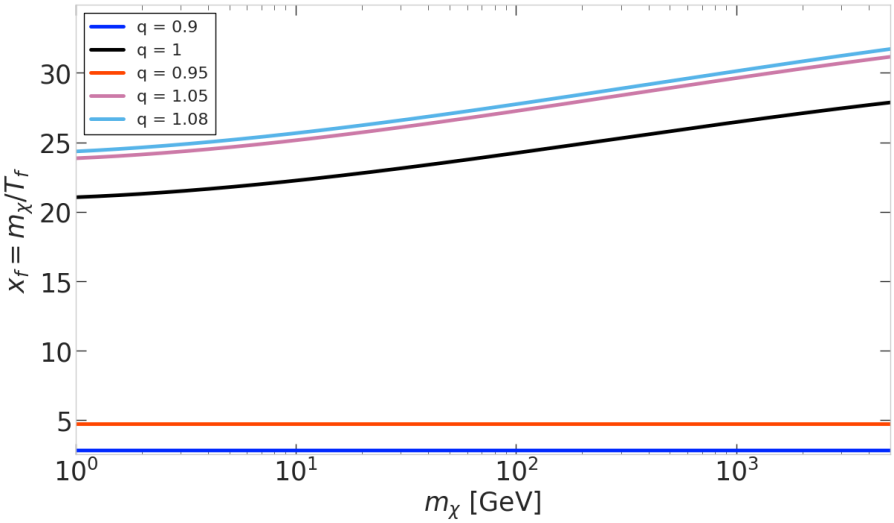

(a) First order approximation.

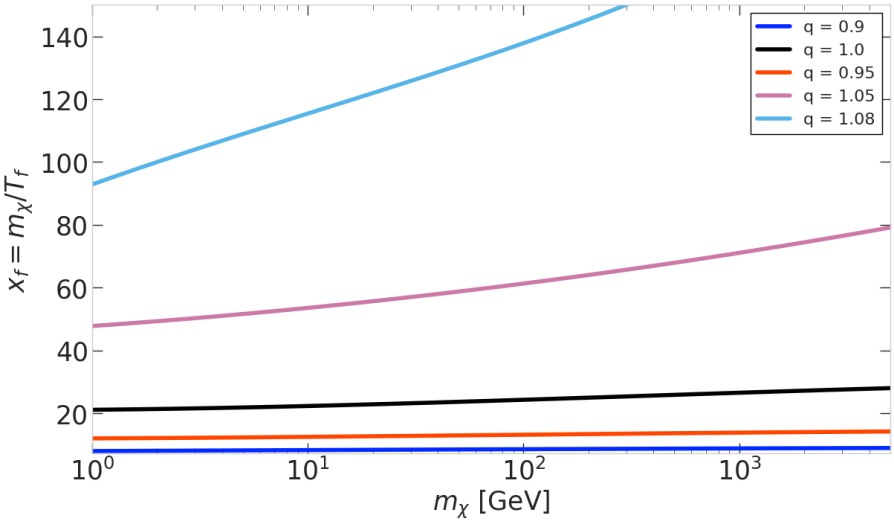

(b) Exact model.

Figure 6.3: **Decoupling $x_f \equiv m_\chi/T_f$ as a function of m_χ for** $\{q = 0.9, 0.95, 1.0, 1.05, 1.08\}$ numerically calculated from the Boltzmann Equation algorithm.

6.1.3 Freeze-out point versus WIMP mass

To study how the parameter q affects the decoupling point x_f without modeling the full process in Fig. 6.1 for all masses, we plot x_f versus m_χ for values of q greater and smaller than unity.

As seen in Fig. 6.3, the first order scheme shows an asymmetric behavior in q. For $q < 1$, the approximately logarithmic scaling of x_f with the mass m_χ is attenuated, whereas for $q > 1$ the effect is closer to a mild rescaling of the $x_f(m_\chi)$ relation. In contrast, the exact model more clearly shows the consequences of nonextensivity: for $q > 1$, the power law tails increase the slope and dispersion of the Freeze-out *locus* in the (m_χ, x_f) plane; for $q < 1$, the compact support mitigates the variation of x_f with m_χ, although without the marked suppression introduced by the first order expansion.

This means that the mass m_χ and the Freeze-out temperature T_f do not scale in the same way. Due to the logarithmic behavior of the decoupling condition, m_χ grows faster than T_f. Consequently, for heavier masses, the decoupling temperature T_f occurs earlier in the thermal history when larger values of q are chosen.

Limitations of the first order model. The analysis developed in the previous subsections shows that the first order scheme is not sufficiently accurate for the phenomenological analysis performed in this work. Therefore, the main results are based on the exact q-distribution model. In particular, the approximation derived from (3.16) does not offer the necessary fidelity to reliably characterize the effects of nonextensivity in the Early Universe. Consequently, from this point onward the numerical results and conclusions are based on the exact model.

6.1.4 Freeze-out point from the q-generalized transcendental equation

We determine the decoupling point by solving the q-generalized transcendental condition, Eq. (4.24), consistently with the exact q-exponential used in the phase-space distributions. Figure 6.4 shows $x_f(q)$ for $m_\chi = \{100, 500, 1000\}$ GeV together with the canonical band $15 \leq$

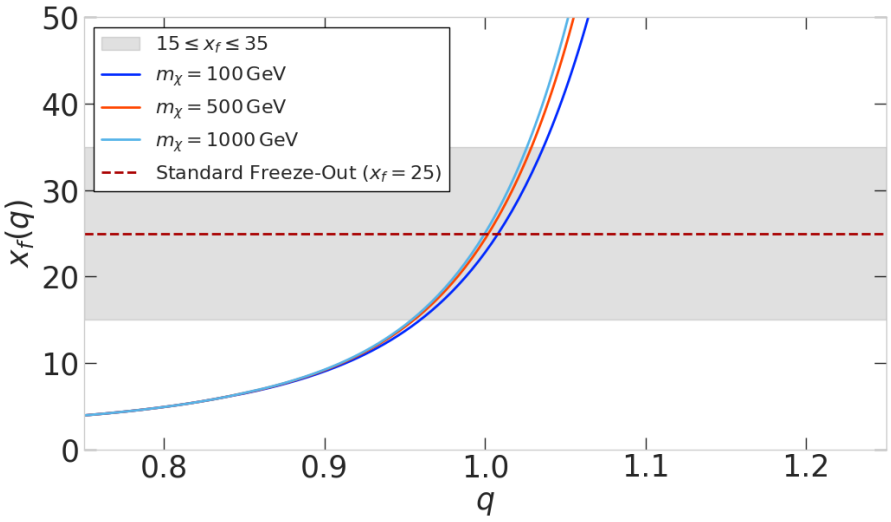

Figure 6.4: **Freeze-out parameter x_f versus nonextensivity q for fixed WIMP masses** ($m_\chi = \{100, 500, 1000\}$ GeV). Curves are obtained by solving the q-generalized transcendental condition Eq. 4.24, $R_\rho(q)$ computed from the exact q-exponential, and $\langle\sigma v\rangle_q \approx a + b\,\langle v_{\mathrm{rel}}^2\rangle_q$. The grey band indicates a "canonical" range $15 \leq x_f \leq 35$. For fixed m_χ, x_f grows with q, reflecting the nonlinear q-logarithmic inversion that dominates over the H_q increase.

$x_f \leq 35$. For fixed mass, x_f increases monotonically with q: although $H_q \propto \sqrt{R_\rho(q)}$ also grows with q, which by itself would tend to reduce x_f, the q-logarithmic inversion in Eq. (4.24) dominates in the relevant range and produces a net increase of x_f. The same pattern holds when setting $b = 0$, which shows that the main driver is the $\ln_q$ inversion rather than the p-wave term. This agrees with the Freeze-out points obtained from the q-Boltzmann solver; see Fig. 6.3. In the implementation we keep only the radiation-background rescaling through $R_\rho(q)$, i.e. $H_q = \sqrt{R_\rho(q)}\, H$, while the nonrelativistic equilibrium density $n_{\chi,\mathrm{eq}}$ is left unmodified at Freeze-out. For $q > 1$, the exact q-exponential $e_q(-z)$, with $z \equiv E/T$, develops power law tails, Eq. (3.26), which increase the velocity moments entering $\langle\sigma v\rangle_q = a + b\,\langle v^2\rangle_q$, Eqs. (4.5) and (4.13). Together with the background rescaling $H_q = \sqrt{R_\rho(q)}\, H$, Eqs. (4.19) and (3.25), the net effect in Eq. (4.24) is an increase of x_f.

For $q < 1$, $e_q(-z)$ vanishes for $z \geq z_{\max} = 1/(1-q)$, Eqs. (3.26) and (3.28), which suppresses the velocity moments entering $\langle\sigma v\rangle_q$, while $R_\rho(q) < 1$ implies $H_q = \sqrt{R_\rho(q)}\, H < H$, Eqs. (4.19) and (3.25). With $n_{\chi,\mathrm{eq},q}$ kept in its nonrelativistic form, the reduction in $\Gamma_{\mathrm{ann},q} \sim n_{\chi,\mathrm{eq},q}\,\langle\sigma v\rangle_q$

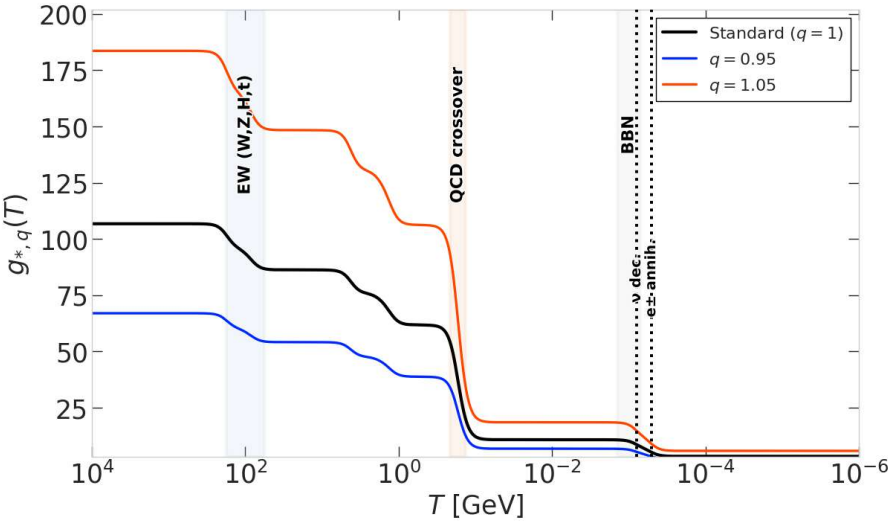

(a) $g_{*,q}(T)$ (effective).

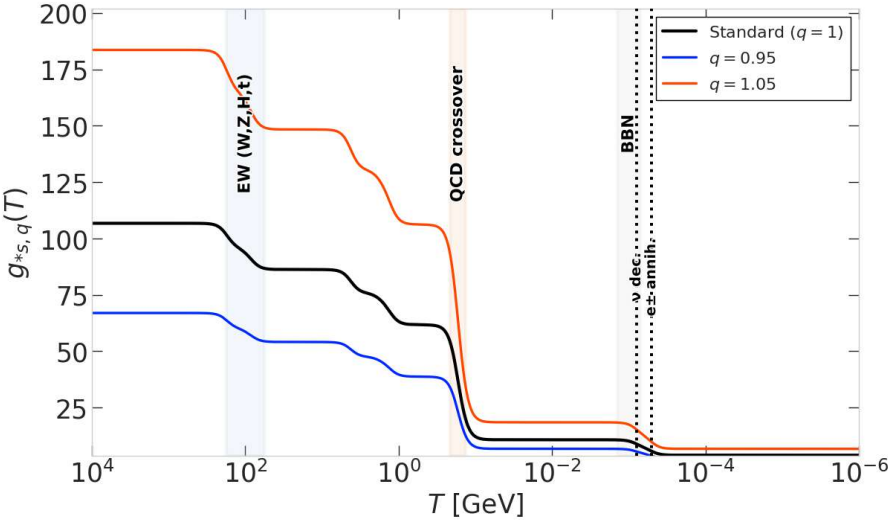

(b) $g_{*s,q}(T)$ (entropic).

Figure 6.5: **Degrees of freedom in the plasma with q-statistics**. We show $q = 1$ and $q = \{0.95,\ 1.05\}$. In our convention $g_{*,q}(T) = R_\rho(q)\, g_*(T)$ and $g_{*s,q}(T) = R_\rho(q)\, g_{*s}(T)$; the main thermal transitions (EW, QCD crossover, BBN, $e^\pm$, ν) are indicated [1]. Valid for $q < 5/4$.

arises through $\langle\sigma v\rangle_q$ and dominates over the decrease of H_q, so $\Gamma_{\mathrm{ann},q}/H_q$ drops below unity at higher temperatures and decoupling occurs earlier as q decreases.

6.1.5 Degrees of freedom of the primordial plasma

Figure 6.5 shows the evolution of the effective $g_{*,q}$ and entropic $g_{*s,q}$ degrees of freedom in the q-generalized framework. While the thermal transitions of the Standard Model are preserved, the factor $R_\rho(q)$ introduces a vertical rescaling of the curves. This effect requires care in its physical interpretation, because it can mimic a change in the number of relativistic particle species present in the primordial plasma. This point is discussed further in connection with the N_{eff} restriction on q and the motivation for a relaxation model. Note that the entropic degrees of freedom differ slightly from the effective ones when electron-positron annihilation occurs because it injects heat and entropy into the photon background; this can be seen in the tables in Appendix B.1.

6.1.6 Impact of nonextensivity through statistical analysis

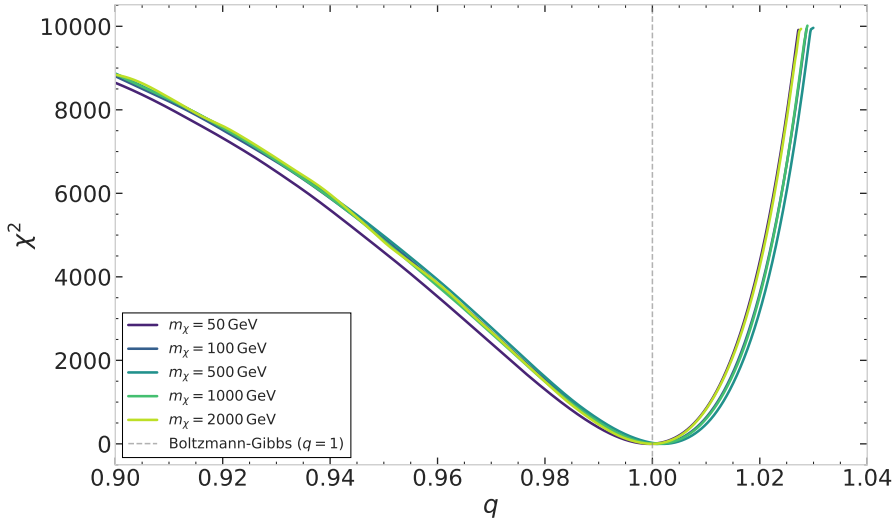

Figure 6.6: **Absolute $\chi^2(q)$ profiles at fixed cross section (mass scan).** Smoothed curves for several m_χ values illustrate the global fit structure and the approximate degeneracy in q when only $\Omega_c h^2$ is used as constraint; the common minimum indicates nearly equivalent solutions across masses. A representative fixed thermally averaged cross section $\langle\sigma v\rangle_q = 2 \times 10^{-9}\mathrm{GeV}^{-2}$ was used.

To assess how nonextensivity impacts the results, we perform a simple statistical analysis against the observed Relic Abundance. In our model independent setup, multiple combinations (a, q, m_χ) can reproduce the Planck value $\Omega_{\chi,q}h^2 = 0.120 \pm 0.001$ (see Table 5.1), so the constraint from a single observable is underdetermined in the three-dimensional space. Consequently, the global minimum of a χ^2 fit is not unique but organized along a valley of nearly equivalent solutions.

To explore the parameter space, we take the simplest case, s-wave domination, and perform two complementary scans. At fixed annihilation cross section $\langle\sigma v\rangle$, $\chi^2(q)$ is evaluated on a grid in q for a list of WIMP masses m_χ. At fixed mass m_χ, $\chi^2(q)$ is computed for a list of cross sections $\langle\sigma v\rangle$. These two slices make the (q, m_χ, a) landscape tractable, revealing the sensitivity of the Relic Abundance under parameter modifications. The results of both scans can be seen in Figs. 6.6, 6.7, 6.8, and 6.9.

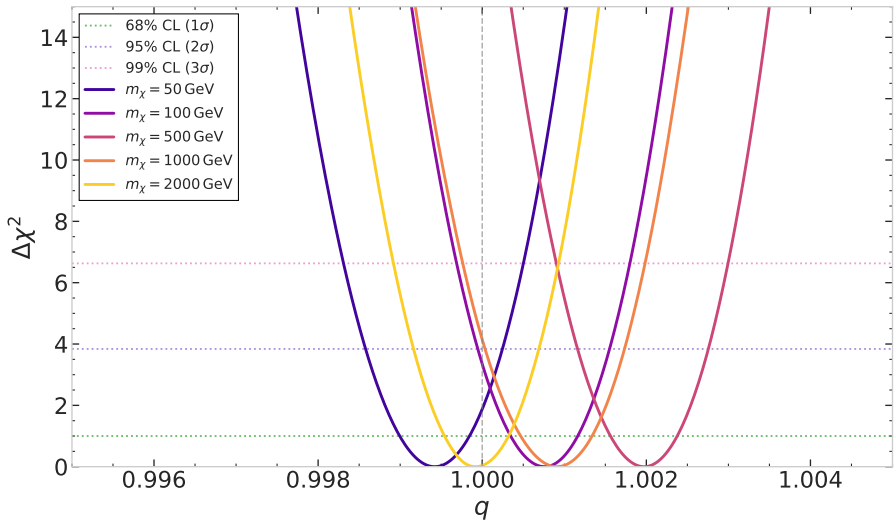

Figure 6.7: **Profile likelihood $\Delta\chi^2(q)$ (mass scan).** We show $\Delta\chi^2(q) = \chi^2(q) - \chi^2_{\min}$ for the same masses as above. Horizontal lines mark the 68%, 95%, and 99% confidence levels for one effective parameter, defining the allowed q intervals around q_{best}.

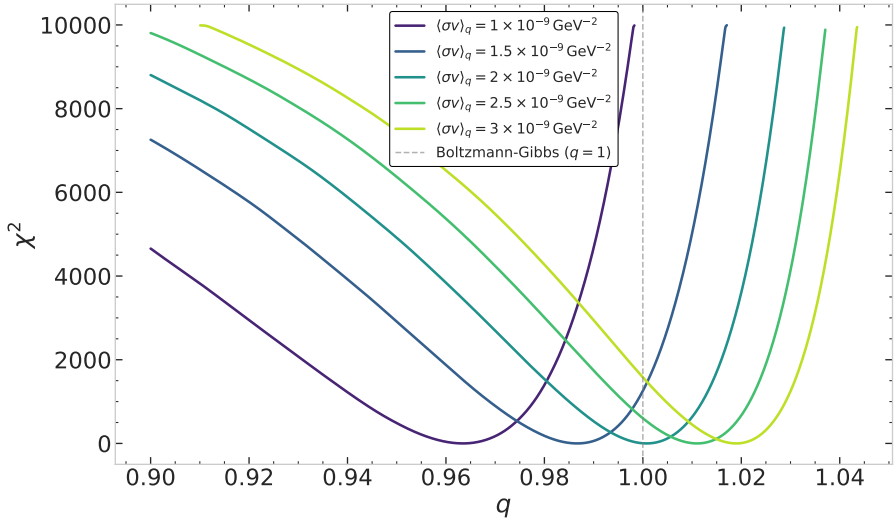

Figure 6.8: **Absolute $\chi^2(q)$ profiles at fixed mass (cross-section scan).** For a representative $m_\chi = 100$ GeV, curves are shown for different s-wave amplitudes $a \equiv \langle\sigma v\rangle_{s\text{-wave}}$ (in GeV^{-2}). The smoothing highlights a valley of nearly equivalent (q, a) solutions reproducing $\Omega_\chi h^2$, underscoring the role of a as a nuisance parameter in a model independent setup.

In the scans, nonextensivity is markedly more sensitive to variations of the thermally averaged annihilation cross section $\langle\sigma v\rangle_q$ than to the WIMP mass. At fixed m_χ, the absolute and profile curves versus q exhibit separated minima for different a-values, where a is the s-wave amplitude; see Figs. 6.8 and 6.9. This indicates that modest changes in a shift the preferred q, reflecting a pronounced (q, a) trade-off: a behaves as a nuisance parameter that traces an extended valley of nearly degenerate solutions reproducing $\Omega_c h^2$. In contrast, when $\langle\sigma v\rangle_q$ is held fixed and only m_χ varies, the corresponding minima cluster tightly and the $\Delta\chi^2$ bands overlap broadly, keeping the preferred q close to the extensive limit $q \simeq 1$; see Figs. 6.6 and 6.7. Physically, at fixed a, the mass mainly enters through the logarithmic dependence of the Freeze-out parameter x_f, whereas changing a directly rescales the annihilation rate and thus the Relic Abundance normalization, which couples more strongly to q. This scan is structured this way because the dark matter mass and annihilation cross section are currently unconstrained

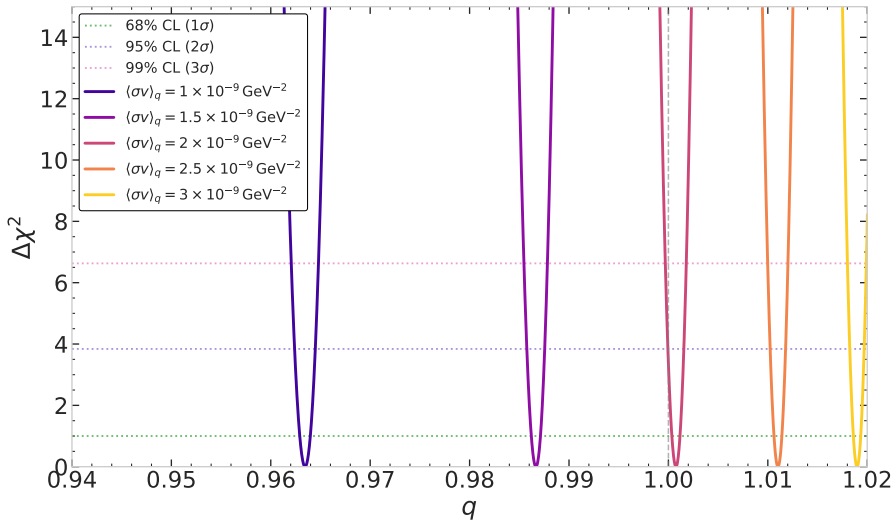

Figure 6.9: **Profile likelihood $\Delta\chi^2(q)$ (cross-section scan).** The $\Delta\chi^2(q)$ curves corresponding to the previous panel are shown with 68%, 95%, and 99% confidence-level lines, from which the confidence intervals in q are read for each choice of a. The compatible solutions trace an extended (q, a) valley, showing that the Relic Abundance alone does not provide a unique constraint on q.

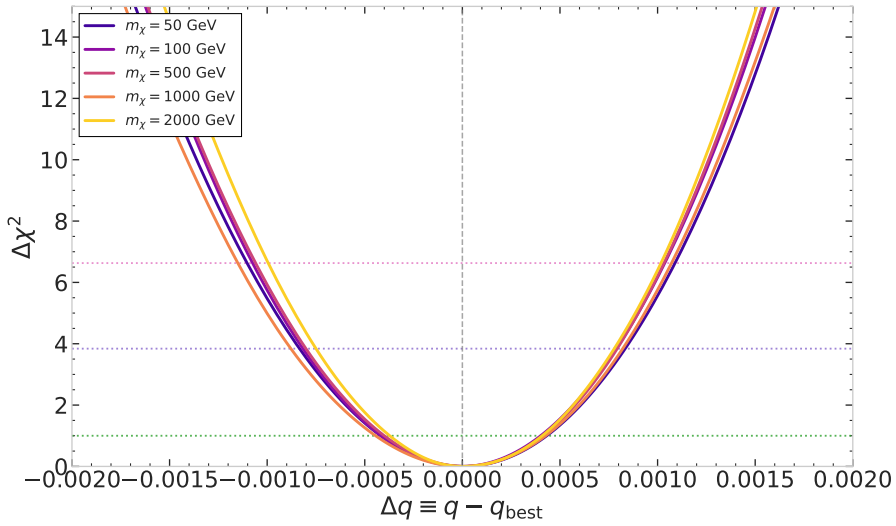

Figure 6.10: **Profile likelihood $\Delta\chi^2(q)$ (mass scan, centered).** We show $\Delta\chi^2(q) \equiv \chi^2(q) - \chi^2_{\rm min}$ for $m_\chi = \{50, 100, 500, 1000, 2000\}$ GeV with the horizontal axis centered at $q - q_{\rm best}$. Horizontal lines indicate the 68%, 95%, and 99% confidence levels for one effective parameter. The clustering of minima across masses keeps the favored q close to the extensive limit, consistent with the weak mass sensitivity discussed in the text.

experimentally; independent measurements would reduce these degeneracies.

The differing widths of the $\Delta\chi^2(q)$ profiles in the mass and cross-section scans indicate that the standard Freeze-out hierarchy is retained: variations in the thermally averaged cross section $\langle\sigma v\rangle_q$ are the primary lever modifying the Relic Abundance, whereas changes in m_χ mainly shift the minimum without appreciably broadening the profile. To visualize this point, we center the curves in Figs. 6.10 and 6.11 by defining $\Delta q \equiv q - q_{\rm best}$, where $q_{\rm best}$ is the best value of q that reproduces the observed Relic Abundance $\Omega_c h^2 = 0.120 \pm 0.001$ in each case.

The main feature of this statistical analysis is that the Relic Abundance does not provide a robust and unique constraint on the nonextensive parameter q by itself. In a model inde-

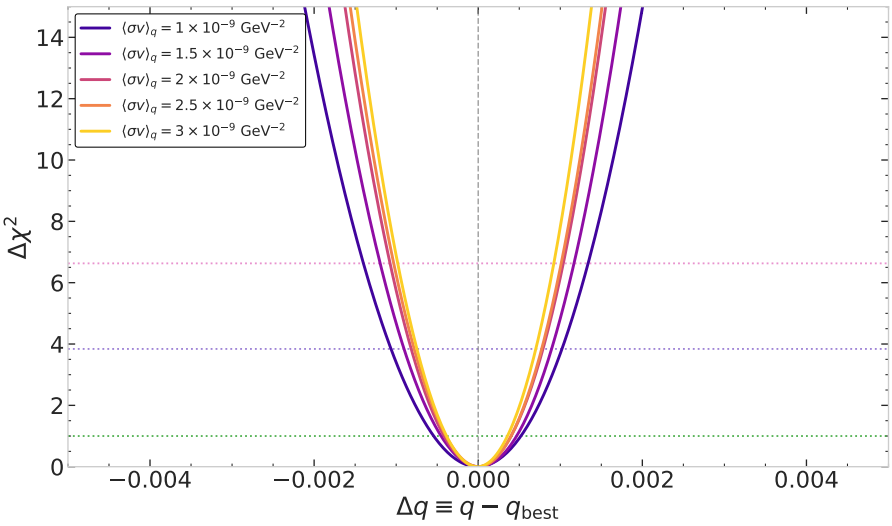

Figure 6.11: **Profile likelihood $\Delta\chi^2(q)$ (cross-section scan, centered).** For $m_\chi = 100\,\mathrm{GeV}$, curves correspond to different s-wave amplitudes a (legend shows $\langle\sigma v\rangle_q$ values in GeV^{-2}); the horizontal axis is centered at $q - q_{\rm best}$. Modest changes in a shift the preferred q by amounts larger than the 68-95% bands, tracing an extended (q, a) valley of nearly degenerate solutions. Horizontal lines denote the 68%, 95%, and 99% confidence levels.

pendent setup, different combinations of (q, a, b, m_χ) can reproduce the observed value of $\Omega_c h^2$, generating degeneracies in the parameter space. Therefore, Relic Abundance data alone should be interpreted primarily as a consistency test of the nonextensive Freeze-out framework rather than as evidence for a particular value of q.

6.1.7 Results and Constraints on q from a deformed neutrino sector by using BBN and CMB-BAO Data

At this point, the statistical analysis based on Relic Abundance alone remains affected by the intrinsic degeneracy between nonextensivity and annihilation microphysics. For this reason, it is necessary to move to an observable that probes the radiation background more directly. This motivates the next step of the analysis, namely the mapping of the nonextensive deformation onto $\Delta N_{\rm eff}$ through a deformed neutrino sector.

Table 6.1 summarizes the intervals with respect to the confidence levels for the nonextensivity parameter q via an upper and lower bound and a best fit given by $q_{\rm best}$ from a χ^2-type fit[1] combining the CMB+BAO and BBN data of Table 5.1. These results and Figs. 6.14a and 6.14b constrain the nonextensive parameter to lie very close to the extensive limit $q = 1$; small departures remain allowed within the quoted confidence intervals.

It is useful to clarify the statistical meaning of this fit. In the deformed neutrino sector analysis, the only free phenomenological parameter is the Tsallis parameter q, while $N_{\rm eff}^{\rm std}$ is kept fixed as the theoretical reference value and is not treated as an additional data. The observables entering the combined fit are the BBN and CMB+BAO determinations of $N_{\rm eff}$ listed in Table 5.1. Therefore, for the combined analysis one has two observational inputs and one free parameter, leaving one effective degree of freedom. In contrast, the separate BBN and

[1]The $\chi^2_{\rm BBN}(q)$ and $\chi^2_{\rm CMB+BAO}(q)$ profiles are symmetric in the residuals involving $N_{\rm eff}^{\rm std} + \Delta N_{\rm eff}(q)$, but they are not required to be symmetric as functions of q. In this work, the dependence on q enters through $\Delta N_{\rm eff}(q) = \left[R_\nu^{\rm FD}(q) - 1\right] N_{\rm eff}^{\rm std}$, where $R_\nu^{\rm FD}(q)$ is obtained from the exact q-deformed fermionic distribution. Since $q > 1$ gives power-law tails while $q < 1$ gives compact-support behavior, both regimes are not mirror deformations around $q = 1$. Therefore, $\Delta\chi^2_{N_{\rm eff}}(q)$ can be asymmetric in q, and the shift of $q_{\rm best}$ toward $q < 1$ follows from the fact that the central values of $N_{\rm eff}^{\rm BBN}$ and $N_{\rm eff}^{\rm CMB}$ used here lie below $N_{\rm eff}^{\rm std} = 3.044$.

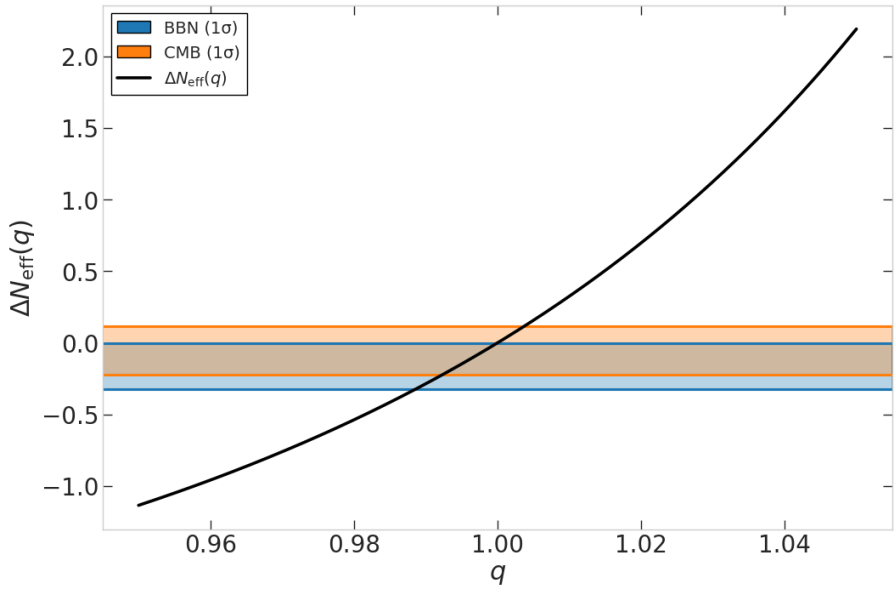

Figure 6.12: **Nonextensive prediction for $\Delta N_{\rm eff}(q)$ (black curve) from the neutrino rescaling** $R_\nu^{\rm FD}(q)$, using $\Delta N_{\rm eff}(q) = (R_\nu^{\rm FD}(q) - 1)N_{\rm eff}^{\rm std}$ with $k = \frac{7}{8}(4/11)^{4/3}$ and $N_{\rm eff}^{\rm std} = 3.044$. The horizontal bands show the 1σ regions of BBN (blue, ± 0.16) and CMB+BAO (orange, ± 0.17). Values of q compatible at 1σ with both sets are those where the black curve falls within the intersection of both bands.

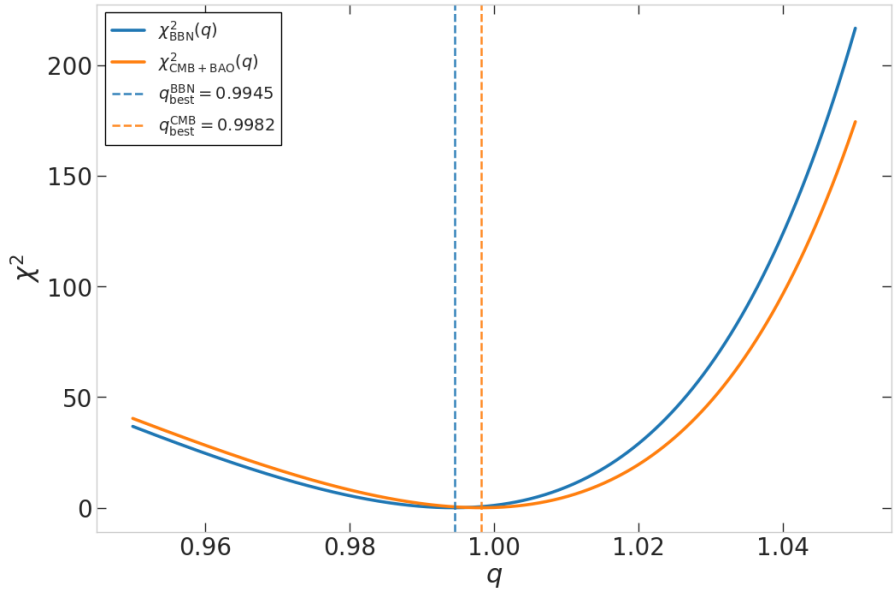

Figure 6.13: **Curves of χ^2 vs. q from $N_{\rm eff}$.** The blue and orange curves correspond to $\chi^2_{\rm BBN}(q)$ and $\chi^2_{\rm CMB+BAO}(q)$, respectively. The vertical dotted lines indicate the minima: $q^{\rm BBN}_{\rm best} = 0.9945$ and $q^{\rm CMB}_{\rm best} = 0.9982$. Both datasets favor values close to the extensive limit $q = 1$.

CMB+BAO profiles contain one value and one fitted parameter, so they should be interpreted mainly as one parameter likelihood profiles for q, rather than as independent goodness of fit tests. This is different from the Relic Abundance analysis, where the observable $\Omega_{\chi,q}h^2$ depends simultaneously on q, m_χ, and the annihilation parameters a and b. In that case, one observable cannot isolate the effect of q because variations in the annihilation microphysics can compensate changes in the nonextensive background. The $N_{\rm eff}$ analysis is therefore less degenerate: once the effective neutrino-sector prescription is fixed, the shift $\Delta N_{\rm eff}(q)$ is controlled only by q.

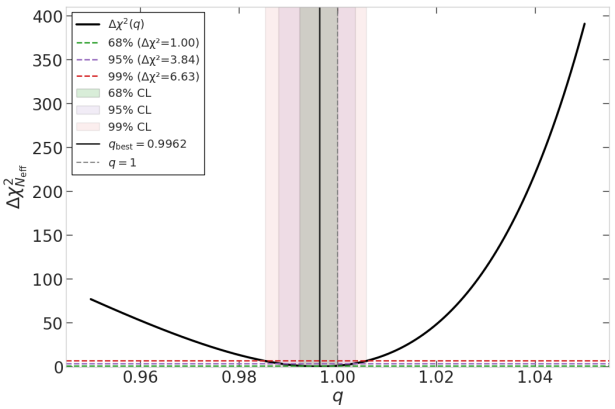

(a) $\Delta\chi^2_{N_{\rm eff}}(q)$ **curve for the deformed neutrino sector**. Confidence levels 68%, 95%, and 99% (horizontal lines) and the corresponding intervals in q (shaded bands) around the minimum $q_{\rm best}$ are shown; the gray line marks $q = 1$.

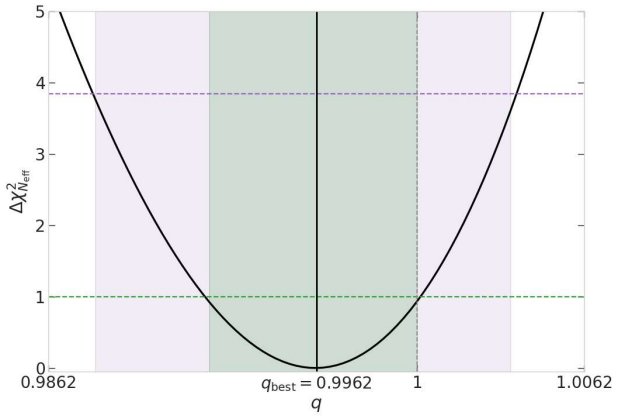

(b) $\Delta\chi^2_{N_{\rm eff}}(q)$ **for the deformed neutrino sector**. Confidence levels 68%, 95%, and 99% (horizontal lines) and the corresponding intervals in q (shaded bands) around the minimum $q_{\rm best}$ are shown; the gray line marks $q = 1$.

Figure 6.14: **χ^2-type fit to constrain the Tsallis Parameter q by finding its best value**: the left panel shows $\Delta\chi^2_{N_{\rm eff}}$ as a function of q, while the right panel shows a zoom around the best value $q_{\rm best}$.

This is why radiation era observables provide a cleaner phenomenological restriction on the nonextensive parameter than the Relic Abundance alone.

It is important to stress that the best-fit values slightly different from unity should not be interpreted as evidence for $q \neq 1$. The allowed regions remain close to the extensive case, and $q = 1$ is not excluded at the quoted confidence levels. In this analysis, q is interpreted as an effective parameter encoding possible long range interactions, correlations, or memory effects in the early plasma. For more details of the construction of the fit, see Appendix B.2. Therefore, this analysis suggests that small residual nonextensive effects in the neutrino sector are not excluded by the data used in Table 5.1, but it does not establish evidence for nonextensivity.

Table 6.1: Constraints obtained for q and the best-fit minimum for BBN and CMB+BAO.

Dataset	$q_{\rm best}$	68% CL	95% CL	99% CL
BBN	0.9945	[0.9888, 0.9998]	[0.9825, 1.005]	[0.9785, 1.008]
CMB+BAO	0.9983	[0.9925, 1.004]	[0.9863, 1.009]	[0.9820, 1.012]
Combined	0.9962	[0.9927, 1.000]	[0.9891, 1.004]	[0.9868, 1.006]

Taking the largest deviation from $q_{\rm best}$ in the combined χ^2 analysis in Table 6.1, we have

$$|q - 1| \leq 1.09 \times 10^{-2} \quad (95\%\ \text{CL}), \tag{6.1}$$

$$|q - 1| \leq 1.32 \times 10^{-2} \quad (99\%\ \text{CL}), \tag{6.2}$$

which define the phenomenological intervals obtained in this work for the nonextensive parameter q at $T \sim 1$ MeV or later epochs from a deformed neutrino sector by using nonextensive statistical mechanics.[2] These bounds should be treated as phenomenological, since the full neutrino decoupling calculation is not performed in this work.

[2]These intervals are phenomenological bounds within the effective neutrino sector deformation adopted in this thesis. They should not be read as final BBN or neutrino decoupling bounds on q.

Table 6.2: Comparison of the constraints on the nonextensivity parameter q obtained from different physical methodologies and the present work.

Methodology	**Bound on q**	**Reference**
Generalized Planck Radiation Law	$\lvert q-1\rvert \leq 0.41 \times 10^{-4}$	[31]
Gravitational constant uncertainty	$\lvert q-1\rvert \leq \mathcal{O}(10^{-4})$	[32]
Early Universe: Primordial Helium and Weak interactions	$\lvert q-1\rvert \leq 4.01 \times 10^{-3}$	[33]
Early Universe: Primordial Helium and Weak interactions	$\lvert q-1\rvert \leq 2.08 \times 10^{-5}$	[34]
Deformation of the neutrino sector	$\lvert q-1\rvert \leq 1.32 \times 10^{-2}$	This Work

Unlike the Relic Abundance analysis, the $\Delta N_{\rm eff}$ mapping provides a more direct and less degenerate probe of nonextensivity. The resulting BBN and CMB+BAO bounds from $N_{\rm eff}$ consistently drive q toward the extensive limit, showing that physically viable departures from BG statistics near the late radiation era must remain close to unity. This establishes radiation era observables, rather than Relic Abundance alone, as the strongest phenomenological handle on the nonextensive parameter in this work.

For instance, studies based on a generalized Planck radiation law have derived a tight bound of $|q-1| \leq 0.41 \times 10^{-4}$ [31], while uncertainties in the gravitational constant suggest a limit of the order of 10^{-4} [32]. Furthermore, observables from the Early Universe, specifically regarding primordial helium abundance and weak interactions, provide some of the most stringent constraints, with values ranging from $|q-1| \leq 4.01 \times 10^{-3}$ [33] down to 2.08×10^{-5} [34]. In this context, our analysis of the deformation of the neutrino sector gives a complementary phenomenological bound of $|q-1| \leq 1.32 \times 10^{-2}$. Collectively, these results suggest that nonextensive corrections relevant to late radiation era cosmology must remain close to the extensive limit, as seen in Table 6.2.

6.2 Interpretation of the results and motivated extensions

The results obtained so far suggest a clear hierarchy in the phenomenology of the constant-q framework. On the one hand, the exact treatment must be preferred over the first order approximation. On the other hand, Relic Abundance predictions alone do not isolate the value of q, because a, b and m_χ are not measured independently in this model-independent setup, whereas radiation era observables constrain it much more directly. These conclusions naturally motivate two extensions of the framework: a Multi-component interpretation of under-abundant results and a dynamical nonextensive parameter that relaxes toward the extensive limit.

6.2.1 Multi-component Dark Matter

In the exact Tsallis framework with constant q, standard WIMP-like candidates can freeze out with a Relic Abundance below the observed value for the fixed benchmark annihilation parameters used in Fig. 6.2. This should not be interpreted as a generic prediction for all parameter choices. Rather than forcing agreement by overtuning annihilation microphysics or invoking special mechanisms, one possible interpretation is that the dark matter sector may be

multi-component: the missing fraction could be supplied by an additional stable species that freezes out independently in the same nonextensive bath [12].

This viewpoint is also practical for phenomenology: each component carries a fraction of the total density, which directly rescales experimental expectations, linearly for direct detection and quadratically for indirect searches. As a minimal baseline, two independent species could suffice, one under-abundant candidate plus a complementary relic, to recover the observed total while keeping the constant-q setup clean and model independent. Next, the parameter space of the generalized WIMP Freeze-out model is explored to identify regions of under and overabundance of dark matter.

Parameter space: s-wave dominated scenario

For illustrative purposes, we explore the three dimensional parameter space (q, a, m_χ) under the assumption of s-wave dominance, $b = 0$, in order to identify the regions that lead to an under-abundant Relic Abundance as well as those yielding an overabundance. This is achieved through three independent two dimensional scans, in which one of the three parameters is held fixed while the remaining two are varied, as shown in Figs. 6.15, 6.16, and 6.17. In all panels we display the Relic Abundance on a logarithmic scale, $\log_{10}(\Omega_{\chi,q}h^2)$. Accordingly, the Planck 2018 central value reads $\log_{10}(\Omega_c h^2) = -0.921$, and the corresponding $\pm 3\sigma$ band is given by $\log_{10}(\Omega_c h^2) \in [-0.932, -0.910]$. These scans provide a convenient way to identify under-abundant regions, which can be interpreted within Multi-component dark matter scenarios motivated by particle physics models in an s-wave dominated scenario. For example, two independent dark matter candidates could evolve in the plasma and decouple independently, satisfying $\Omega_1 h^2 + \Omega_2 h^2 = \Omega_c h^2$.

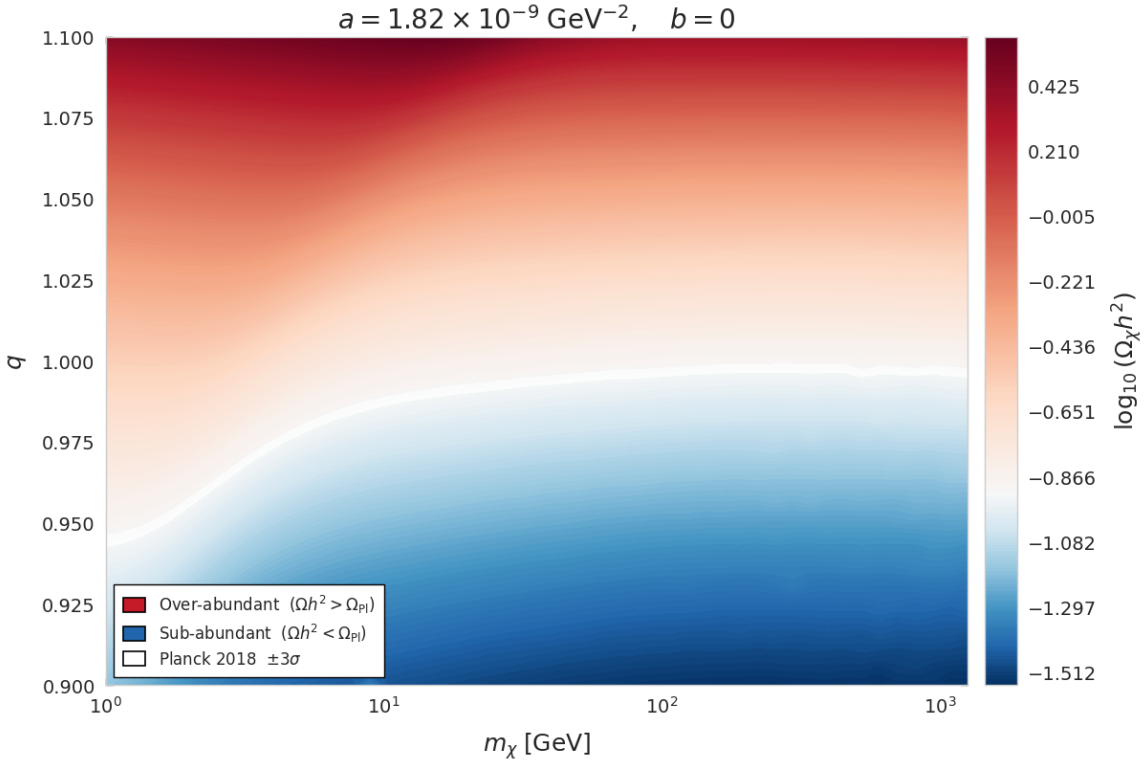

Figure 6.15: **Parameter-space scan in the** (m_χ, q) **plane**. For a fixed s-wave amplitude $a = 1.82 \times 10^{-9}\,\mathrm{GeV}^{-2}$ (with $b = 0$). The color scale shows $\log_{10}(\Omega_{\chi,q}h^2)$ and the Planck 2018 $\pm 3\sigma$ contour delineates the region consistent with the observed Relic Abundance.

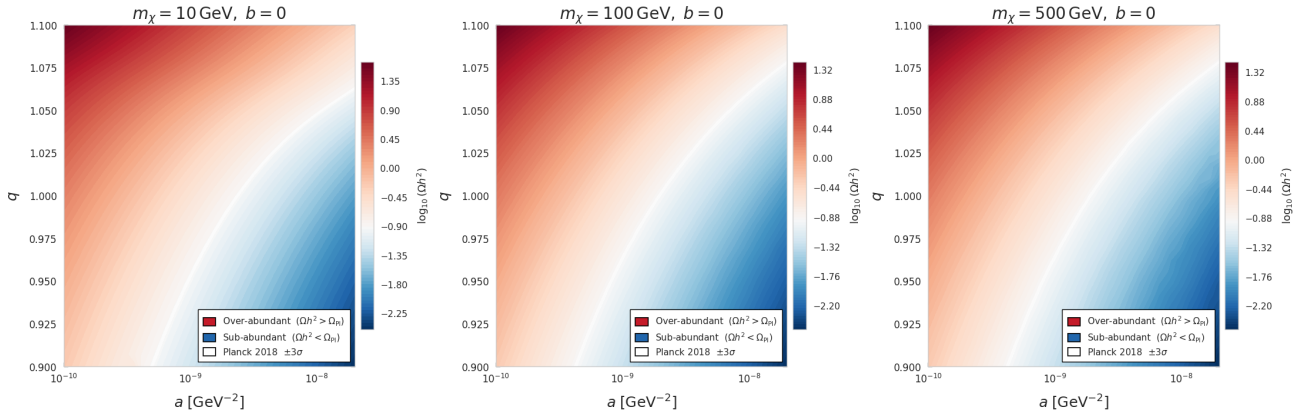

Figure 6.16: **Parameter-space scan in the (a, q) plane.** For fixed WIMP masses $m_\chi = \{10, 100, 500\}$ GeV under s-wave dominance ($b = 0$). The colormap encodes $\log_{10}(\Omega_{\chi,q}h^2)$ and the Planck 2018 $\pm 3\sigma$ contour identifies the locus compatible with the observed Cold dark matter abundance, separating over and under-abundant regions as indicated in the legend.

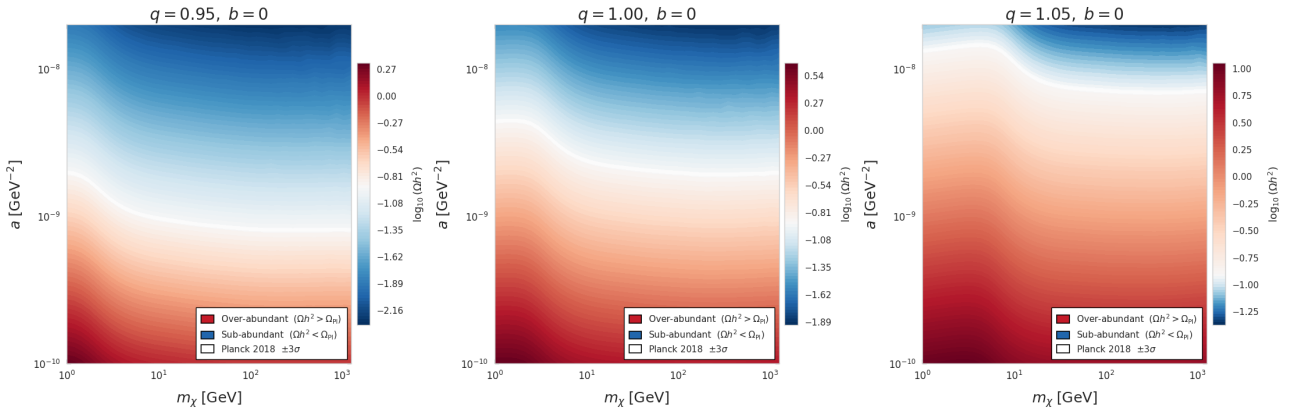

Figure 6.17: **Parameter-space scan in the (m_χ, a) plane.** For fixed nonextensivity $q = \{0.95, 1.0, 1.05\}$ assuming s-wave dominance ($b = 0$, hence $\langle\sigma v\rangle_q \simeq a$). The colormap shows $\log_{10}(\Omega_{\chi,q}h^2)$; the white contour marks the Planck 2018 $\pm 3\sigma$ band around the observed value, separating over-abundant ($\Omega_{\chi,q}h^2 > \Omega_{\mathrm{Pl}}h^2$) from under-abundant ($\Omega_{\chi,q}h^2 < \Omega_{\mathrm{Pl}}h^2$) regions.

Parameter space: p-wave dominated scenario

For completeness, we repeat the analysis in the p-wave dominated regime, where $\langle\sigma v\rangle_q \simeq b\langle v_{\mathrm{rel}}^2\rangle_q$. In this case, the mean value of the relative velocity squared, $\langle v_{\mathrm{rel}}^2\rangle$, plays a central role because its structure from Eq. (4.13) depends on both the nonextensive parameter q and the WIMP mass m_χ. This modifies the dynamics of the parameter space shown in Figs. 6.18, 6.19, and 6.20.

Within the exact p-wave framework, the appearance of two disconnected Planck-compatible branches in the (q, m_χ) plane at sufficiently large b indicates that the Relic Abundance becomes a non-monotonic function of q, as seen in Fig. 6.18. This is physically plausible because q simultaneously deforms the equilibrium distribution, the kinetic moment entering $\langle\sigma v\rangle_q$, and the expansion rate H_q. Nevertheless, the branch located in the $q < 1$ sector should be interpreted more cautiously, since compact-support effects make that regime numerically less robust.

In the exact p-wave scenario, with $a = 0$ and $\langle\sigma v\rangle_q \simeq b\,\langle v_{\mathrm{rel}}^2\rangle_q$, these parameter-space maps show how $\Omega_{\chi,q}h^2$ changes under the combined effect of q, m_χ, and b. In the (q, m_χ) plane, increasing b lowers the Relic Abundance and progressively opens under-abundant regions, while for sufficiently large b the Planck-compatible band may split into disconnected branches,

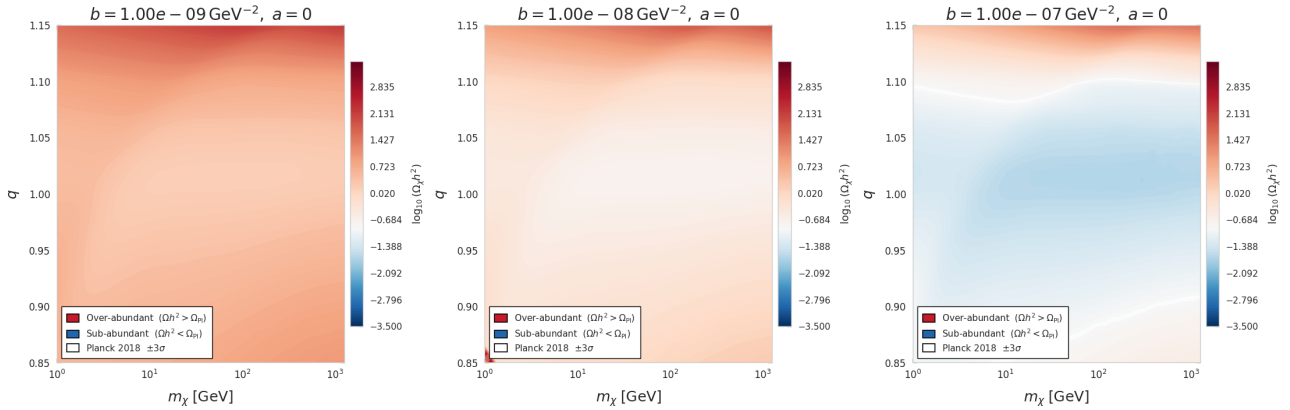

Figure 6.18: **Parameter-space maps in the (q, m_χ) plane for the exact p-wave scenario with $a = 0$ and $\langle\sigma v\rangle_q \simeq b\langle v_{\rm rel}^2\rangle_q$.** The three panels correspond to fixed values of the p-wave coefficient, $b = 10^{-9}$, 10^{-8}, and $10^{-7}\,\mathrm{GeV}^{-2}$, respectively. The color scale represents $\log_{10}(\Omega_\chi h^2)$, with red regions indicating over-abundance and blue regions indicating under-abundance relative to the observed dark matter density. The white band marks the Planck 2018 $\pm 3\sigma$ interval. These plots illustrate how the Relic Abundance changes as a function of the nonextensive parameter q and the WIMP mass m_χ for different p-wave annihilation strengths.

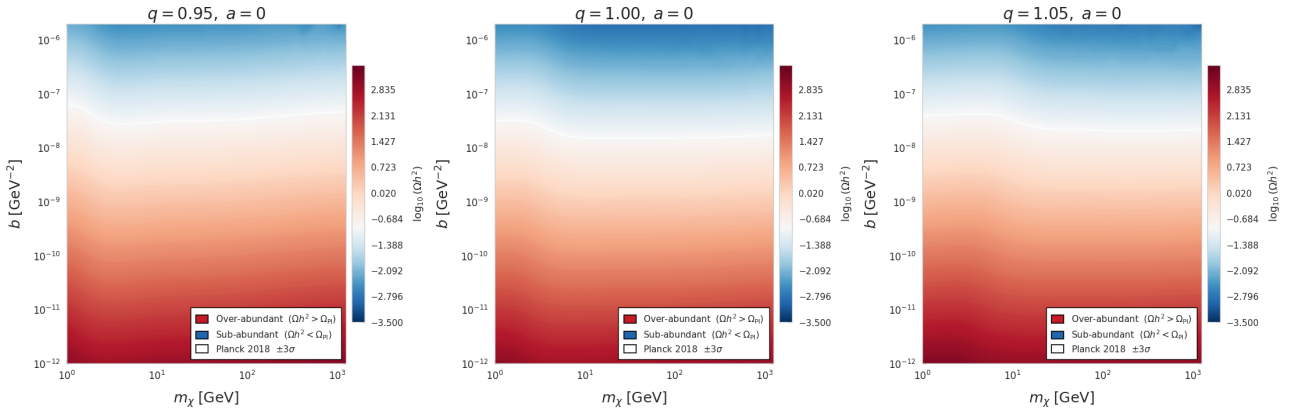

Figure 6.19: **Contour plots of the Relic Abundance in the (m_χ, b) plane for the exact p-wave scenario with $a = 0$.** The three panels correspond to fixed values of the nonextensive parameter, $q = 0.95$, 1.00, and 1.05. The color scale shows $\log_{10}(\Omega_\chi h^2)$, while the white band denotes the Planck 2018 $\pm 3\sigma$ region. Red areas correspond to over-abundant configurations and blue areas to under-abundant ones. These maps show how the allowed range of the p-wave coefficient b depends on the WIMP mass and on the choice of the nonextensive parameter q.

indicating a non-monotonic dependence on q. In the (m_χ, b) plane, the main effect is controlled by b, whereas the dependence on m_χ is milder over the range explored. In the (b, q) plane, the transition from over-abundance to under-abundance becomes explicit for fixed m_χ. Small localized distortions near the lower edge of the $q < 1$ region should be interpreted as numerical artifacts associated with the compact-support regime of the exact q-distribution, while the global structure of the maps remains useful for the qualitative interpretation of the parameter space.

6.2.2 Dynamical nonextensive parameter

The results for the primordial plasma, Fig. 6.5, together with the bounds on q, Eqs. (6.1)–(6.2), indicate that by the epoch of BBN and thereafter the nonextensivity parameter must

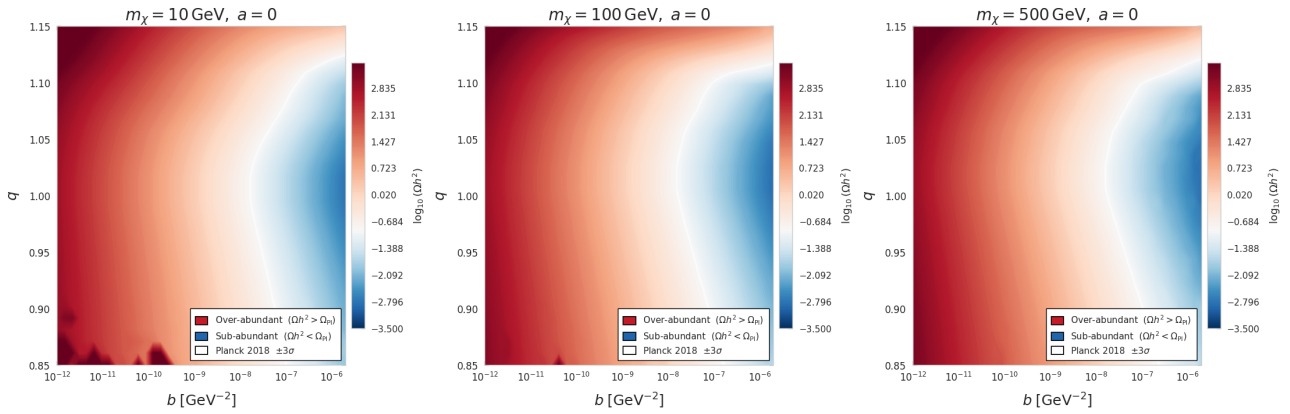

Figure 6.20: **Parameter-space maps in the (b, q) plane for the exact p-wave scenario with $a = 0$ and fixed WIMP masses $m_\chi = 10$, 100, and 500 GeV**, from left to right. The color scale represents $\log_{10}(\Omega_\chi h^2)$, with the white band indicating the Planck 2018 $\pm 3\sigma$ interval. Red regions correspond to over-abundance and blue regions to under-abundance. These plots highlight the interplay between the p-wave coefficient b and the nonextensive parameter q in determining the final thermal Relic Abundance for representative WIMP masses.

lie very close to the extensive limit, $q \simeq 1$. At the same time, the q-generalized H-theorem implies that the stationary, or attractor, solutions of the kinetic equation are precisely the q-equilibrium distributions, Eq. (3.10). These two facts motivate a dynamical picture in which the early plasma could have exhibited a nonzero departure $|q - 1| > 0$ at high temperatures, while entropy production and frequent collisions may drive the system toward the extensive regime. In other words, consistency between late-time radiation constraints and kinetic theory motivates introducing a relaxation trajectory $q(T)$ connecting an initial value $q_{\rm i}$ at $T \gg$ MeV to $q \simeq 1$ by $T \sim$ MeV.

In the Freeze-out and primordial-plasma context, the results obtained here do not exclude the possibility that larger departures from extensivity occurred at earlier stages of the Universe, provided that the parameter relaxes toward the observationally allowed region before BBN. This implication is further explored in the next chapter.

Chapter 7

Dynamical nonextensive parameter

Having established the thermodynamic framework of the primordial plasma and evaluated the strong observational restrictions on a constant Tsallis parameter, this chapter addresses the theoretical challenge of this work: the evolution of nonextensivity. As discussed in previous chapters, the tension between the possible presence of nonextensive correlations at early times and the near-extensive limit demanded by the bounds obtained from a deformed neutrino sector makes a strictly constant nonextensive parameter difficult to maintain phenomenologically. Therefore, in this chapter, we propose and develop a phenomenological formulation where the nonextensive parameter acquires a temperature-dependent dynamics, $q(T)$. We explore how this transition affects the thermal non-linearity of the system and assume that, under a separation of timescales, the plasma may be approximated as evolving through quasi-stationary states. Under this assumption, consistency with the generalized H-theorem can be preserved locally in temperature.

7.1 Minimal proposals for a dynamical Tsallis parameter

The bounds obtained from the deformed neutrino sector indicate that the nonextensive parameter must be close to the extensive limit near the MeV scale. However, this does not exclude the possibility that larger deviations from extensivity occurred at earlier temperatures. For this reason, we introduce two minimal phenomenological profiles for $q(T)$. The first one is a logarithmic interpolation in temperature, useful as a simple monotonic relaxation between two boundary values. The second one is a sigmoid profile, useful to localize the variation of $q(T)$ around a transition scale, such as EWSB or the QCD crossover.

Logarithmic function. Assuming adiabatic expansion of the Universe, it is convenient to approximate the variation of q with a linear relaxation toward $q \simeq 1$ in logarithmic temperature. This connects an initial value $q_{\rm high} \neq 1$ at high temperature with a final value $q_{\rm low} = 1$ at $T \sim$ MeV, consistently with the bounds obtained previously. The function has the form

$$q(T) = A \ln T + B, \quad \frac{dq}{d\ln T} = A, \tag{7.1}$$

where $q = q_{\rm high} \neq 1$ at an initial temperature $T_{\rm high}$ and $q = q_{\rm low} = 1$ at $T_{\rm low} \sim$ MeV as a simplifying choice consistent with the bounds obtained near the MeV scale. From these boundary conditions, the constants A and B are

$$A = \frac{q_{\rm high} - 1}{\ln\left(T_{\rm high}/T_{\rm low}\right)}, \quad B = 1 - A\ln(T_{\rm low}). \tag{7.2}$$

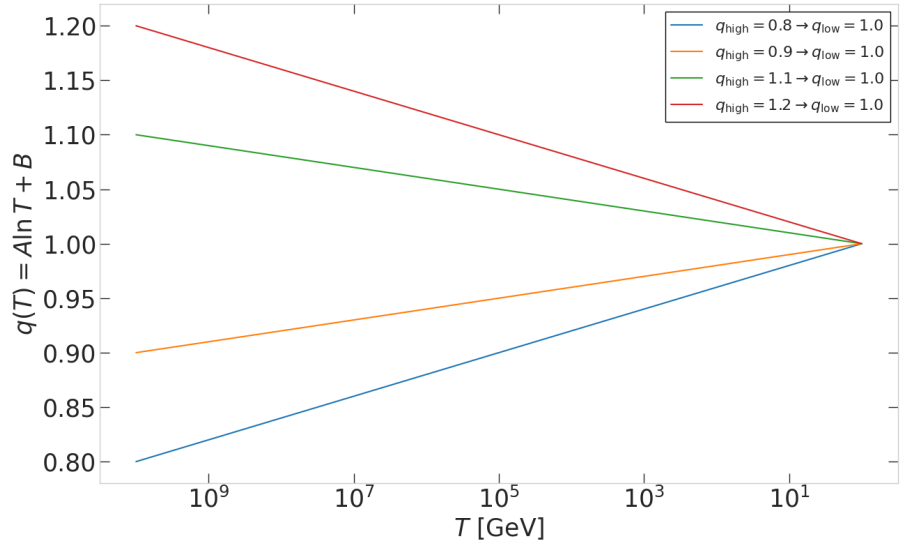

Figure 7.1: **Dynamical nonextensive parameter from Eq. (7.1):** for different values of q_{high}, the profile relaxes toward the extensive value $q_{\text{low}} = 1$, consistently with the bounds obtained in Eq. (6.1) at $T_{\text{low}} \sim$ MeV.

Replacing A and B in Eq. (7.1), one obtains

$$q(T) = 1 + (q_{\text{high}} - 1)\frac{\ln(T/T_{\text{low}})}{\ln(T_{\text{high}}/T_{\text{low}})}. \tag{7.3}$$

In the limit $T \to T_{\text{low}} \sim$ MeV, the extensive case is recovered, $q = 1$, as shown in Fig. 7.1.

Sigmoid function. Alongside the logarithmic proposal, we adopt a sigmoid-type profile based on the logistic map

$$P(x) = \frac{1}{1 + e^{-x}}, \tag{7.4}$$

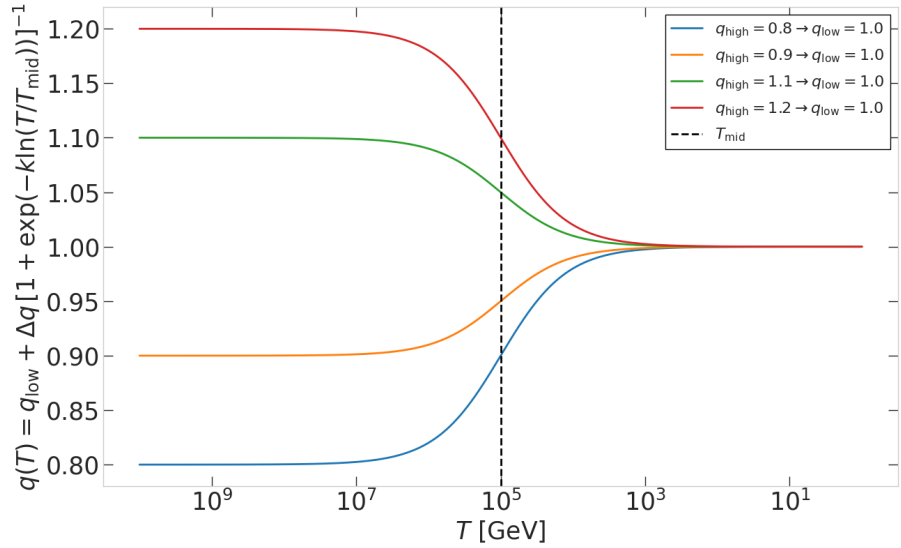

Figure 7.2: **Dynamical nonextensive parameter from Eq. (7.5):** for different values of q_{high}, the profile relaxes toward the extensive value $q_{\text{low}} = 1$, consistently with the bounds obtained in Eq. (6.1) at $T \sim$ MeV. A sigmoid of this kind allows one to control the sharpness through k and the transition scale through T_{mid}.

and define

$$q(T) = q_{\rm low} + \frac{\Delta q}{1+\exp[-k\,x]}, \qquad x \equiv \ln(T/T_{\rm mid}), \quad \Delta q \equiv q_{\rm high} - q_{\rm low}, \tag{7.5}$$

where $q_{\rm high}$ is the value approached at early times and $q_{\rm low}$ is the value that must satisfy the bounds (6.1) or (6.2) at BBN. The parameter $T_{\rm mid}$ sets the transition scale and $k > 0$ controls its sharpness. This sigmoid structure gives direct control over the evolution with temperature and keeps the interpretation of each parameter transparent, as shown in Fig. 7.2 for a generic case.

This function obeys the logistic ODE

$$\frac{dq}{d(\ln T)} = \frac{k}{\Delta q}\,(q - q_{\rm low})(q_{\rm high} - q), \tag{7.6}$$

which we refer to as the free logistic ODE for $q(T)$. Eq. (7.5) is its exact solution and no external pulses or sources are included.

7.2 Propagation to the distribution function

The functions in Eqs. (7.1) and (7.5) are introduced in order to propagate a temperature-dependent nonextensive parameter into the q-generalized distribution functions of Eq. (3.10). We first study the behavior of the resulting dynamical q-exponential using the finite-domain, or compact-support, property of the Tsallis formalism [35]. Then, we insert this structure into the distribution functions for Maxwell-Boltzmann (MB), Fermi-Dirac (FD), and Bose-Einstein (BE) statistics. Finally, we analyze the induced non-linearity by computing logarithmic derivatives of the dynamical q-exponential.

7.2.1 Generalized distribution functions with a dynamical nonextensive parameter

The explicit form of the $q(T)$-generalized distribution function is written as

$$f_{q(T)} = \frac{1}{\Big[1 + \big(q(T)-1\big)\beta(E-\mu)\Big]^{\frac{1}{q(T)-1}} + \xi}, \tag{7.7}$$

where $q(T)$ can be either (7.1) or (7.5). Here, $\xi = 0$ corresponds to Maxwell-Boltzmann statistics, $\xi = +1$ to Fermi-Dirac statistics, and $\xi = -1$ to Bose-Einstein statistics. For simplicity, we refer to these functions as $q(T)$-generalized distribution functions, or $q(T)$-GDFs.

The denominator preserves the structure of a q-exponential, but now with a temperature-dependent nonextensive parameter. Rewriting Eq. (7.7), one obtains

$$f_{q(T)} = \frac{1}{\Big[e_{q(T)}(-\beta(E-\mu))\Big]^{-1} + \xi}, \quad e_{q(T)}(x) \equiv \Big[1 + \big(1-q(T)\big)x\Big]_+^{\frac{1}{1-q(T)}}. \tag{7.8}$$

The notation $[\cdots]_+$ denotes the positive part of the argument, ensuring that the q-exponential remains real in the compact-support regime.

Using $\beta = 1/T$ and defining $\Delta = E - \mu$, the dynamical q-exponential becomes

$$e_{q(T)}(-\beta(E-\mu)) = e_{q(T)}\left(-\frac{\Delta}{T}\right) \equiv \left[1 - \big(1-q(T)\big)\frac{\Delta}{T}\right]_+^{\frac{1}{1-q(T)}}. \tag{7.9}$$

This definition will be useful for qualitative purposes. Following the standard convention in the Tsallis framework, see [35], we define the dynamical q-exponential for negative arguments as

$$e_{q(T)}(-x) \equiv \Big[1-(1-q(T))\,x\Big]_{+}^{\frac{1}{1-q(T)}}, \qquad \lim_{q(T)\to 1} e_{q(T)}(-x) = e^{-x}. \tag{7.10}$$

For $x = \beta\Delta > 0$, the condition for real values requires $1-(1-q(T))x > 0$. This constraint is always satisfied if $q(T) \geq 1$, whereas for $q(T) < 1$ it imposes the lower bound $q(T) > 1-1/x$. As this bound is approached from above, the q-exponential vanishes, reflecting the compact-support feature of the $q < 1$ regime. In contrast, for positive arguments the standard q-exponential exhibits an upper bound $q > 1 + 1/x$ [35].

7.2.2 Dynamical q-exponential

Figure 7.3 shows the inverse of Eq. (7.10), which appears in the denominator of the $q(T)$-GDFs in Eq. (7.8). The curves are evaluated for several fixed values of $x = \beta\Delta$ and for the two proposed profiles of the nonextensive parameter, Eqs. (7.1) and (7.5). This comparison illustrates how the temperature dependence of $q(T)$ modifies the effective Boltzmann factor entering the distribution function.

7.3 Implication: Increase in Non-linearity

In this section, we study how the promotion $q \to q(T)$ introduces an additional source of non-linearity. To motivate this point, let us recall the example used by Tsallis in terms of differential equations [23]. Considering an equation of the form

$$\frac{dy}{dx} = y^q, \tag{7.11}$$

where q is the nonextensive parameter, one obtains a non-linear solution given by the q-exponential $e_q(x)$. Therefore, the non-linearity is induced by q, and in the limit $q \to 1$ the ordinary exponential behavior is recovered.

This behavior can be visualized through logarithmic derivatives. For the standard fixed-q case, the slope and curvature are

$$\frac{d}{dx}\ln e_q(x) = \frac{1}{1+(1-q)x}, \tag{7.12}$$

and

$$\frac{d^2}{dx^2}\ln e_q(x) = -\frac{1-q}{[1+(1-q)x]^2}. \tag{7.13}$$

Thus, for $q \neq 1$ the slope is not constant and the curvature is non-zero. In our cosmological context, $x \propto 1/T$, so the temperature evolution already induces a contribution through $dx(T)/dT$. When q is promoted to a temperature-dependent parameter, a second contribution appears through $dq(T)/dT$. Schematically,

Total non-linearity = Tsallis contribution with varying T + dynamical contribution from $q(T)$.

To quantify this effect, we take the derivative with respect to the temperature T, applying the chain rule:

$$\frac{d}{dT}\ln e_q(-x(T))^{-1} = \frac{\partial \ln e_q(-x(T))^{-1}}{\partial x(T)}\frac{dx(T)}{dT} + \frac{\partial \ln e_q(-x(T))^{-1}}{\partial q(T)}\frac{dq(T)}{dT}. \tag{7.14}$$

This yields the slope

$$\frac{d}{dT}\ln e_q(-x(T))^{-1} = \underbrace{-\frac{x(T)}{T\left[1-(1-q(T))\,x(T)\right]}}_{\text{Tsallis contribution with varying } T} + \underbrace{\left[-\frac{x(T)}{(1-q(T))\left[1-(1-q(T))\,x(T)\right]} - \frac{\ln\left[1-(1-q(T))\,x(T)\right]}{(1-q(T))^2}\right]\frac{dq(T)}{dT}}_{\text{dynamical contribution from } q(T)}. \tag{7.15}$$

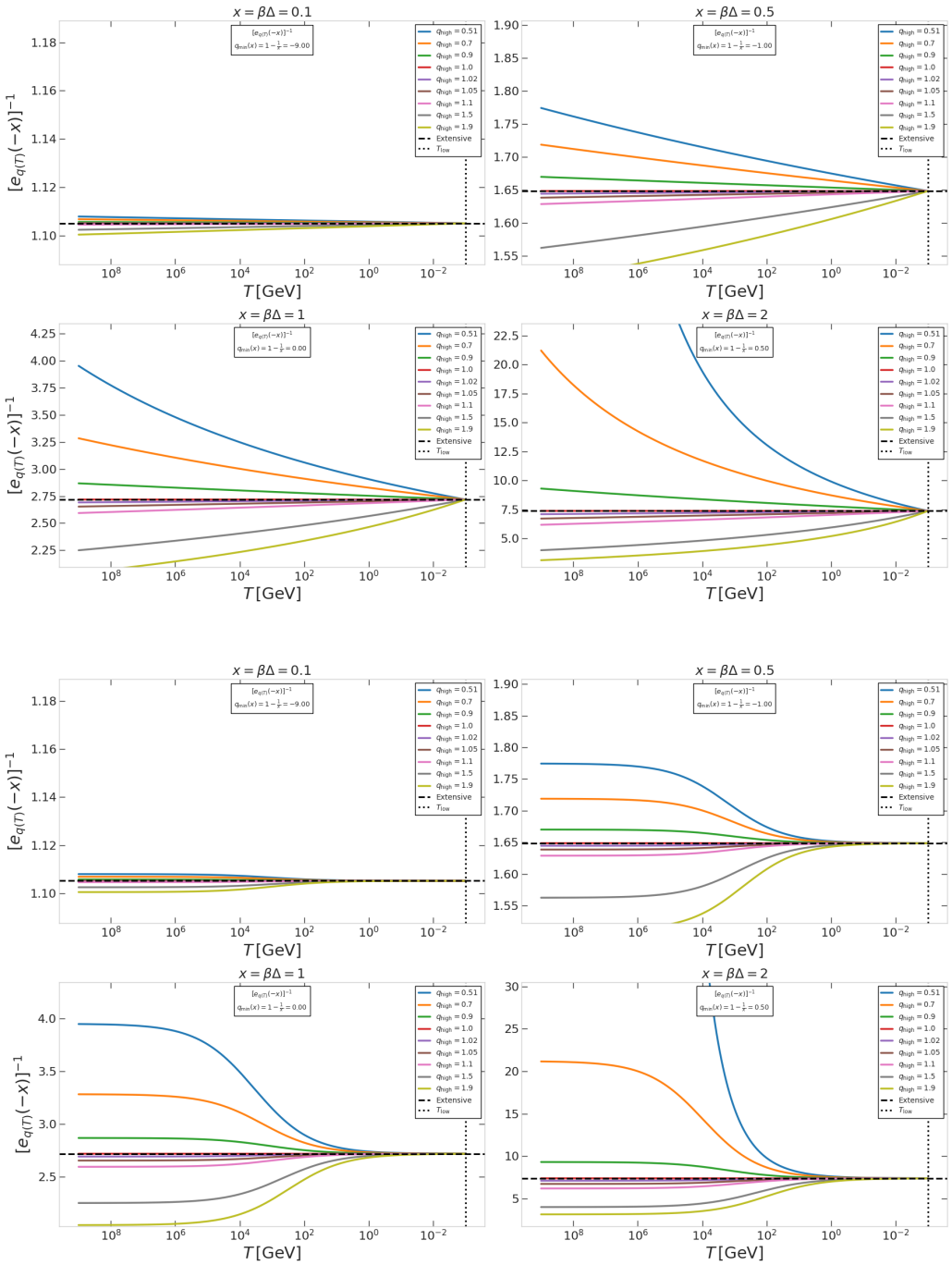

Figure 7.3: **Inverse dynamical $q(T)$-exponential in the distribution function.** $[e_{q(T)}(-x)]^{-1}$ as a function of T for $x = \beta\Delta = \{0.1, 0.5, 1, 2\}$. Top: $q(T) = A\ln T + B$. Bottom: sigmoid $q(T)$. In both cases, $T \in [10^{-3}, 10^{9}]$ GeV, $q_{\text{low}} = 1$, and $q_{\text{high}} = \{0.51, 0.7, 0.9, 1.0, 1.02, 1.05, 1.1, 1.5, 1.9\}$.

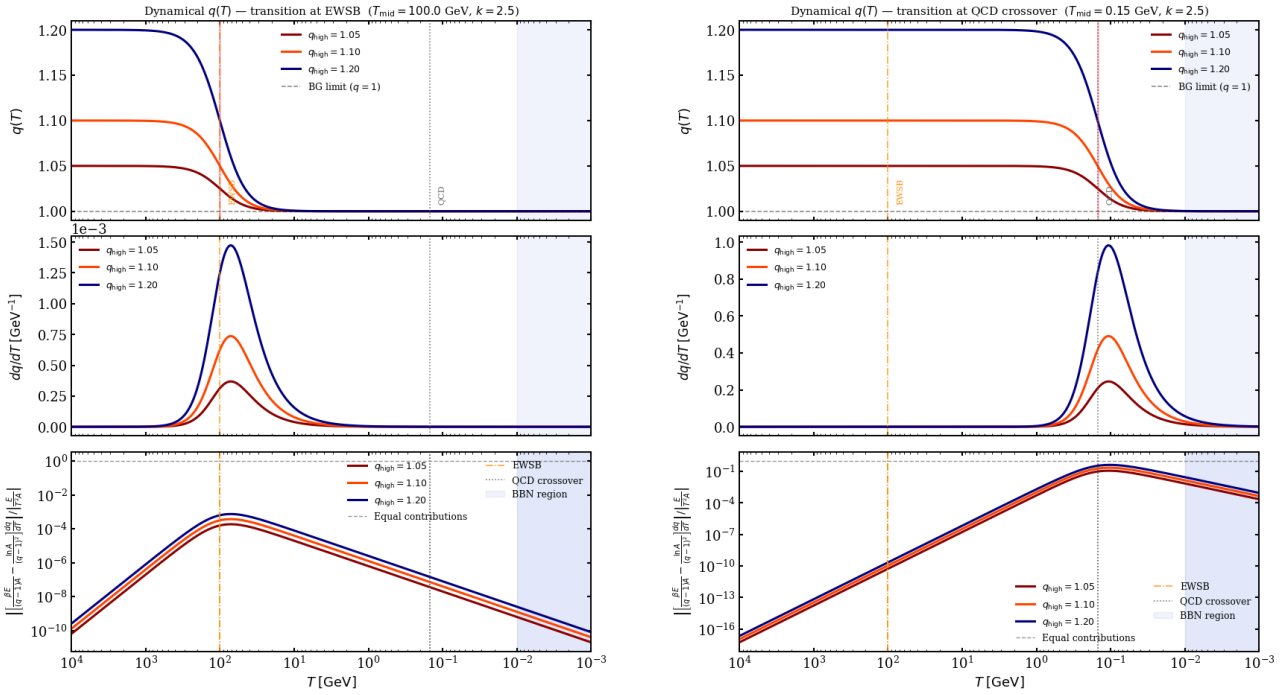

(a) EWSB scale ($T_{\rm mid} = 100$ GeV). (b) QCD scale ($T_{\rm mid} = 0.15$ GeV).

Figure 7.4: **Dynamical evolution of the Tsallis parameter and induced non-linearity by the sigmoid function.** Left: Electroweak Symmetry Breaking transition. Right: QCD crossover. In both cases, the lower panel shows the absolute ratio between the dynamical non-linear contribution and the standard fixed-q term from Eq. (7.15). The dynamical contribution peaks around $T_{\rm mid}$ and vanishes toward the BBN regime, recovering extensivity ($q \simeq 1$).

For fixed q, the term $dq(T)/dT$ vanishes and only the first contribution remains.

The sigmoid profile is particularly useful for this analysis because it introduces a transition scale $T_{\rm mid}$ and a sharpness parameter k. Therefore, the contribution proportional to dq/dT in Eq. (7.15) can be localized around physical crossover regions such as EWSB or QCD. In contrast, the logarithmic profile produces a smoother and more global evolution in temperature, without isolating a specific transition scale.

To illustrate the phenomenological behavior of this formulation, we evaluate the sigmoid relaxation at two critical epochs of the Early Universe characterized by rapid crossovers associated with changes in the effective degrees of freedom: the Electroweak Symmetry Breaking scale, EWSB, with $T_{\rm mid} \sim 100$ GeV, and the QCD crossover, with $T_{\rm mid} \sim 0.15$ GeV [1].

As shown in Figs. 7.4a and 7.4b, the dynamical framework introduces a localized enhancement in the thermodynamic non-linearity. The bottom panels display the absolute ratio between the extra dynamical non-linearity, the term proportional to dq/dT in Eq. (7.15), and the standard fixed-q thermal contribution. During the transition phase, $T \sim T_{\rm mid}$, the derivative dq/dT reaches its maximum amplitude, causing the dynamical contribution to become relevant. As the Universe expands and cools into the BBN region, $T \sim 10^{-4} - 10^{-2}$ GeV, dq/dT vanishes and the ratio drops to zero, allowing the Boltzmann-Gibbs regime to be recovered within the adopted approximation. This qualitative analysis suggests that a dynamical, temperature-dependent Tsallis parameter can provide a useful phenomenological description of the primordial plasma during epochs of rapid crossover. Within the sigmoid ansatz, the relaxation of $q(T)$ can be interpreted as producing localized pulses of enhanced thermodynamic non-linearity.

7.4 Thermodynamic consistency through the generalized H-Theorem

Promoting the Tsallis Parameter q to a temperature-dependent function $q(T)$ introduces a conceptual challenge that must be addressed with care. Recall that the generalized H-theorem establishes that the attractors of the dynamics are the q-generalized distribution functions obtained from the maximum entropy principle under the assumption of constant q [11, 23]. However, if q evolves due to the expansion of the Universe, the corresponding attractors also become time dependent, or equivalently temperature dependent.

To ensure thermodynamic consistency, a separation of timescales must be invoked:

- The microscopic relaxation time, governed by the interaction rate Γ, must be much shorter than the expansion timescale set by the Hubble parameter H [19]. Therefore, when $\Gamma \gg H$, the system rapidly relaxes toward a sequence of quasi-stationary states.
- An adiabatic evolution is assumed: at each instant, the plasma effectively experiences an approximately constant value of $q(T)$. The generalized H-theorem then supports the interpretation of relaxation toward an instantaneous attractor corresponding to that value of the Tsallis Parameter. This relaxation process continues until the extensive regime $q \simeq 1$ is reached.

Strictly speaking, the generalized H-theorem is formulated for fixed q. When q is promoted to $q(T)$, the entropy functional itself becomes slowly time dependent. Therefore, the present construction should be interpreted as a quasi-static approximation: at each temperature, the plasma is assumed to relax toward the instantaneous $q(T)$-equilibrium attractor. This requires a hierarchy of timescales,

$$\Gamma \gg H, \qquad \Gamma \gg \left| \frac{d \ln q}{dt} \right|,$$

so that microscopic relaxation is faster than both the Hubble expansion and the variation of the nonextensive parameter.[1]

This provides a basis for further development of the framework and for future applications to Early Universe cosmological scenarios.

[1] The generalized H-theorem is formulated for fixed q. Its use for $q(T)$ is therefore local in temperature: the plasma is assumed to relax toward an instantaneous $q(T)$-equilibrium attractor under a quasi-static separation of timescales.

Chapter 8

Conclusions and Future Work

Conclusions

The central motivation of this thesis was to study how a nonextensive primordial plasma could affect the thermal production of WIMP dark matter. In this context, this work formulated and compared two extensions of the standard Freeze-out framework within Tsallis statistics: a first order $(q-1)$ Taylor approximation and an exact treatment based on q-exponentials. The formalism propagates nonextensivity to the effective degrees of freedom $(g_{*,q}, g_{*s,q})$, the expansion rate $H_q(T)$, the effective q-generalized Boltzmann equation for $Y_{\chi,q}(x)$, and a q-logarithmic transcendental equation for x_f.

The comparison between both prescriptions shows that the first order approximation is useful as an analytical guide near the extensive limit, but it is not sufficiently reliable for the phenomenological analysis developed in this work. For this reason, the exact formulation provides the main framework for the numerical results. With the thermally averaged cross section approximated through a partial-wave expansion up to p-wave order,

$$\langle \sigma v \rangle_q \approx a + b \, \langle v_{\rm rel}^2 \rangle_q, \tag{8.1}$$

and with (a, b) treated as nuisance parameters, the Relic Abundance observable alone does not provide a robust constraint on q. This is because different combinations of q, m_χ, and the annihilation parameters can reproduce the observed dark matter abundance. Therefore, in this thesis, $\Omega_{\chi,q}h^2$ should be interpreted mainly as a consistency test of the nonextensive Freeze-out framework, rather than as a unique determination of the Tsallis parameter.

The parameter-space scans also show that underabundant regions, $\Omega_{\chi,q}h^2 < 0.12$, may be interpreted within a Multi-component dark matter scenario. This interpretation is not a necessary consequence of nonextensivity, but it provides a possible phenomenological extension when a single WIMP component does not saturate the observed abundance for fixed annihilation parameters. In this sense, the nonextensive framework can be used to explore how thermal relic production changes when the primordial plasma is deformed, while still remaining compatible with the possibility that dark matter is composed of more than one stable species.

Radiation era observables encoded in $\Delta N_{\rm eff}(q)$ provide a more direct phenomenological handle on the nonextensive parameter. Within the effective deformation of the neutrino sector adopted here, the comparison with BBN and CMB+BAO data restricts q to values close to the extensive limit, favoring a near-extensive background by the BBN epoch, or equivalently around $T \sim 1$ MeV. These bounds should be understood as phenomenological constraints within the assumptions of the present setup, since a full treatment of neutrino decoupling, spectral distortions, finite-temperature effects, weak interaction rates, and light-element abundances is not performed. Nevertheless, the result indicates that any nonextensive correction surviving into the late radiation era must be small.

Based on this restriction, a dynamical relaxation model $q(T)$ was introduced as a phenomenological way to reconcile possible nonextensive effects at earlier stages of the Early Universe with the near-extensive behavior required close to BBN. By assuming a separation of timescales, the primordial plasma can be modeled as evolving through quasi-stationary states. Under the stated assumptions, this allows a local use of the q-generalized H-Theorem. This dynamical description should not be interpreted as a microscopic derivation of $q(T)$, but rather as an effective parametrization of how a nonextensive imprint could relax as the Universe cools.

The dynamical evolution was modeled using simple profiles for $q(T)$, with particular emphasis on a sigmoid-type function evaluated qualitatively around phase-transition scales such as EWSB and the QCD crossover. In this case, the non-linearity of the thermal evolution receives an additional contribution proportional to dq/dT. This contribution is localized around the transition scale fixed by T_{mid} and becomes negligible before the BBN era within the parameter choices considered here. Therefore, the sigmoid ansatz provides a controlled way to localize possible nonextensive effects around physically motivated thermal transitions, while recovering an almost standard radiation background at lower temperatures.

Overall, the results suggest that Tsallis statistics can be used as a phenomenological framework to organize possible departures from Boltzmann-Gibbs thermodynamics in the primordial plasma. At the same time, the analysis shows that such departures are strongly limited by radiation era observables. The main outcome is therefore not evidence for a nonextensive primordial plasma, but a controlled route to identify where nonextensive effects may enter the WIMP Freeze-out calculation, where they are observationally constrained, and which assumptions must be improved in future work.

Future Work

As future work, several extensions follow naturally from the framework developed in this thesis:

- Generalize the exact thermally averaged cross section in Eq. (2.29), instead of using the partial-wave approximation, and implement it in the generalized Boltzmann equation for WIMP Freeze-out, Eq. (4.4).
- Explore heavier WIMP masses, especially $m_\chi \geq 1$ TeV, and study how the phenomenology changes for different values of q.
- Study direct and indirect detection observables within the Tsallis framework, including the effect of nonextensive corrections on the expected signals.
- Incorporate concrete particle-physics dark matter models into the exact nonextensive Freeze-out framework.
- Apply the formalism to the real singlet scalar dark matter model and assess whether Tsallis corrections modify its viable parameter space [36].
- Further develop the dynamical nonextensive parameter $q(T)$, clarifying its physical interpretation and its implementation in Early Universe cosmology.
- Study the Freeze-in production mechanism of dark matter within Tsallis statistics.

Appendix A

Mathematical Developments and Additional Formulas

This appendix collects the mathematical derivations and auxiliary formulas used in the main text. Sections A.3–A.4.1 support the discussion of Tsallis entropy and its constraint structure. Section A.5 gives the first order expressions used to compare the perturbative and exact descriptions. Section A.6.1 presents the exact mapping used to define the nonextensive rescalings, and Section A.6.2 gives the derivation of the q-generalized transcendental equation used for the Freeze-out point.

A.1 Number Density

The number density for a species with g internal degrees of freedom is computed from the integral of its equilibrium distribution function, see Eq. (2.12):

$$n \;=\; g \int \frac{d^3p}{(2\pi)^3}\, f(E)\,, \tag{A.1}$$

where, unless otherwise indicated, the chemical potential is taken to be negligible, $\mu \simeq 0$.

A.1.1 Relativistic case

For relativistic particles, $E \simeq p$, bosons and fermions are treated separately. For bosons:

$$\begin{aligned} n_b &= \frac{g_b}{(2\pi)^3} \int \frac{d^3p}{e^{p/T}-1} = \frac{g_b}{2\pi^2} \int_0^\infty \frac{p^2\,dp}{e^{p/T}-1} = \frac{g_b T^3}{2\pi^2} \int_0^\infty \frac{x^2\,dx}{e^{x}-1} \\ &= \frac{g_b T^3}{2\pi^2} \Big(2\,\zeta(3)\Big) \;=\; \frac{\zeta(3)}{\pi^2}\, g_b\, T^3\,. \end{aligned} \tag{A.2}$$

For fermions one uses the standard identity

$$\int_0^\infty \frac{x^2\,dx}{e^{x}+1} = \frac{3}{2}\zeta(3),$$

so that

$$n_f \;=\; \frac{3}{4}\,\frac{\zeta(3)}{\pi^2}\, g_f\, T^3\,. \tag{A.3}$$

A.1.2 Nonrelativistic case

In this regime it is more precise to work with $E = \sqrt{p^2 + m^2}$. The integral is expressed through K_2, the modified Bessel function of the second kind:

$$n \;=\; \frac{g\, m^2 T}{2\pi^2}\, K_2\!\left(\frac{m}{T}\right). \tag{A.4}$$

For $z \equiv m/T \gg 1$, one uses $K_\nu(z) \sim \sqrt{\pi/(2z)}\, e^{-z}$ and obtains the Maxwell-Boltzmann form with Boltzmann suppression:

$$n \;\simeq\; g\left(\frac{mT}{2\pi}\right)^{3/2} e^{-m/T}. \tag{A.5}$$

A.2 Energy Density

Analogously, the energy density is defined by

$$\rho \;=\; g \int \frac{d^3p}{(2\pi)^3}\, E(p)\, f(E)\,. \tag{A.6}$$

A.2.1 Relativistic case

For a relativistic bosonic species:

$$\begin{aligned}\rho_b &= \frac{g_b}{2\pi^2}\int_0^\infty \frac{p^3\, dp}{e^{p/T}-1} = \frac{g_b T^4}{2\pi^2}\int_0^\infty \frac{x^3\, dx}{e^x-1} = \frac{g_b T^4}{2\pi^2}\left(\frac{\pi^4}{15}\right)\\ &= \frac{\pi^2}{30}\, g_b\, T^4\,.\end{aligned} \tag{A.7}$$

For fermions one obtains

$$\rho_f \;=\; \frac{7}{8}\,\frac{\pi^2}{30}\, g_f\, T^4\,, \tag{A.8}$$

where the factor $7/8$ comes from the integral

$$\int_0^\infty \frac{x^3}{e^x+1}\, dx = \frac{7}{8}\,\frac{\pi^4}{15}.$$

A.2.2 Nonrelativistic case

In the nonrelativistic limit, the energy is dominated by the rest mass, so at leading order

$$\rho \;\simeq\; m\, n\,, \tag{A.9}$$

with n given by Eq. (A.4) or, for $m \gg T$, by Eq. (A.5). The subleading kinetic correction is $\frac{3}{2}nT$ for an ideal classical gas.

For the total relativistic content at a common temperature, it is useful to write

$$\rho = g_*\,\frac{\pi^2}{30} T^4,$$

with g_* defined in Eq. (2.19). Analogously, the entropy satisfies

$$s = g_{*s}\,\frac{2\pi^2}{45} T^3,$$

with g_{*s} given by Eq. (2.22).

A.3 Tsallis Entropy

The Tsallis entropy, S_q, can be obtained as a generalization of the Boltzmann-Gibbs-Shannon entropy by replacing the natural logarithm, ln, with its analogue in the nonextensive formalism, the q-logarithm, $\ln_q$ [23].

The fundamental form of entropy in standard statistical mechanics is

$$S = k \sum_i p_i \ln\left(\frac{1}{p_i}\right), \tag{A.10}$$

where $\{p_i\}$ is the set of probabilities of the system's microstates.

The generalization is achieved by introducing the q-logarithm:

$$\ln_q(x) \equiv \frac{x^{1-q} - 1}{1-q}. \tag{A.11}$$

In the limit $q \to 1$, one recovers the natural logarithm, $\ln_q(x) \to \ln(x)$.

Applying this replacement in the entropy formula, one obtains the form postulated by Tsallis in 1987 [8]:

$$S_q = k \sum_i p_i \ln_q\left(\frac{1}{p_i}\right). \tag{A.12}$$

Substituting the definition of the q-logarithm and expanding algebraically:

$$S_q = k \sum_i p_i \left(\frac{(1/p_i)^{1-q} - 1}{1-q}\right) \tag{A.13}$$

$$= k \sum_i \left(\frac{p_i \cdot p_i^{q-1} - p_i}{1-q}\right) = k \sum_i \left(\frac{p_i^q - p_i}{1-q}\right). \tag{A.14}$$

Separating the sum into two parts:

$$S_q = \frac{k}{1-q}\left(\sum_i p_i^q - \sum_i p_i\right). \tag{A.15}$$

Using the probability normalization condition, $\sum_i p_i = 1$, the expression simplifies to

$$S_q = \frac{k}{1-q}\left(\sum_i p_i^q - 1\right). \tag{A.16}$$

Finally, rearranging the expression gives the standard convention for the Tsallis entropy:

$$S_q = k\frac{1 - \sum_i p_i^q}{q-1}. \tag{A.17}$$

A.4 Non-additivity of Tsallis Entropy

A fundamental property distinguishing the Tsallis entropy, S_q, from the Boltzmann-Gibbs entropy, S_{BG}, is its non-additivity. While S_{BG} is strictly additive for independent systems, S_q obeys a more general composition rule known as *pseudo-additivity*. For a system composed of two statistically independent subsystems, A and B, the total entropy is expressed as [23]

$$S_q(A+B) = S_q(A) + S_q(B) + (1-q)S_q(A)S_q(B). \tag{A.18}$$

The term $(1-q)S_q(A)S_q(B)$ quantifies the deviation from additivity. Depending on the value of the parameter q, three regimes are defined:

Extensive ($q = 1$): The interaction term vanishes and the additivity of Boltzmann-Gibbs entropy is recovered: $S_1(A + B) = S_1(A) + S_1(B)$.

Super-additive ($q < 1$): The interaction term is positive, yielding $S_q(A+B) > S_q(A)+S_q(B)$.

Sub-additive ($q > 1$): The interaction term is negative, leading to $S_q(A+B) < S_q(A)+S_q(B)$.

Proof. Let A be a discrete system with probabilities $\{p_i\}$ and B another discrete system with probabilities $\{r_j\}$. The Tsallis entropy, with $k_B = 1$, is defined as

$$S_q(P) = \frac{1 - \sum_i p_i^q}{q - 1}, \qquad q \in \mathbb{R}, \quad q \neq 1.$$

If A and B are independent, the combined system $A + B$ has probabilities $p_{ij} = p_i r_j$. Then

$$S_q(A + B) = \frac{1 - \sum_{i,j}(p_{ij})^q}{q - 1} = \frac{1 - \sum_{i,j}(p_i r_j)^q}{q - 1} = \frac{1 - \left(\sum_i p_i^q\right)\left(\sum_j r_j^q\right)}{q - 1}.$$

Define $X = \sum_i p_i^q$ and $Y = \sum_j r_j^q$. Then

$$S_q(A + B) = \frac{1 - XY}{q - 1}, \qquad S_q(A) = \frac{1 - X}{q - 1}, \qquad S_q(B) = \frac{1 - Y}{q - 1}.$$

Now consider

$$S_q(A) + S_q(B) + (1 - q)S_q(A)S_q(B) = \frac{1 - X}{q - 1} + \frac{1 - Y}{q - 1} + (1 - q)\frac{(1 - X)(1 - Y)}{(q - 1)^2}.$$

Since

$$\frac{1 - q}{(q - 1)^2} = -\frac{1}{q - 1},$$

one obtains

$$\begin{aligned} \text{Right-hand side} &= \frac{2 - X - Y}{q - 1} - \frac{(1 - X)(1 - Y)}{q - 1} \\ &= \frac{2 - X - Y - (1 - X - Y + XY)}{q - 1} = \frac{1 - XY}{q - 1} = S_q(A + B). \end{aligned}$$

This gives the pseudo-additive composition rule of the Tsallis entropy, also related to the q-sum structure [35].

A.4.1 Constraints for the Maximization of Entropy

The common probability normalization condition for all constraint prescriptions is

$$\sum_i p_i = 1. \tag{A.19}$$

Constraint I (linear / ordinary average) [23]:

$$\langle A \rangle = \sum_i p_i A_i, \qquad \overline{E} \equiv \langle E \rangle = \sum_i p_i E_i. \tag{A.20}$$

Constraint II (Curado–Tsallis, unnormalized q-average) [24]:

$$\langle A \rangle_q^{\mathrm{CT}} = \sum_i p_i^q A_i, \qquad \overline{E}_q^{\mathrm{CT}} = \sum_i p_i^q E_i. \tag{A.21}$$

Constraint III (Tsallis–Mendes–Plastino, normalized q-average) [37]:

$$P_i^{(q)} \equiv \frac{p_i^q}{\sum_j p_j^q}, \qquad \langle A \rangle_q^{\mathrm{TMP}} = \sum_i P_i^{(q)} A_i, \qquad \overline{E}_q^{\mathrm{TMP}} = \sum_i P_i^{(q)} E_i. \tag{A.22}$$

A.5 Analytic Expressions of Cosmological Observables in Nonextensive Statistics at First Order

In this appendix we show the first-order calculations in $(q-1)$ for the cosmological observables used in the main text. We start from the standard definitions in Eqs. (2.13)–(2.15) and from the first-order approximation of the q-generalized distribution function given in Eq. (3.16). Unless otherwise indicated, we take $\mu = 0$.

A.5.1 Generalized Distribution at First Order and Structure of the Integrals

Let $f_0(E)$ be the standard equilibrium distribution in Eq. (2.12). To first order in $(q-1)$,

$$f_q(E) = f_0(E)\Big[1 + (q-1)\Phi(E/T,\xi)\Big] + \mathcal{O}\Big((q-1)^2\Big), \tag{A.23}$$

where Φ is a dimensionless function depending on E/T and on the statistics ξ, as given in Eq. (3.16). With Eq. (A.23), any observable linear in f adopts the scheme

$$\mathcal{O}_q = \mathcal{O}_{\rm std} + (q-1)\delta\mathcal{O} + \mathcal{O}\Big((q-1)^2\Big), \tag{A.24}$$

with

$$\mathcal{O}_{\rm std} = g\int \frac{d^3p}{(2\pi)^3}\, W(p) f_0(E), \qquad \delta\mathcal{O} = g\int \frac{d^3p}{(2\pi)^3}\, W(p) f_0(E)\Phi(E/T,\xi), \tag{A.25}$$

where $W(p)$ is the appropriate kinematic weight: 1 for n, E for ρ, and $p^2/(3E)$ for P. The standard integrals over $x = p/T$ produce combinations of ζ-functions and powers of π; the numerical coefficients cited below are taken from [26].

A.5.2 Number Density

Inserting Eq. (A.23) into Eq. (2.13) and using $x = p/T$:

$$n_q = g\int \frac{d^3p}{(2\pi)^3} f_q = \frac{gT^3}{2\pi^2}\int_0^\infty dx\, x^2\Big[f_0(x) + (q-1) f_0(x)\Phi(x,\xi)\Big]. \tag{A.26}$$

Evaluating the integrals, with coefficients from [26], gives

$$n_q = \begin{cases} \dfrac{\zeta(3)}{\pi^2} gT^3 + \dfrac{g(q-1)}{2\pi^2}\Big(12.98\Big)T^3, & \text{bosons (Bose-Einstein)},\ \xi = -1, \\ \dfrac{3}{4}\dfrac{\zeta(3)}{\pi^2} gT^3 + \dfrac{g(q-1)}{2\pi^2}\Big(11.36\Big)T^3, & \text{fermions (Fermi-Dirac)},\ \xi = +1, \\ \dfrac{gm^2T}{2\pi^2} K_2\Big(\dfrac{m}{T}\Big)\left[1 + \dfrac{q-1}{2}\left(\dfrac{15}{4} + \dfrac{3m}{T} + \dfrac{m^2}{T^2}\right)\right], & \text{Maxwell-Boltzmann},\ \xi = 0. \end{cases} \tag{A.27}$$

For $m/T \gg 1$, one may use $K_2(z) \sim \sqrt{\pi/(2z)}e^{-z}$ to obtain the Maxwell-Boltzmann asymptotic form.

A.5.3 Energy Density and Pressure

With Eqs. (2.14) and (A.23),

$$\rho_q = \frac{gT^4}{2\pi^2}\int_0^\infty dx\, x^2 \frac{E}{T}\Big[f_0(x) + (q-1)f_0(x)\Phi(x,\xi)\Big], \tag{A.28}$$

and analogously for P_q with weight $W = p^2/(3E)$. In the relativistic regime, $E \simeq p$, one obtains

$$\rho_q = \begin{cases} \dfrac{\pi^2}{30} g T^4 + \dfrac{30}{\pi^2}(1.04) g (q-1) T^4, & \text{bosons, } \xi = -1, \\ \dfrac{7}{8}\dfrac{\pi^2}{30} g T^4 + \dfrac{30}{\pi^2}(0.97) g (q-1) T^4, & \text{fermions, } \xi = +1, \\ m n_q, & \text{Maxwell-Boltzmann, } \xi = 0. \end{cases} \tag{A.29}$$

In the last line, $E \simeq m$ has been used at leading order in the nonrelativistic regime. For the total relativistic content at a common temperature, it is useful to write

$$g_{*q} = \sum_{\text{bosons}} g_i \left(\frac{T_i}{T}\right)^4 + \frac{7}{8}\sum_{\text{fermions}} g_j \left(\frac{T_j}{T}\right)^4 + (q-1)\left[9.58 \sum_{\text{bosons}} g_i \left(\frac{T_i}{T}\right)^4 + 8.98 \sum_{\text{fermions}} g_j \left(\frac{T_j}{T}\right)^4\right], \tag{A.30}$$

so that

$$\rho_q = \frac{\pi^2}{30} g_{*q} T^4, \qquad P_q \simeq \frac{1}{3}\rho_q \quad \text{(relativistic regime)}. \tag{A.31}$$

A.5.4 Entropy Density and Entropic Degrees of Freedom

Using $s_q = (\rho_q + P_q)/T$ and $P_q \simeq \rho_q/3$ in the relativistic regime, one obtains

$$s_q = \frac{2\pi^2}{45} g_{*s,q} T^3, \tag{A.32}$$

with

$$g_{*s,q} = \sum_{\text{bosons}} g_i \left(\frac{T_i}{T}\right)^3 + \frac{7}{8}\sum_{\text{fermions}} g_j \left(\frac{T_j}{T}\right)^3 + 7.18(q-1)\left[\sum_{\text{bosons}} g_i \left(\frac{T_i}{T}\right)^3 + \frac{15}{16}\sum_{\text{fermions}} g_j \left(\frac{T_j}{T}\right)^3\right], \tag{A.33}$$

as used in the main body; see Eqs. (2.21) and (2.22) for the standard case. The comoving entropy $S_q = s_q a^3$ remains approximately constant in adiabatic expansion.

A.5.5 Velocity Moments and Thermally Averaged Cross Section

For the computation of

$$\langle \sigma v \rangle_q \approx a + b\, \langle v_{\text{rel}}^2 \rangle_q,$$

the relative velocity moment $\langle v_{\text{rel}}^2 \rangle_q = 2\langle v^2 \rangle_q$ is required. In the notation used in the text, with $x \equiv m_\chi/T$ and $y \equiv p/T$:

$$\langle v^2 \rangle_q = \frac{\displaystyle\int_0^{y_{\max}} dy\, y^2 \left(\frac{y}{\sqrt{y^2+x^2}}\right)^2 f_q\!\left(\sqrt{y^2+x^2}\right)}{\displaystyle\int_0^{y_{\max}} dy\, y^2 f_q\!\left(\sqrt{y^2+x^2}\right)}. \tag{A.34}$$

Here f_q is expanded as in Eq. (A.23). To first order in $(q-1)$:

$$\langle v^2\rangle_q = \langle v^2\rangle_{\rm std} + (q-1)\delta\Big(\langle v^2\rangle\Big)\,, \tag{A.35}$$

where the correction is given by ratios of integrals weighted by Φ. This scheme is replicated for any kinematic moment required in the partial-wave expansion and is used in the comparison between the perturbative and exact models in the results chapter.

A.5.6 Equilibrium Abundance and Comoving Variables

The comoving abundance is defined as $Y_q \equiv n_q/s_q$. In equilibrium:

$$Y_q^{\rm eq}(T) = \frac{n_q^{\rm eq}(T)}{s_q(T)} = \frac{n_{\rm std}^{\rm eq}(T) + (q-1)\delta n^{\rm eq}(T)}{s_{\rm std}(T) + (q-1)\delta s(T)} = Y_{\rm std}^{\rm eq}(T)\left[1 + (q-1)\Delta_Y(T)\right], \tag{A.36}$$

where Δ_Y is a linear combination of $\delta n^{\rm eq}/n_{\rm std}^{\rm eq}$ and $\delta s/s_{\rm std}$. This form is inserted into the q-generalized Boltzmann equation in the main chapter to study Freeze-out.

The previous results specify how corrections of order $(q-1)$ enter n_q, ρ_q, s_q, g_{*q}, $g_{*s,q}$, and H_q.

A.6 Expressions of Cosmological Observables in Nonextensive Statistics in Exact Form

In this section of the appendix we present the construction of the exact model. The model is based on ratios of phase-space integrals, which are evaluated numerically in the main analysis.

A.6.1 Factorization of Generalized Observables and Development of the Mapping

We use the notation

$$x \equiv \frac{m}{T}, \qquad y \equiv \frac{p}{T}, \qquad z \equiv \frac{E}{T} = \sqrt{y^2 + x^2}, \qquad \mu = 0,$$

and the exact Tsallis distribution for Maxwell-Boltzmann statistics:

$$e_q(-z) = \begin{cases} \Big[1 - (1-q)z\Big]^{\frac{1}{1-q}}, & \text{if } 1-(1-q)z > 0, \\ 0, & \text{otherwise.} \end{cases}$$

The momentum-space measure is $d^3p = 4\pi p^2 dp = 4\pi T^3 y^2 dy$. For $q < 1$, the compact support fixes

$$y_{\rm max}(x,q) = \sqrt{\left(\frac{1}{1-q}\right)^2 - x^2}, \quad q < 1, \qquad y_{\rm max} = \infty, \quad q \geq 1. \tag{A.37}$$

When useful, we denote by "std" the case $q = 1$.

For a species with degeneracy g and Maxwell-Boltzmann statistics:

$$n_q(T) = \frac{g}{(2\pi)^3}\int d^3p\, e_q\Big(-\frac{E}{T}\Big) = \frac{g}{2\pi^2}T^3 \underbrace{\int_0^{y_{\max}} y^2 e_q\Big(-\sqrt{y^2+x^2}\Big)\, dy}_{I_n(x,q)}, \tag{A.38}$$

$$\rho_q(T) = \frac{g}{(2\pi)^3}\int d^3p\, E\, e_q\Big(-\frac{E}{T}\Big) = \frac{g}{2\pi^2}T^4 \underbrace{\int_0^{y_{\max}} y^2\sqrt{y^2+x^2}\, e_q\Big(-\sqrt{y^2+x^2}\Big)\, dy}_{I_\rho(x,q)}, \tag{A.39}$$

$$P_q(T) = \frac{g}{(2\pi)^3}\int d^3p\, \frac{p^2}{3E}\, e_q\Big(-\frac{E}{T}\Big) = \frac{g}{2\pi^2}T^4 \underbrace{\int_0^{y_{\max}} \frac{y^4}{3\sqrt{y^2+x^2}}\, e_q\Big(-\sqrt{y^2+x^2}\Big)\, dy}_{I_P(x,q)}. \tag{A.40}$$

The standard integrals are obtained by replacing $e_q \to e^{-z}$ and $y_{\max} \to \infty$:

$$I_n^{\rm std}(x) = \int_0^\infty y^2 e^{-\sqrt{y^2+x^2}} dy, \qquad I_\rho^{\rm std}(x) = \int_0^\infty y^2\sqrt{y^2+x^2}\, e^{-\sqrt{y^2+x^2}} dy, \tag{A.41}$$

$$I_P^{\rm std}(x) = \int_0^\infty \frac{y^4}{3\sqrt{y^2+x^2}}\, e^{-\sqrt{y^2+x^2}} dy. \tag{A.42}$$

For $q > 1$, convergence must be checked because the exact q-exponential develops power-law tails. For $q < 1$, the compact support guarantees convergence with $y_{\max}$ given by Eq. (A.37).

We define exact factors depending on x and q by ratios of integrals:

$$R_n(x,q) \equiv \frac{I_n(x,q)}{I_n^{\rm std}(x)}, \qquad R_\rho(x,q) \equiv \frac{I_\rho(x,q)}{I_\rho^{\rm std}(x)}, \qquad R_P(x,q) \equiv \frac{I_P(x,q)}{I_P^{\rm std}(x)}. \tag{A.43}$$

Then the physical densities are factorized as identities:

$$n_q = R_n(x,q) n_{\rm std}, \qquad \rho_q = R_\rho(x,q)\rho_{\rm std}, \qquad P_q = R_P(x,q) P_{\rm std}. \tag{A.44}$$

For the ultra-relativistic regime, $x \to 0$ and $z = \sqrt{y^2+x^2} \to y$. Changing variables to z:

$$I_n(0,q) = \int_0^{z_{\max}} z^2 e_q(-z)\, dz, \qquad I_\rho(0,q) = \int_0^{z_{\max}} z^3 e_q(-z)\, dz, \qquad I_P(0,q) = \frac{1}{3}\int_0^{z_{\max}} z^3 e_q(-z)\, dz.$$

In the standard case,

$$I_n^{\rm std}(0) = \Gamma(3) = 2!, \qquad I_\rho^{\rm std}(0) = \Gamma(4) = 3! = 6, \qquad I_P^{\rm std}(0) = \frac{1}{3}\Gamma(4) = 2.$$

Hence

$$R_n^{\rm UR}(q) = \frac{1}{2}\int_0^{z_{\max}} z^2 e_q(-z)\, dz, \qquad R_\rho^{\rm UR}(q) = \frac{1}{6}\int_0^{z_{\max}} z^3 e_q(-z)\, dz, \qquad R_P^{\rm UR}(q) = R_\rho^{\rm UR}(q). \tag{A.45}$$

In the ultra-relativistic regime one has $P_q = \rho_q/3$ and, with $\mu = 0$,

$$s_q = \frac{\rho_q + P_q}{T} = \frac{4}{3}\frac{\rho_q}{T} \quad \Longrightarrow \quad s_q = R_\rho^{\rm UR}(q) s_{\rm std}. \tag{A.46}$$

In summary, n_q and $R_n(q)$ converge in the ultra-relativistic limit if $q < 4/3$, while ρ_q, P_q, and $R_\rho(q)$ converge if $q < 5/4$.

In the ultra-relativistic regime with vanishing chemical potential, the species-aware rescaling factors for the number density and the energy density are defined as follows:

$$\exp_q(z) \equiv \Big[1 + (1-q)z\Big]^{\frac{1}{1-q}}, \qquad f_{q,\xi}(z) \equiv \frac{1}{\exp_q(z) + \xi}, \qquad \xi = \begin{cases} -1, & \text{BE}, \\ +1, & \text{FD}. \end{cases} \tag{A.47}$$

with

$$z_{\max} = \begin{cases} \dfrac{1}{1-q}, & q < 1, \\ \infty, & q \geq 1. \end{cases} \tag{A.48}$$

The species-aware rescalings are

$$R_n^{(\xi)}(q) = \frac{\displaystyle\int_0^{z_{\max}} \frac{z^2\,dz}{e_q(z) + \xi}}{\displaystyle\int_0^{\infty} \frac{z^2\,dz}{e^z + \xi}}, \qquad R_\rho^{(\xi)}(q) = \frac{\displaystyle\int_0^{z_{\max}} \frac{z^3\,dz}{e_q(z) + \xi}}{\displaystyle\int_0^{\infty} \frac{z^3\,dz}{e^z + \xi}}. \tag{A.49}$$

Explicitly,

$$R_n^{\text{BE}}(q) = \frac{\displaystyle\int_0^{z_{\max}} \frac{z^2\,dz}{e_q(z) - 1}}{\displaystyle\int_0^{\infty} \frac{z^2\,dz}{e^z - 1}}, \qquad R_n^{\text{FD}}(q) = \frac{\displaystyle\int_0^{z_{\max}} \frac{z^2\,dz}{e_q(z) + 1}}{\displaystyle\int_0^{\infty} \frac{z^2\,dz}{e^z + 1}}, \tag{A.50}$$

$$R_\rho^{\text{BE}}(q) = \frac{\displaystyle\int_0^{z_{\max}} \frac{z^3\,dz}{e_q(z) - 1}}{\displaystyle\int_0^{\infty} \frac{z^3\,dz}{e^z - 1}}, \qquad R_\rho^{\text{FD}}(q) = \frac{\displaystyle\int_0^{z_{\max}} \frac{z^3\,dz}{e_q(z) + 1}}{\displaystyle\int_0^{\infty} \frac{z^3\,dz}{e^z + 1}}. \tag{A.51}$$

These definitions reduce to the standard Bose-Einstein and Fermi-Dirac factors in the limit $q \to 1$ and are used in the bounds calculation for q using BBN and CMB+BAO data.

A.6.2 Generalized Transcendental Equation

We start from

$$\Gamma_{\text{ann},q}(T_f) \simeq H_q(T_f), \qquad \Gamma_{\text{ann},q} = n_{\chi,\text{eq},q}\Big|_{T_f} \langle \sigma v \rangle_q(T_f), \qquad x \equiv \frac{m_\chi}{T}, \quad x_f = \frac{m_\chi}{T_f}. \tag{A.52}$$

Chemical decoupling occurs in the nonrelativistic regime, $x_f \gtrsim \mathcal{O}(20)$, so we do not apply R_n to the WIMP particle sector. Instead, $n_{\chi,\text{eq},q}$ is computed from the exact phase-space integral in Eq. (3.29), evaluated in the nonrelativistic regime, $\langle v^2 \rangle_q$ is computed from Eq. (4.13), and the background enters through $H_q = \sqrt{R_\rho(q)}H$ with $R_\rho(q)$ defined above. With these inputs, the Freeze-out condition $\Gamma_{\text{ann},q}(T_f) \simeq H_q(T_f)$ leads to the q-logarithmic transcendental equation used in the main text:

$$x_f(q) \simeq \ln_q\left[\frac{g_\chi M_{\text{Pl}} m_\chi}{1.66(2\pi)^{3/2}\sqrt{g_*(T_f)R_\rho(q)}}\left(a + b\,\langle v_{\text{rel}}^2 \rangle_q\right)\sqrt{x_f}\right]. \tag{A.53}$$

This is the nonrelativistic-consistent form employed in the computations.

Appendix B

Methodological Inputs

This appendix records the numerical and statistical inputs used to generate the figures and tables discussed in the main text. The physical interpretation of these inputs is given in the corresponding chapters; here we only document the implementation details needed for reproducibility.

B.1 Degrees of Freedom and Nonextensive Deformation

We employ the effective energy and entropy degrees of freedom, defined by

$$\rho(T) = \frac{\pi^2}{30}\, g_*(T)\, T^4, \tag{B.1}$$

$$s(T) = \frac{2\pi^2}{45}\, g_{*s}(T)\, T^3. \tag{B.2}$$

To capture the Standard Model thermal thresholds, tables are built piecewise on a node mesh $\{T_i\}$ in increasing order, including m_e, neutrino decoupling, m_μ, pions, the QCD crossover, heavy quarks, and the electroweak sector. In each interval $[T_i, T_{i+1})$ one sets

$$g_*(T) = g_{*,i}, \qquad g_{*s}(T) = g_{*s,i}, \tag{B.3}$$

implementing a right-continuous step function.

When introducing the nonextensive deformation, g_* and g_{*s} are rescaled by a factor $R_\rho(q)$ constant in T:

$$R_\rho(q) = \frac{\displaystyle\int_0^{y_{\max}} y^3 e_q(-y)\, dy}{6}, \qquad y_{\max} = \begin{cases} \dfrac{1}{1-q}, & q < 1, \\ \infty, & q \geq 1, \end{cases} \tag{B.4}$$

leading to

$$\rho_q(T) = R_\rho(q)\rho_{\text{std}}(T), \qquad g_{*,q}(T) = R_\rho(q) g_*(T), \qquad g_{*s,q}(T) = R_\rho(q) g_{*s}(T). \tag{B.5}$$

For plotting, a logarithmic mesh in T is generated and the steps are smoothed by sigmoids centered on each threshold. Without this smoothing, the same input remains a stepped function. The smoothed curve is written as

$$g_{\text{smooth}}(T) = g_0 + \sum_i \Delta_i \frac{1 + \tanh\left(\frac{\log_{10} T - \log_{10} T_i}{w}\right)}{2}, \qquad \Delta_i = g_i - g_{i-1}, \tag{B.6}$$

where w controls the slope. The curves shown in the main text correspond to $g_{*,q}(T)$ and $g_{*s,q}(T)$ for different values of q as the Universe cools. The degrees of freedom are listed in Tables B.1 and B.2 [1].

Table B.1: Effective energy degrees of freedom $g_*(T)$ in the plasma.

Epoch	Range T [GeV]	$g_*(T)$
$\gamma + \nu\,(T \ll m_e)$	$[1.0 \times 10^{-6},\ 5.11 \times 10^{-4})$	3.363
m_e	$[5.11 \times 10^{-4},\ 8.0 \times 10^{-4})$	6.863
ν decoupling (approx.)	$[8.0 \times 10^{-4},\ 0.1057)$	10.75
m_μ	[0.1057, 0.135)	10.75
π^0	[0.135, 0.1396)	14.25
$\pi^\pm$	[0.1396, 0.170)	15.25
QCD crossover	[0.170, 1.29)	61.75
m_c	[1.29, 1.777)	72.25
m_τ	[1.777, 4.19)	75.75
m_b	[4.19, 80.4)	86.25
m_W	[80.4, 91.2)	92.25
m_Z	[91.2, 125.6)	95.25
m_H	[125.6, 173.3)	96.25
m_t	$[173.3,\ 1.0 \times 10^4]$	106.75

Table B.2: Entropic degrees of freedom $g_{*s}(T)$ in the plasma.

Epoch	Range T [GeV]	$g_{*s}(T)$
$\gamma + \nu\,(T \ll m_e)$	$[1.0 \times 10^{-6},\ 5.11 \times 10^{-4})$	3.909
m_e	$[5.11 \times 10^{-4},\ 8.0 \times 10^{-4})$	7.409
ν decoupling (approx.)	$[8.0 \times 10^{-4},\ 0.1057)$	10.75
m_μ	[0.1057, 0.135)	10.75
π^0	[0.135, 0.1396)	14.25
$\pi^\pm$	[0.1396, 0.170)	15.25
QCD crossover	[0.170, 1.29)	61.75
m_c	[1.29, 1.777)	72.25
m_τ	[1.777, 4.19)	75.75
m_b	[4.19, 80.4)	86.25
m_W	[80.4, 91.2)	92.25
m_Z	[91.2, 125.6)	95.25
m_H	[125.6, 173.3)	96.25
m_t	$[173.3,\ 1.0 \times 10^4]$	106.75

B.2 Effective Number of Neutrinos and Likelihoods

The statistical interpretation of this fit is discussed in the results chapter. Here we record only the explicit likelihood used in the numerical implementation. The model prediction is compared with the BBN and CMB+BAO observational inputs listed in Table 5.1 through

$$\chi^2_{N_{\rm eff}}(q) = \frac{\left[\widehat{N}_{\rm eff}(q) - \mu_{\rm BBN}\right]^2}{\sigma^2_{\rm BBN}} + \frac{\left[\widehat{N}_{\rm eff}(q) - \mu_{\rm CMB}\right]^2}{\sigma^2_{\rm CMB}}, \tag{B.7}$$

where μ denotes the central value and σ the corresponding observational uncertainty. The theoretical value $N_{\rm eff}^{\rm std}$ is not included as an additional datum in the χ^2; it is used only as the reference value around which the nonextensive shift is defined. Including it as an independent observational contribution would amount to double-counting the theoretical baseline and would artificially drive the fit toward $q = 1$.

It is also useful to define

$$\Delta\chi^2_{N_{\rm eff}}(q) = \chi^2_{N_{\rm eff}}(q) - \chi^2_{N_{\rm eff},\min}, \tag{B.8}$$

where $\chi^2_{N_{\rm eff},\rm min}$ is the minimum value of Eq. (B.7). This shift places the minimum at zero and allows the confidence intervals in q to be read from the standard $\Delta\chi^2$ thresholds, as shown in Fig. 6.14b.

Bibliography

[1] Lars Husdal. On effective degrees of freedom in the early universe. *Galaxies*, 4(4):78, December 2016.

[2] Vera C. Rubin and Jr. Ford, W. Kent. Rotation of the Andromeda Nebula from a Spectroscopic Survey of Emission Regions. *Astrophys. J.*, 159:379, 1970.

[3] Douglas Clowe et al. A Direct Empirical Proof of the Existence of Dark Matter. *Astrophys. J. Lett.*, 648:L109–L113, 2006.

[4] Planck Collaboration and N. et al. Aghanim. Planck 2018 results. vi. cosmological parameters. *Astron. Astrophys.*, 641:A6, 2020.

[5] Anthony Zee. *Group Theory in a Nutshell for Physicists*. Princeton University Press, 2016.

[6] Alexandre D. Dolgov Cosimo Bambi. *Introduction to Particle Cosmology*. Springer Berlin, Heidelberg, Springer-Verlag GmbH Germany, part of Springer Nature 2016, 1st edition, 2016.

[7] Dmitry S. Gorbunov and Valery A. Rubakov. *Introduction to the Theory of the Early Universe: Hot Big Bang Theory*. World Scientific, 2011.

[8] Constantino Tsallis. Possible Generalization of Boltzmann-Gibbs Statistics. *J. Statist. Phys.*, 52:479–487, 1988.

[9] Paolo Gondolo and Graciela Gelmini. Cosmic abundances of stable particles: Improved analysis. *Nucl. Phys. B*, 360:145–179, 1991.

[10] Richard H. Cyburt, Brian D. Fields, Keith A. Olive, and Tsung-Han Yeh. Big bang nucleosynthesis: Present status. *Rev. Mod. Phys.*, 88:015004, 2016. See constraint $N_\nu = 2.88 \pm 0.16$.

[11] J. A. S. Lima, R. Silva, and A. R. Plastino. Nonextensive thermostatistics and the H theorem. *Phys. Rev. Lett.*, 86:2938–2941, 2001.

[12] Mayumi Aoki, Michael Duerr, Jisuke Kubo, and Hiroshi Takano. Multi-Component Dark Matter Systems and Their Observation Prospects. *Phys. Rev. D*, 86:076015, 2012.

[13] Julien Froustey, Cyril Pitrou, and Maria Cristina Volpe. Neutrino decoupling including flavour oscillations and primordial nucleosynthesis. *JCAP*, 12:015, 2020.

[14] G. Belanger, F. Boudjema, and A. Pukhov. micromegas : a code for the calculation of dark matter properties in generic models of particle interaction, 2014.

[15] Pedro G. Ferreira and Alexander Roskill. A Short Introduction to Cosmology and its Current Status. 9 2025.

[16] S. Perlmutter, G. Aldering, G. Goldhaber, R. A. Knop, P. Nugent, P. G. Castro, S. Deustua, S. Fabbro, A. Goobar, D. E. Groom, I. M. Hook, A. G. Kim, M. Y. Kim, J. C. Lee, N. J. Nunes, R. Pain, C. R. Pennypacker, R. Quimby, C. Lidman, R. S. Ellis, M. Irwin, R. G. McMahon, P. Ruiz-Lapuente, N. Walton, B. Schaefer, B. J. Boyle, A. V. Filippenko, T. Matheson, A. S. Fruchter, N. Panagia, H. J. M. Newberg, W. J. Couch, and The Supernova Cosmology Project. Measurements of Ω and Λ from 42 high-redshift supernovae. *The Astrophysical Journal*, 517(2):565–586, June 1999.

[17] A.G. Adame, J. Aguilar, S. Ahlen, S. Alam, D.M. Alexander, M. Alvarez, O. Alves, A. Anand, U. Andrade, E. Armengaud, S. Avila, A. Aviles, H. Awan, B. Bahr-Kalus, S. Bailey, C. Baltay, A. Bault, J. Behera, S. BenZvi, A. Bera, F. Beutler, D. Bianchi, C. Blake, R. Blum, S. Brieden, A. Brodzeller, D. Brooks, E. Buckley-Geer, E. Burtin, R. Calderon, R. Canning, A. Carnero Rosell, R. Cereskaite, J.L. Cervantes-Cota, S. Chabanier, E. Chaussidon, J. Chaves-Montero, S. Chen, X. Chen, T. Claybaugh, S. Cole, A. Cuceu, T.M. Davis, K. Dawson, A. de la Macorra, A. de Mattia, N. Deiosso, A. Dey, B. Dey, Z. Ding, P. Doel, J. Edelstein, S. Eftekharzadeh, D.J. Eisenstein, A. Elliott, P. Fagrelius, K. Fanning, S. Ferraro, J. Ereza, N. Findlay, B. Flaugher, A. Font-Ribera, D. Forero-Sánchez, J.E. Forero-Romero, C.S. Frenk, C. Garcia-Quintero, E. Gaztañaga, H. Gil-Marín, S.Gontcho A. Gontcho, A.X. Gonzalez-Morales, V. Gonzalez-Perez, C. Gordon, D. Green, D. Gruen, R. Gsponer, G. Gutierrez, J. Guy, B. Hadzhiyska, C. Hahn, M.M.S. Hanif, H.K. Herrera-Alcantar, K. Honscheid, C. Howlett, D. Huterer, V. Iršič, M. Ishak, S. Juneau, N.G. Karaçaylı, R. Kehoe, S. Kent, D. Kirkby, A. Kremin, A. Krolewski, Y. Lai, T.-W. Lan, M. Landriau, D. Lang, J. Lasker, J.M. Le Goff, L. Le Guillou, A. Leauthaud, M.E. Levi, T.S. Li, E. Linder, K. Lodha, C. Magneville, M. Manera, D. Margala, P. Martini, M. Maus, P. McDonald, L. Medina-Varela, A. Meisner, J. Mena-Fernández, R. Miquel, J. Moon, S. Moore, J. Moustakas, E. Mueller, A. Muñoz-Gutiérrez, A.D. Myers, S. Nadathur, L. Napolitano, R. Neveux, J.A. Newman, N.M. Nguyen, J. Nie, G. Niz, H.E. Noriega, N. Padmanabhan, E. Paillas, N. Palanque-Delabrouille, J. Pan, S. Penmetsa, W.J. Percival, M.M. Pieri, M. Pinon, C. Poppett, A. Porredon, F. Prada, A. Pérez-Fernández, I. Pérez-Ràfols, D. Rabinowitz, A. Raichoor, C. Ramírez-Pérez, S. Ramirez-Solano, M. Rashkovetskyi, C. Ravoux, M. Rezaie, J. Rich, A. Rocher, C. Rockosi, N.A. Roe, A. Rosado-Marin, A.J. Ross, G. Rossi, R. Ruggeri, V. Ruhlmann-Kleider, L. Samushia, E. Sanchez, C. Saulder, E.F. Schlafly, D. Schlegel, M. Schubnell, H. Seo, A. Shafieloo, R. Sharples, J. Silber, A. Slosar, A. Smith, D. Sprayberry, T. Tan, G. Tarlé, P. Taylor, S. Trusov, L.A. Ureña-López, R. Vaisakh, D. Valcin, F. Valdes, M. Vargas-Magaña, L. Verde, M. Walther, B. Wang, M.S. Wang, B.A. Weaver, N. Weaverdyck, R.H. Wechsler, D.H. Weinberg, M. White, J. Yu, Y. Yu, S. Yuan, C. Yèche, E.A. Zaborowski, P. Zarrouk, H. Zhang, C. Zhao, R. Zhao, R. Zhou, T. Zhuang, and H. Zou. Desi 2024 vi: cosmological constraints from the measurements of baryon acoustic oscillations. *Journal of Cosmology and Astroparticle Physics*, 2025(02):021, February 2025.

[18] B. D. Fields, P. Molaro, and S. Sarkar. Big-bang nucleosynthesis. In S. Navas and others (Particle Data Group), editors, *Review of Particle Physics*, volume 110, page 030001. August 2024. Section 24 in the PDG 2024 Review.

[19] Edward W. Kolb and Michael S. Turner. *The Early Universe*. Addison-Wesley, Redwood City, CA, 1990.

[20] Scott Dodelson. *Modern Cosmology*. Academic Press, San Diego, CA, 2003.

[21] R. Soto. *Kinetic Theory and Transport Phenomena*. Oxford master series in condensed matter physics. Oxford University Press, 2016.

[22] Giorgio Arcadi, David Cabo-Almeida, Maíra Dutra, Pradipta Ghosh, Manfred Lindner, Yann Mambrini, Jacinto P. Neto, Mathias Pierre, Stefano Profumo, and Farinaldo S. Queiroz. The Waning of the WIMP: Endgame? *Eur. Phys. J. C*, 85(2):152, 2025.

[23] Constantino Tsallis, Fulvio Baldovin, Roberto Cerbino, and Paolo Pierobon. Introduction to nonextensive statistical mechanics and thermodynamics, 2003.

[24] E. M. F. Curado and C. Tsallis. Generalized statistical mechanics: connection with thermodynamics. *Journal of Physics A: Mathematical and General*, 24:L69–L72, 1991.

[25] Fevzi Büyükiliç, Dogan Demirhan, and Atilla Güleç. A statistical mechanical approach to generalized statistics of quantum and classical gases. *Physics Letters A*, 197(3):209–220, 1995.

[26] M.E. Pessah, Diego F. Torres, and H. Vucetich. Statistical mechanics and the description of the early universe. (i). foundations for a slightly non-extensive cosmology. *Physica A: Statistical Mechanics and its Applications*, 297(1–2):164–200, August 2001.

[27] Manuel Drees, Fazlollah Hajkarim, and Ernany Rossi Schmitz. The effects of qcd equation of state on the relic density of wimp dark matter. *Journal of Cosmology and Astroparticle Physics*, 2015(06):025–025, June 2015.

[28] B. D. Fields, P. Molaro, and S. Sarkar. Big bang nucleosynthesis. *Prog. Theor. Exp. Phys.*, 2024. in Particle Data Group Review.

[29] Mark Hindmarsh and Owe Philipsen. Wimp dark matter and the qcd equation of state. *Journal of Cosmology and Astroparticle Physics*, 2005(07):009, 2005.

[30] Ken'ichi Saikawa and Satoshi Shirai. Precise wimp relic abundance and the qcd equation of state. *Journal of Cosmology and Astroparticle Physics*, 2018(05):035, 2018.

[31] Uğur Tirnakli, Fevzi Büyükkiliç, and Doğan Demirhan. Some bounds upon the nonextensivity parameter using the approximate generalized distribution functions. *Physics Letters A*, 245(1–2):62–66, August 1998.

[32] Everton M.C. Abreu, Jorge Ananias Neto, Albert C.R. Mendes, and Wilson Oliveira. New bounds for tsallis parameter in a noncommutative phase–space entropic gravity and nonextensive friedmann equations. *Physica A: Statistical Mechanics and its Applications*, 392(20):5154–5163, October 2013.

[33] Uğur Tırnaklı and Diego F Torres. Quantal distribution functions in non-extensive statistics and an early universe test revisited. *Physica A: Statistical Mechanics and its Applications*, 268(1–2):225–230, 1999.

[34] Diego F. Torres, Héctor Vucetich, and A. Plastino. Early universe test of nonextensive statistics. *Physical Review Letters*, 79(9):1588–1590, 1997.

[35] Sabir Umarov and Constantino Tsallis. *Mathematical Foundations of Nonextensive Statistical Mechanics*. World Scientific, Singapore, 2022.

[36] Wan-Lei Guo and Yue-Liang Wu. The real singlet scalar dark matter model. *Journal of High Energy Physics*, 2010(10), October 2010.

[37] C. Tsallis, R. S. Mendes, and A. R. Plastino. The role of constraints within generalized nonextensive statistics. *Physica A: Statistical Mechanics and its Applications*, 261:534–554, 1998.